UNIVERSITY OF CALIFORNIA, MERCED

Programmed assemblies of biofunctionalized gold nanoclusters

A dissertation for the degree
Doctor of Philosophy

in

Chemistry and Biochemistry

by

Melissa Goodlad

2023

Committee members:
Professor Son Nguyen, Chair
Professor Tao Ye
Professor Anne Kelley
Professor Sayantani Ghosh

The dissertation of Melissa Goodlad is approved, and it is acceptable in quality and form for publication on microfilm and electronically:

(Professor Tao Ye)

(Professor Anne Kelley)

(Professor Sayantani Ghosh)

(Professor Son Nguyen, Chair)

University of California, Merced

2023

To Mr. Philip Cairney & Darwin

Table of Contents

List of Figures

List of Tables

Acknowledgements

I would like to thank my advisor, Dr. Tao Ye for his support throughout my graduate study at the University of California, Merced (UC Merced). I would also like to thank my committee, Dr. Son Nguyen, Dr. Anne Kelley and Dr. Sayantani Ghosh, for their guidance, patience and support.

I am grateful for my lab members, Dr. Huan Cao, Dr. Qufei Gu, Dr. Yehan Zhang, Dr. Paniz Rahmani, Zachary Petrek and Warren Nanney. Their insight and friendships have been invaluable.

Thank you to the UC Merced Teaching Lab and Dr. Ryan Baxter for allowing access to their instruments.

And finally, my deepest gratitude to Philip Cairney. I could not have done this without your love and support.

Curriculum Vitae

Melissa Goodlad

EDUCATION

- Ph. D. Chemistry and Biochemistry, 2023
  University of California Merced, Merced, CA

- B.A. Chemistry, cum laude, 2009
  California State University Fresno, Fresno, CA

RESEARCH EXPERIENCE

- Tao Ye Research Group, University of California Merced, (2016-2023)
- Undergraduate Researcher, Lawrence Berkeley National Laboratories, 2010

PUBLICATIONS

- Rahmani, P., **Goodlad, M.**, Zhang, Y., Li, Y., & Ye, T. (2022). One-Step Ligand-Exchange Method to Produce Quantum Dot–DNA Conjugates for DNA-Directed Self-Assembly. ACS Applied Materials & Interfaces, 14(42), 47359-47368.
- Perez-Lopez E, Gavrilova L, Disla J, **Goodlad M**, Ngo D, Seshappan A, et al. (2022) Ten Simple Rules for Creating and Sustaining Antiracist Graduate Programs. PLoS Comput Biol 18(10): e1010516.

TEACHING EXPERIENCE

- Teaching Assistant- Chemistry Center, Chemistry, UC Merced, (2016-2020)
- Chemistry/Physics Instructional Technician, Fresno City College (2014-2016)
- Teacher - AP Chemistry, Honors Chemistry. Clovis North High School (2011-2014)
- Teacher – Chemistry, Physics, Scientific Research, McLane High School (2010-2011)

AWARDS AND FELLOWSHIPS

- Merced nAnomaterials for Energy and Sensing Fellowship (2020-2021)
- Center for Cellular and Biomolecular Machines Fellowship (2018-2019)
- Chemistry and Chemical Biology Department Fellowship (2017-2018)

LEADERSHIP AND MENTORING EXPERIENCE

- Graduate Dean's Advisory Council on Diversity (2020-2021)
- Delegate for Chemistry and Chemical Biology for GSA (2020-2021)
- GradEXCEL Program Mentorship for incoming graduate students (2018-2021)
- Women in STEM Mentorship (2018-2019)

Abstract of the Dissertation

Programmed assemblies of bioconjugated gold nanoclusters

by

Melissa Goodlad

Doctor of Philosophy in Chemistry and Biochemistry

University of California, Merced, 2023

Monolayer-protected gold nanoclusters (AuNCs) are atomically precise assemblies less than 2 nanometers in diameter, giving them size-specific physical and chemical properties. This small size lends them to biosensing, electronics, optics, and biomedicine applications. The ligand monolayer contributes to the physical and chemical properties. Many nanomedicine applications require the conjugation of biomolecules into this ligand monolayer to interface with biological systems. While many bioconjugation strategies, DNA-based conjugations offer stability, functionality, and specificity. Thus, specific molecular recognition by DNA can be leveraged to target cell types and tissues.

Moreover, this programmable specificity of base-pairing allows for the precise self-assembly of multiple nanomaterials. Despite the advantages of AuNC-DNA conjugates, a detailed study has not been undertaken into the experimental conditions that lead to successful and predictable ligand exchange outcomes. The ligand monolayer significantly contributes to the physiochemical properties of AuNCs and has an even greater impact on how AuNCs interface with biological systems. Thus for AuNC-DNA conjugates, a purification technique must be able to isolate AuNC-$(DNA)_n$ from AuNC-$(DNA)_{n\pm1}$. By isolating each conjugate species, it is possible to study how each conjugate interfaces with a biological system. Finally, an emerging area of

interest is how AuNCs couple with other nanoscale components. For instance, the distance-dependent energy transfer between an AuNC and fluorophore would lend itself to future applications in biosensing and imaging. Coupling between AuNCs and other materials is sensitive to their relative position from each other. Thus, self-assembly methods capable of predefined geometrical arrangements and precise nanometer separation are needed. No publications meet these conjugation, isolation, and self-assembly needs in the AuNC field.

The projects detailed within this dissertation hope to address these gaps. In Chapter 2, we leverage the small size of monolayer-protected Au_{25} NCs to enable polyacrylamide gel electrophoresis (PAGE) and densitometric analysis to characterize the distribution of AuNCs with discrete numbers of DNA ligands under different reaction conditions. We found that both AuNC and salt concentrations affect ligand exchange products and that the noncovalent interactions of DNA are a nontrivial and complex variable in these reactions. The DNA ligands' length and sequence affect the final conjugation products of such reactions. The complexity of noncovalent DNA interactions and their effect on final products is not inconsequential. In Chapter 3, we sought to develop a method that could isolate AuNC-$(DNA)_n$ from AuNC-$(DNA)_{n\pm1}$ to aid in characterizing individual conjugate assemblies for downstream *in vivo* applications. We found ion-paired reversed-phased HPLC methods suitable for isolating and purifying the individual AuNC-DNA conjugates. After purification, the steady-state fluorescence studies that characterized the AuNC-DNA conjugates illustrated how differently an AuNC-$(DNA)_n$ can behave from an AuNC-$(DNA)_{n\pm1}$. Chapter 4 demonstrates the first successful AuNC self-assembly with precisely controlled positions on a DNA origami template. These results demonstrate that by functionalizing the AuNCs with the oligonucleotides via the ligand exchange reaction and then using the purified mono-functionalized products, we can program the self-assembly of the AuNCs with nanometer precision.

It is our hope that the work amassed here will further the field of AuNC applications. The specificity of DNA base-pairing combined with the stability of water-soluble thiolate monolayer-protected AuNC has significant potentialities. We have demonstrated the suitability of purified AuNC-DNA conjugates for self-assemblies.

Chapter 1

Introduction

1.1. Gold nanoclusters

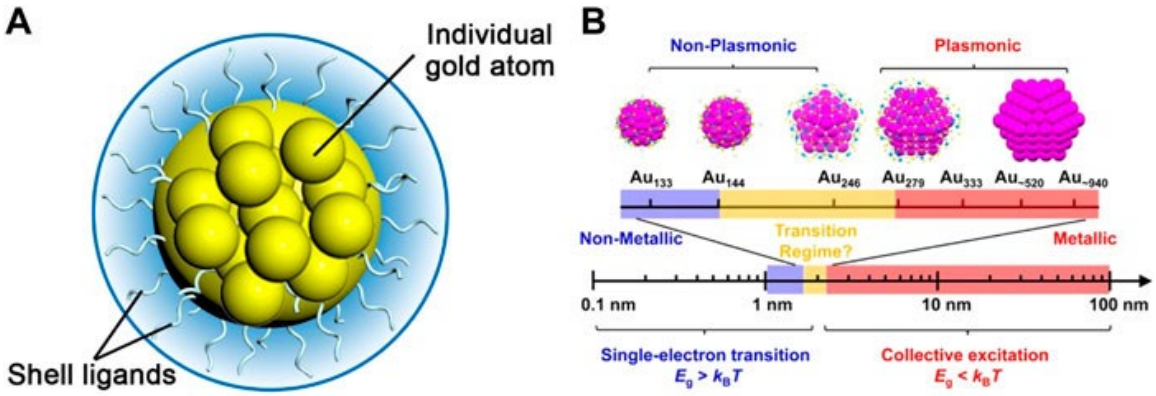

Figure 1.1. (A) Schematic illustration showing the gold core surrounded by the ligand monolayer. (B) The number of atoms and band gap changes gold nanoclusters transition from molecular to metallic properties[1].

The earliest use of metal nanoparticles dates back centuries[2]. Gold and silver nanoparticles were used to stain glass for cathedrals, create iridescent glazes and create vibrant pigments. Despite these common applications, their true size was unknown until recently available imaging techniques. We now know that in addition to the striking colors seen in nanoparticle solutions, many other properties of bulk metals change drastically as their size decreases. Bulk metals are colorless and shiny, while metal nanoparticles show vibrant colors in aqueous solutions. The vibrant color seen in these aqueous solutions is due to the excitation of electrons in the conduction band, also known as plasmonic resonance. As these nanoparticles become quantumly small, <2 nm in diameter, they no longer have a continuous conduction band. Gold nanoclusters (AuNCs) instead exhibit molecular-like properties such as *d–sp* and *sp–sp* transitions, broad absorption, and fluorescence properties[3]. These monolayer-protected AuNCs comprise a gold core protected by an outer shell of gold atoms and ligands[3,4].

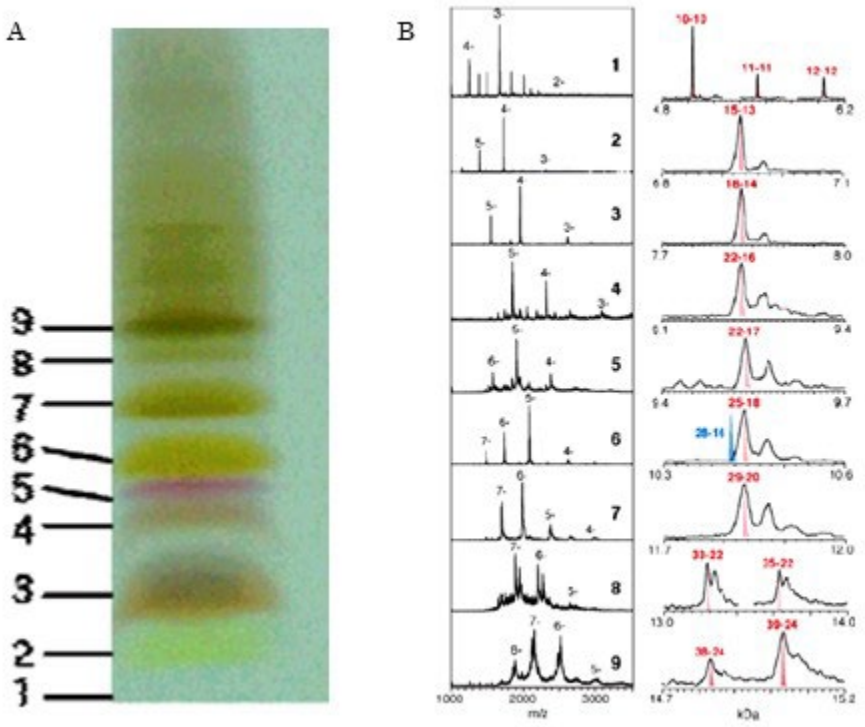

Figure 1.2. (A) PAGE image of the 9 AuNC species isolated by Tsukuda et al. and (B) ESI-MS of each AUNC. The right panel shows deconvoluted mass spectra[5].

While the first AuNCs were documented in 1996, the polydispersity of early synthetic methods stymied their applications[6]. The first synthesis of AuNCs with a narrow size distribution between 1.5-3.5 nm provided the first distinct spectra for AuNCs with diameters less than 2nm[7]. Tsukuda and coworkers achieved an important milestone in synthesizing atomically precise nanoclusters by developing a kinetically controlled synthesis of Au_{25} clusters capped with phenyl ethanethiol in high yield[8]. For purification, they could characterize atomically precise gold nanoclusters using polyacrylamide gel electrophoresis (PAGE), and the individual AuNC species were confirmed with electrospray ionization mass spectrometry (ESI-MS), as seen in Figure 1.2.

The high purity of the synthesized clusters allowed the growth of single crystals and the first X-ray crystallographic study[9]. In this paper, they determined the crystal structure of an $Au_{102}(p\text{-}MBA)_{44}$ to determine the nature of the bonding and packing of gold atoms. They determined that the Au_{102} structure has an Au_{79} core with D_{5h} symmetry. While MS can determine the identity of the AuNC, it is only possible to correlate the structure to the electronic properties by understanding the atomic packing and bonding between gold atoms and ligands. The X-ray crystallographic analysis of Au_{25}

revealed the presence of an Au_{13} icosahedron core with 12 remaining gold atoms arranged along the ±x, y, and z axes of the core. The 18 thiolate ligands form a staple motif with the exterior Au atoms, as seen in Figure 1.3.a-c. This study was also able to correlate the Au_{25} crystal structure to its optical properties, as seen in Figure 1.3.d-e[3].

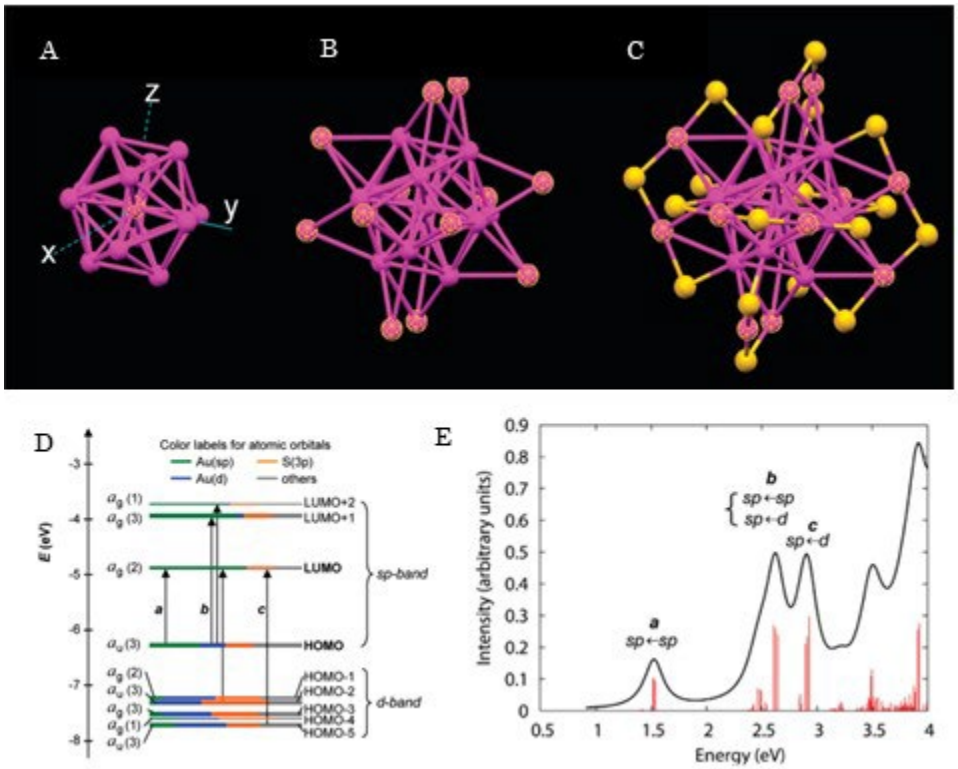

Figure 1.3. The correlation of the crystal structure of $Au_{25}(SR)_{18}$ to optical properties. (A) The metallic core of gold atoms (B) The ligand shell protecting the gold core (C) The Au-ligand interface (D) Kohn-Sham orbital energy level diagram for $Au_{25}(SH)_{18}$. The atomic orbitals of Au (6sp) in green, Au (5d) in blue, S (3p) in yellow, and all others in grey. (E) The theoretical absorption spectrum of $Au_{25}(SH)_{18}^{-}$ [3].

These optical properties, combined with their small size, and functional surface, water-soluble AuNCs have also gained interest in nanomedicine for applications in bioimaging[10–12], diagnostics, and therapies[13–15]. The ultra-small size of AuNCs makes them particularly well-suited for *in vivo* applications. The two main elimination pathways of metal nanoparticles (MNPs) from the body are the urinary and hepatic systems. A study used MNP 1.4-250 nm in size to determine their size-dependent toxicity. Larger gold nanoparticles had accumulated in different organs and showed poor degradation, which could induce acute toxicity[16,17]. The smaller size of the 1.4 nm AuNCs favored elimination and showed low toxicity [18].

AuNCs can be detected by several *in vivo* imaging techniques due to their photoluminescence (PL) that ranges from ultra-violet (UV) to the near-infrared (NIR) region[19]. AuNCs exhibiting PL in the NIR, 600 and 850 nm, [20–22]. This presents an advantage for *in vivo* imaging in deep tissues. These AuNCs have reduced auto-fluorescence and improved penetration of light into the tissues[23]. One limitation to imaging with AuNCs is their low PL quantum yields (QY), with most having QYs less than 1%[24]. Researchers have been synthesizing AuNCs with higher QYs by using more rigid ligands[25,26] or doping with other metals[27,28]. The Jin group at Carnegie-Mellon increased an AuNC QY to 40% by doping the gold core with 13 silver atoms[27].

The adaptable surface chemistry of AuNCs allows the incorporation of biocompatible ligands such as small organic molecules[29,30], amino acids[21] and peptides[31,32] proteins[33], and DNA[34,35]. These targeting molecules, such as folic acid, specifically interact with receptors at the surface of biomolecules. AuNCs conjugated to folic acid can target folate receptors overexpressed in cancer cells[36–38]. Such targeting AuNCs can *in vivo* imaging the biomolecules[23,39,40]. In the emerging field of theragnostics, where medical applications combine diagnostics with therapies, targeting AuNCs has been used for radio-[41,42], photo-[43,44], and chemotherapies[45,46].

When considering the available targeting ligands, DNA-based conjugations have several advantages over others. First, oligonucleotide bioconjugates are stable in temperature and pH fluctuations that would denature proteins. Second, synthetic DNA is relatively easy to manufacture and modify with various functional groups, such as fluorescent dyes, amines, and thiols. Third, DNA has high specificity for complementary base pairing, allowing for precise targeting and binding to complementary sequences.

Moreover, DNA aptamers, sequences selected through Sequential Evolution of Ligands by Exponential Enrichment (SELEX), can specifically bind to small molecules, proteins, cells, and tissues[47]. Thus, specific molecular recognition by DNA can be leveraged to target cell types of tissues. In a NIR imaging study, researchers could image a tumor up to 8 hours post-injection using AuNCs conjugated to only a tumor-targeting peptide. When they used AuNCs conjugated to both peptide and tumor-targeting aptamers, the tumor could be imaged more than 48 hours post-injection[45].

There is great potential for AuNCs in these fields. The underdeveloped characterization of the conjugation process hinders the development of AuNC-DNA in vivo applications. Understanding how DNA ligands are incorporated into the ligand monolayer allows us to build predictive models for yields and target interactions. Since the composition of the ligand monolayer significantly impacts the targeting ability and physicochemical properties of the AuNC, it is

also necessary to develop a purification technique that has the specificity to isolate and characterize these conjugates based on the number of conjugated biomolecules. Further, it is necessary to develop precise assemblies of AUNCs to characterize their coupling to biological interfaces and proximate nanomaterials. There are currently insufficient studies into AuNC bioconjugations, purification and self-assembly mechanisms to advance these materials. The research presented in this dissertation hopes to advance AuNC-DNA conjugates on these three fronts. The remaining sections of this chapter will review the literature on AuNC thiolate ligand exchange reactions (LERs), bioconjugate purification techniques, and AuNC self-assemblies.

1.2. Thiolate ligand exchange reactions

There are two main techniques for creating a biocompatible AuNC ligand monolayer. The first is a direct synthesis with the ligand that will compose the ligand monolayer[48,49]. The second is post-synthesis conjugation via Click chemistry[50], covalent attachment of biomolecules to the monolayer ligands[51–53], and LERs[54]. This bioconjugation allows AuNCs to be used as delivery systems[44,45,55]. LER that can conjugate AuNCs to thiol-functionalized biomolecules is a promising route. By attaching recognition elements, such bioconjugation would allow AuNCs to bind specific small molecules and biomolecules such as proteins, antibodies, or nucleic acids.

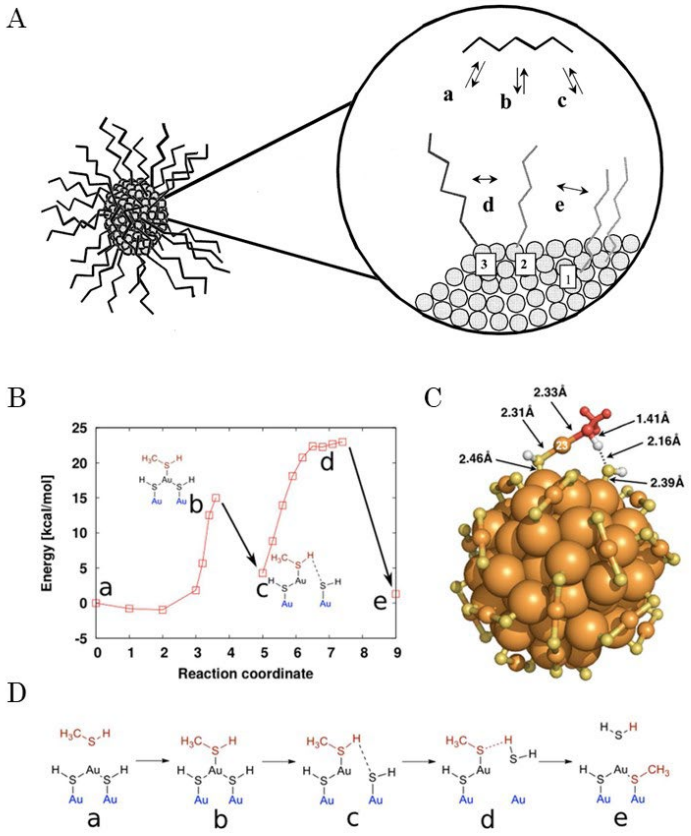

Figure 1.4. (A) The gold sites are labeled as (1) terrace core sites, (2) edge and near-edge core sites; and (3) vertice sites. (a) Exchange of vertice thiolates (3) with free thiols in solution; (b) Exchange of edge and near-edge thiolates (2) with free thiols in solution; (c) Exchange of terrace thiolates (1) with free thiols in solution; (d) Surface migration among vertice and edge thiolates; (e) Surface migration among edge and near-edge with terrace thiolates[56]. (B-D) Proposed ligand exchange process with thiol shown as energy behavior (B) and depicted as a sketch in the bottom panel (D). (C) Full rendering of the transition state (c) [57].

Hostetler et al. were the first to characterize the dynamics of LERs of AuNCs with a thiolated monolayer[56]. By mixing AuNCs with a solution of new alkyl-thiol ligands, Hostetler replaced ligands from the AuNC monolayer (Figure 1.4.a.). These thiol-thiol LERs are particularly interesting due to the robustness thiolated monolayers impart to gold nanomaterials[58]. Since these first characterizations by Hostetler, further experiments have elucidated the binding mechanism, hybridization efficiency, and the role of nonspecific adsorption non-biological ligands[57,59,60]. Experimental and computational studies have shown that the LER is an associative (SN2) pathway[57,61]. Consistent with the SN2 pathway, these studies discovered heterogeneity

among the different surface sites (Figure 1.4.a-d). Exposed surface sites undergo ligand exchange more readily than more protected sites. Additionally, several studies revealed the dependence of LER kinetics on the molecular structures of ligands on AuNCs and free ligands[62–66].

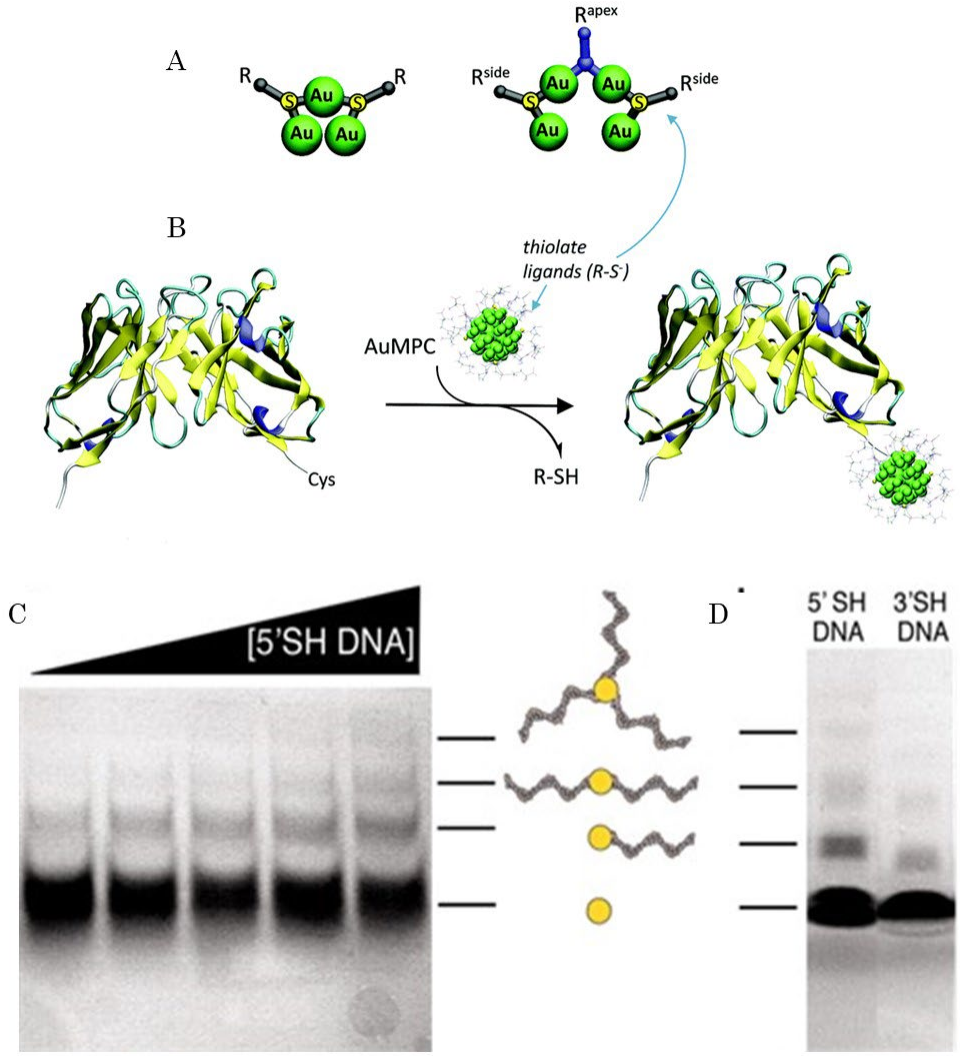

Figure 1.5. (A) Monomeric and dimeric thiol ligand (R) staple motifs on the surface of AuNCs. (B) Schematic of AuNC LER with an antibody [61]. (C) PAGE image of LER mixtures. Each lane contains 500 µM AuNCs and 50, 100, 150, 200, and 250 µM of 20-mer thiolated ssDNA ligands (from left to right). Each band above the bottom band representing excess AuNC indicates an additional DNA ligand. (D) PAGE image showing the difference in yield between a 20-mer ssDNA and AuNC LER and a 19-mer ssDNA ligand with a secondary structure[67].

Scientists have used such LERs to modify the functionality of AuNCs. Rojas-Cervellera et al. determined that the ligand exchange mechanism for a cysteine modified antibody was the same as those initially proposed by Hostetler[61]. As seen in Figure 1.5.a-b., the thiol-thiol LER of the glutathione ligand and antibody is an SN2 reaction. AuNCs conjugated to proteins are susceptible to aggregation, or denaturation due to pH or temperature changes[68]. DNA-AuNC conjugates are more robust and less susceptible to these issues. Despite these promising characteristics, the two most extensive LER studies for AuNC-DNA conjugates were published almost two decades ago [69,70]. This early research focused on establishing the viability of AuNC-DNA conjugation via LERs. As seen in Figures 1.5.c-d., the studies established the stoichiometric relationship between DNA: AuNC ratios and the number of thiol-modified DNA ligands (LDNA) conjugated to each AuNC. A low ratio produced AuNC-DNA with a smaller load of LDNA per AuNC, and a high ratio led to higher average loads of LDNA per AuNC-DNA. To better understand this critical reaction, we sought to characterize what effect salt, AuNC concentration, DNA sequence, and length have on the LER. We specifically looked at how these affect the yield of AuNC-DNA conjugates.

1.3. Purification of AuNCs

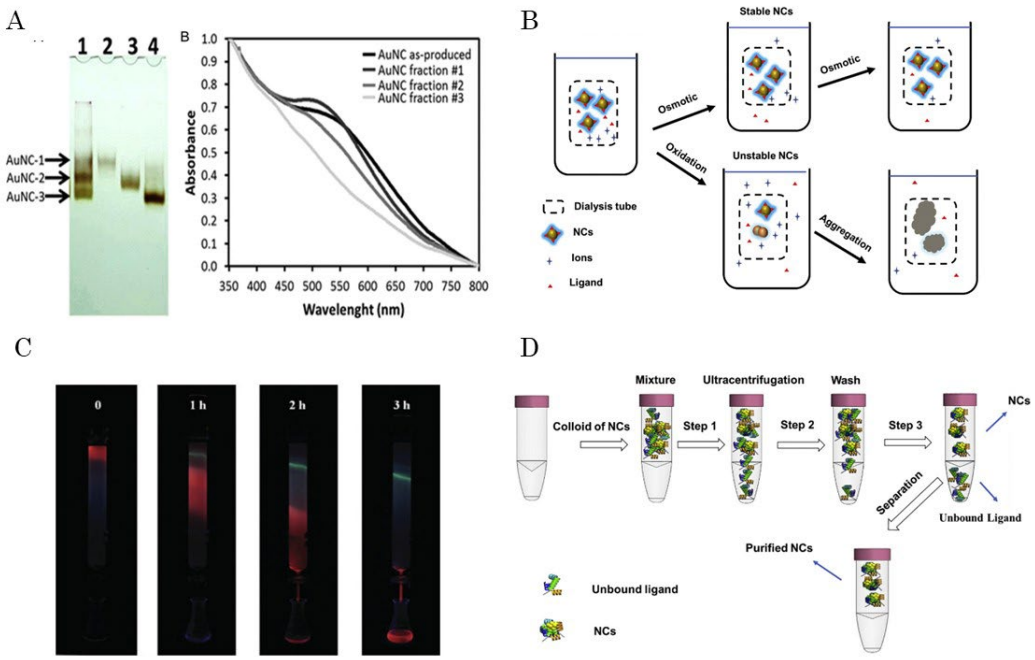

Figure 1.6. (A) AuNCs of different sizes were purified via gel extraction from a polyacrylamide gel. (B) Dialysis purification of AuNCs. The lower pathway shows challenges with oxidation and aggregation of unstable AuNCs. (C) Gel column purification of fluorescent AuNCs. AuNCs were excited with 365 nm irradiation. (D) Schematic showing ultracentrifugation purification of AuNCs[71].

Characterizing LERs is an important first step in increasing the viability of AuNC-DNA conjugate applications. The ligand monolayer significantly contributes to the physiochemical properties of AuNCs, affecting optical[25,72,73], stability[29,74], and catalytic[75] properties. Ligands also play a considerable role in how AuNCs interface with biological systems. As such, it is essential to characterize how incorporating DNA into the ligand monolayer will change the interfacing and physicochemical properties of the AuNC. Accomplishing this requires purification techniques to separate products from excess reactants and conjugate products based on the DNA load per AuNC. As discussed earlier, AuNCs are very promising for in vivo applications. Thus, it would be advantageous to pursue purification techniques that meet the scalability needs of clinical trials.

Most AuNC purification techniques are sufficient for removing excess reactants but lack the specificity or resolution to distinguish the number of bioligands. Aggregation-based techniques rely on changes in pH or salt to reach the isoelectric of the bioligand, which induces a reversible aggregation[71].

This technique would remove the excess AuNC, but excess biomolecules would also precipitate with the conjugates[76]. Molecular weight cutoff techniques such as dialysis or ultracentrifugation (Figure 1.6.b. and Figure 1.6.d.) would similarly only remove the excess ligand and AuNCs, but only if there was a sufficient size difference between the reactants and products[77,78]. All products would be grouped. SEC is close (Figure 1.6.c.), but there are smaller size differences between each products[79,80].

The most common method for isolating the AuNC-DNA bioconjugates by the number of DNA ligands is gel electrophoresis (GE)[81–84]. GE separates charged materials by moving them through a gel matrix in an electric field. Migration through the matrix depends on the materials' size, shape, and charge density. Small, highly charged materials migrate quickly through the matrix, while larger materials will travel more slowly. This technique visualizes the extent of bioconjugation to nanomaterials as well-resolved bands. These bands of bioconjugates can be extracted from the gel for later applications[85–88]. GE resolution is limited by the ability to visualize either the AuNCs or DNA in each band. Therefore, it is challenging to resolve DNA lengths below 50 bases[81]. These shorter, harder-to-resolve DNA lengths also have low gel extraction yields[89–92]. This can be a hindrance since precise programmed assembly often needs oligonucleotide lengths of 12-20 bases. The gel extraction process can be labor-intensive, time-consuming, and not readily scalable to the volumes necessary for large-scale production.

High-performance liquid chromatography (HPLC) is a powerful analytical technique that separates compounds based on their difference in relative affinities for the mobile and stationary phases used. The variety of stationary and mobile phases available makes HPLC a versatile technique. Like GE, HPLC can separate bioconjugates by the extent of bio-ligand coverage. However, unlike GE, HPLC is scalable with improved resolution, reproducibility, and purity.

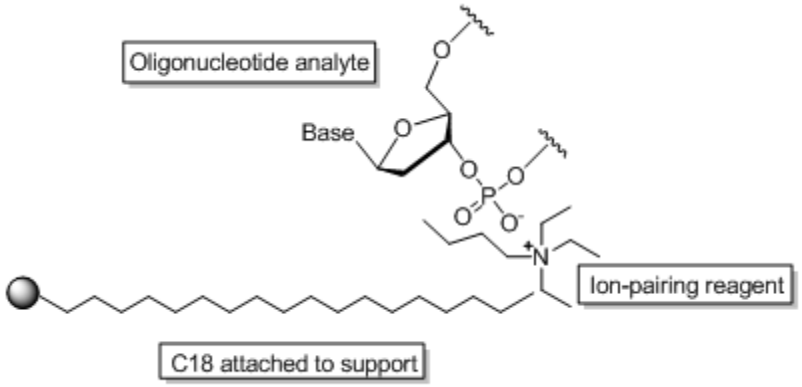

Figure 1.7. Interaction of an oligonucleotide with an ion-pairing reagent at the surface of a C18 ligand attached to a silica stationary phase[93].

Due to the instability of early water-soluble AuNCs, the first HPLC methods applied to AuNCs focused on those with lipophilic ligand monolayers. These first methods focused on separations of differently sized AuNCs, but later methods achieved high-resolution separations of mixed-ligand AuNCs[94–99]. The synthesis of stable water-soluble AuNCs suitable for biological applications makes HPLC a promising method for their purification. As with the lipophilic AUNCs, early methods have thus far focused on AuNC size separations[100,101]. As seen in Figure 1.8.b. Niihori et al. achieved a high-resolution separation of $Au_n(Glutathionate)_m$ clusters using an ion-paired reversed-phased (IP-RP) HPLC method[101]. IP-RP HPLC is a technique used to separate ionic compounds on a reversed-phased (RP) column. The surface of a RP stationary phase is hydrophobic. Without an ion-pairing reagent (IPR) in the mobile phase, the hydrophilic surface chemistry of water-soluble AuNCs has minimal interaction and poor resolution using RP methods. IPRs are generally alkylamines in an acidic solution, making them ionic and hydrophobic. The Coulombic interaction between the analyte and IPRs increases the analyte's hydrophobicity and adsorption capacity on a RP column.

Using tertbutyl ammonium perchlorate as their IPR, Niihori et al. were able to separate several species of AuNCs between $Au_{10}(Glutathionate)_{10}$ and $Au_{39}(Glutathionate)_{24}$ with atomic precision (Figure 1.8.b.). They determined that smaller AuNCs eluted before larger AuNCs. In the presence of IPR, larger AuNCs with more anionic ligands become more hydrophobic and thus have longer retention times than smaller AuNCs (Figure 1.8.a.).

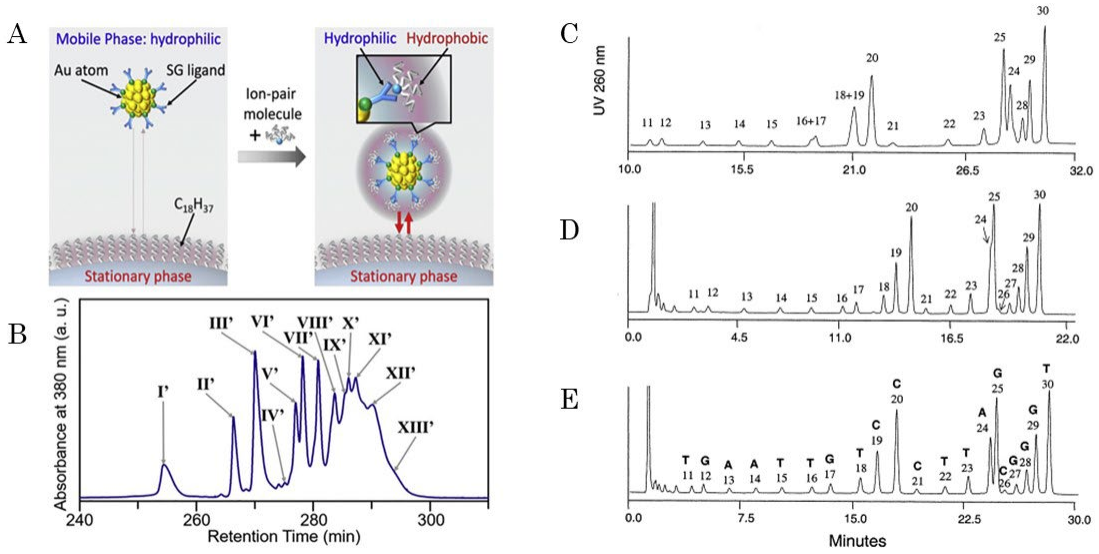

Figure 1.8. (A) Schematic showing the concept IP-RP PLC retention of water-soluble AuNCs. (B) Chromatogram showing the separation of $Au_n(SR)_m$ species [101]. (C-D) Separation of a 10-30 mer oligonucleotide ladder using three different IPRs. (C) Mobile phase A: 100 mM TEAA, pH 7. Mobile phase B: acetonitrile (D) Mobile phase A: 100 mM HFIP, 4.1 mM TEA, pH 8.4. Mobile phase B: methanol (E) Mobile phase A: 400 mM HFIP, 16.3 mM TEA, pH 7.9. Mobile phase B: methanol[102].

While HPLC is an emerging purification technique for AuNCs, it is used extensively to characterize and purify DNA. Due to DNA's strongly anionic phosphate backbone, IP-RP HPLC is typically deployed for these separations. Figure 1.7 shows that the IPR interacts with the oligonucleotide's charged phosphate group to form a hydrophobic pair. This field's extensive research has explored how liquid chromatography variables such as IPRs, temperatures, flowrates, stationary phases, and oligonucleotide modifications affect retention and resolution[102–109].

The two most common IPRs are a triethyl ammonium acetate (TEAA) for UV detection or a 1,1,1,3,3,3-hexafluoroisoproanol-triethyl ammonia (HFIP-TEA) buffer for mass spectrometry detection. As seen in Figures 1.8.a-c., HFIP-TEA buffers have superior selectivity than TEAA, and with higher concentrations, it is possible to achieve single nucleotide resolution 10-30 mer ladder.

The successes of IP-RP HPLC in purifying oligonucleotides and AuNCs suggest that this technique could also be a powerful method for separating AuNC-DNA conjugates. There has been no report using HPLC to purify such conjugates. Since IP-RP methods have achieved single nucleotide resolution, it is reasonable to conclude it could also isolate AuNC-$(DNA)_n$ from AuNC-

$(DNA)_{n\pm1}$. The research presented in Chapter 3 explores the viability of such IP-RP isolations and presents an optimized method for the separation and purification of $Au_{25}(Captopril)_{17}(DNA)$ and $Au_{25}(Captopril)_{16}(DNA)_2$. Characterization of the isolated analytes indicates that the method is successful. We found marked differences between the $Au_{25}(Captopril)_{17}(DNA)$ and $Au_{25}(Captopril)_{16}(DNA)_2$ characterizations, which serves to illustrate how significantly AuNC-DNA applications are affected by the quantity of DNA ligands.

1.4. Self-assembly of AuNCs

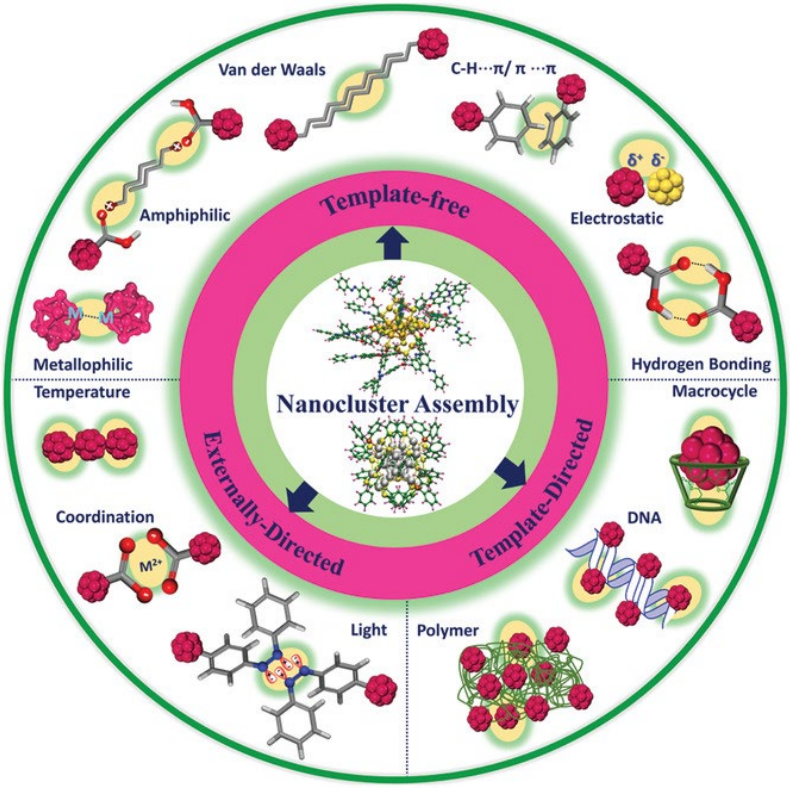

Figure 1.9. Schematic showing the various mechanisms used to assemble metal nanoclusters[110].

One key advantage to AuNC-DNA conjugates is their capacity for programmed assembly. A significant challenge to the fabrication of nanomaterials their need for self-assembly. The base-pairing ability of LDNA means that they can be placed with nanometer precision if their complimentary sequence is used as a target. An emerging area of interest is how AuNCs couple with other nanoscale components or materials to enable novel properties unavailable with isolated AuNCs. For instance, the distance-

dependent energy transfer between an AuNC and fluorophore would lend itself to future applications in biosensing and imaging. These energy transfer mechanisms are discussed in greater detail in the appendix. As the coupling interactions are highly sensitive to spatial organization, forming assemblies in which the AuNCs are positioned with organic dyes, nanoparticles, or other AuNCs with predefined geometrical arrangements and precise nanometer separation is essential.

Current methods of AuNC self-assembly can be broadly divided into template-free and template-directed. Template-free assemblies are facilitated by the properties of ligand monolayer. They are driven hydrogen bonding[9,111], electrostatic interactions[111] and van de Waals forces[112]. This type of self-assembly is best suited for the self-assembly of nanomaterials such as nanowires, nanosheets and crystal structures. It is possible to incorporate other nanomaterials into their fabrication, but template-free assemblies cannot do so with distance precision or varied geometry.

Template-directed assemblies are facilitated by molecules such as polymers or biomolecules[113,114] Templates are substrates with active sites that can selectively bind to AuNCs. These molecular organizations can induce the assembly of AuNCs to the template morphology. The ability to form these assemblies depends on the stability of AuNCs and template-AuNC morphologies and organizations[113]. DNA-templated assemblies have been used assemblies that incorporate other nanomaterials. DNA-templated copper nanoclusters (CuNC) have been used to create two-dimension DNA ribbons with precise distance separations[115]. DNA origami templates have been used to assemble many other nanomaterials and can achieve both the nanometer precision and the varied geometrical arrangements needed to study AuNC couplings. Despite these advantages DNA origami self-assemblies have not been applied to AuNCs [116]. This section will provide a more in depth look at the self-assemblies of DNA origami.

1.4.1 DNA origami

1.4.1.1 DNA

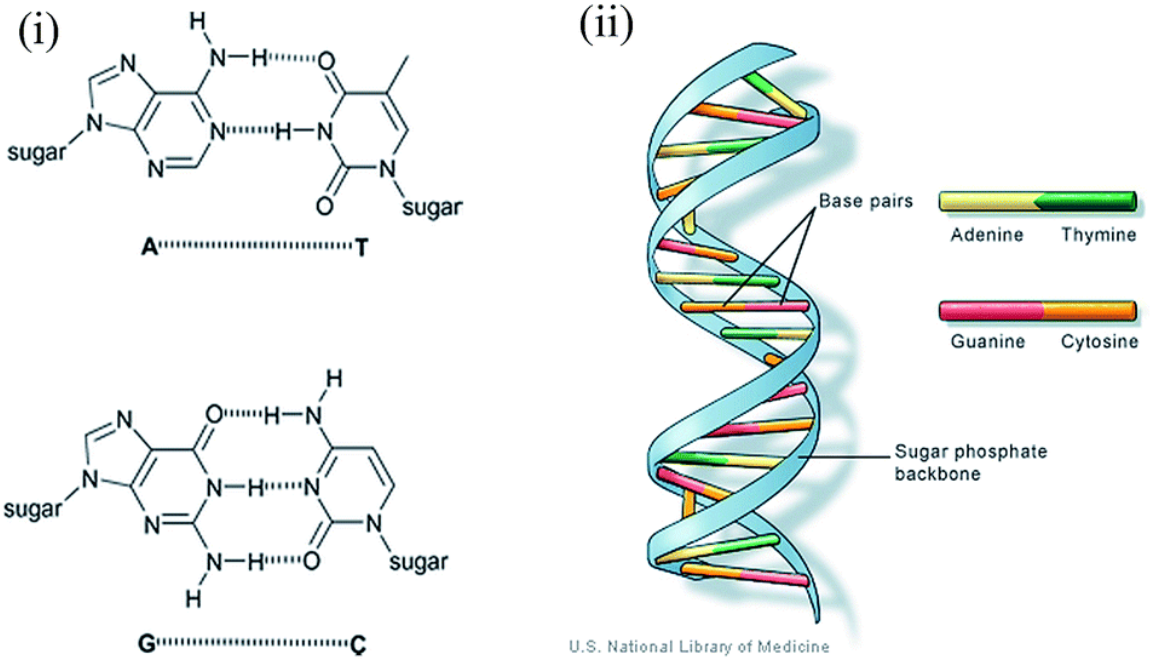

Figure 1.10. (i) The structure and base pairing of nucleotides (ii) The double helix structure of DNA

Watson and Crick first discovered the double helix structure of DNA and solved the X-ray diffraction pattern of DNA crystals[117]. It comprises two strands that wrap around each other to form a double helix, as described in 1953[117,118]. Each of the two strands is a linear sequence of nucleotide sub-units: adenine (A), guanine (G), cytosine (C), and thymine (T)[119]. An individual nucleoside has its base linked to the 1' carbon of deoxyribose (sugar). Nucleosides can form ester bonds with phosphates at the 3' and 5' carbons. Covalent bonds link one nucleotide's sugar with the next's phosphate, giving DNA its "sugar-phosphate backbone." The carbon number associated with the phosphodiester bond indicates the directionality of a single-stranded (ssDNA) sequence.

Bases project this backbone into the center of the double helix, where it can pair with the bases on the opposing strand[120]. The chemical structure of the bases is such that they form hydrogen bonds with each other in a highly specific manner. It forms two hydrogen bonds with T, and C forms three hydrogen bonds with G. Double-stranded DNA (dsDNA) comprises two complementary

ssDNA strands. When bonded, they form a double helix, held together by base pairs [119]. The most common dsDNA helical conformation is the right-handed B-helix, which makes a full turn every 10.4 base-pair (bps) or 3.4 nm. Energetically, it is highly favorable for two complementary strands to hybridize.

1.4.1.2 DNA origami

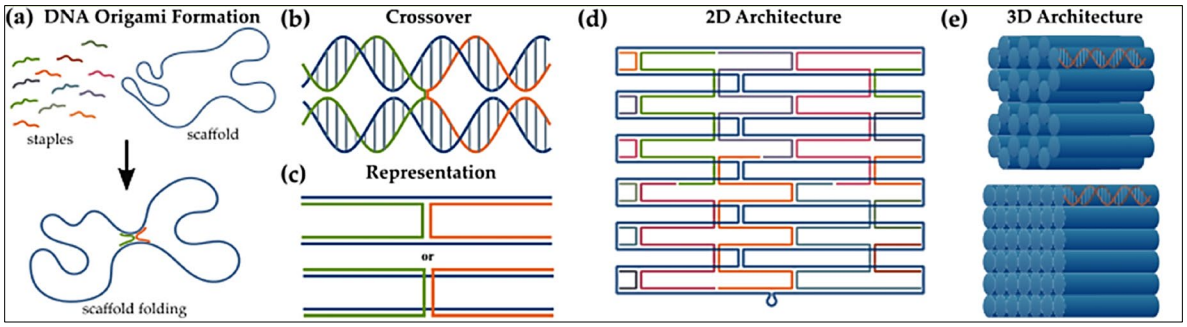

Figure 1.11. Schematic showing the folding process of DNA origami[121]

The specific base-pairing described in the preceding section underpins the field of DNA nanotechnology. Base-pairing provides a programmable methodology for the bottom-up fabrication of complex nanostructures, where each strand of DNA behaves as a programmable unit. In 1982 the first DNA lattice nanostructure was theorized and later realized by Seeman[122]. Since this first structure was realized, the field created octahedral, tetrahedral, 2D, and 3D assemblies [123–127].

In 2006, Rothemund published his study on DNA origami. He developed a method of creating shapes and patterns using a single long strand of DNA and a set of short strands called "staples"[128]. The typical scaffold for DNA origami is a circular ssDNA obtained from a bacteriophage (M13mp18). The set of staples determines the final shape adopted by the scaffold. Each staple strand binds to two or more scaffold sections, pinning them together. To create a flat DNA origami tile, it is necessary to place these crossovers at two proximal points of the helices every 1.5 turns, as seen in Figure 1.11.b. When designing the crossovers, it is assumed that 1.5 turns occur every 16 bases. Since this is not strictly true, one base pair must be deleted every 64 bases. Otherwise, the tile will twist. It is possible to place targeted insertions and deletions of base pairs in the staple set to create DNA origami with curvatures[129]. Using these design principles, other groups have created various 2D shapes [123,128,130–133], dolphins[134], and complex curvatures[135], such as flasks[135], a Mobius strip[136,137] or spheres[138]. Examples can be seen in Figure 1.12.

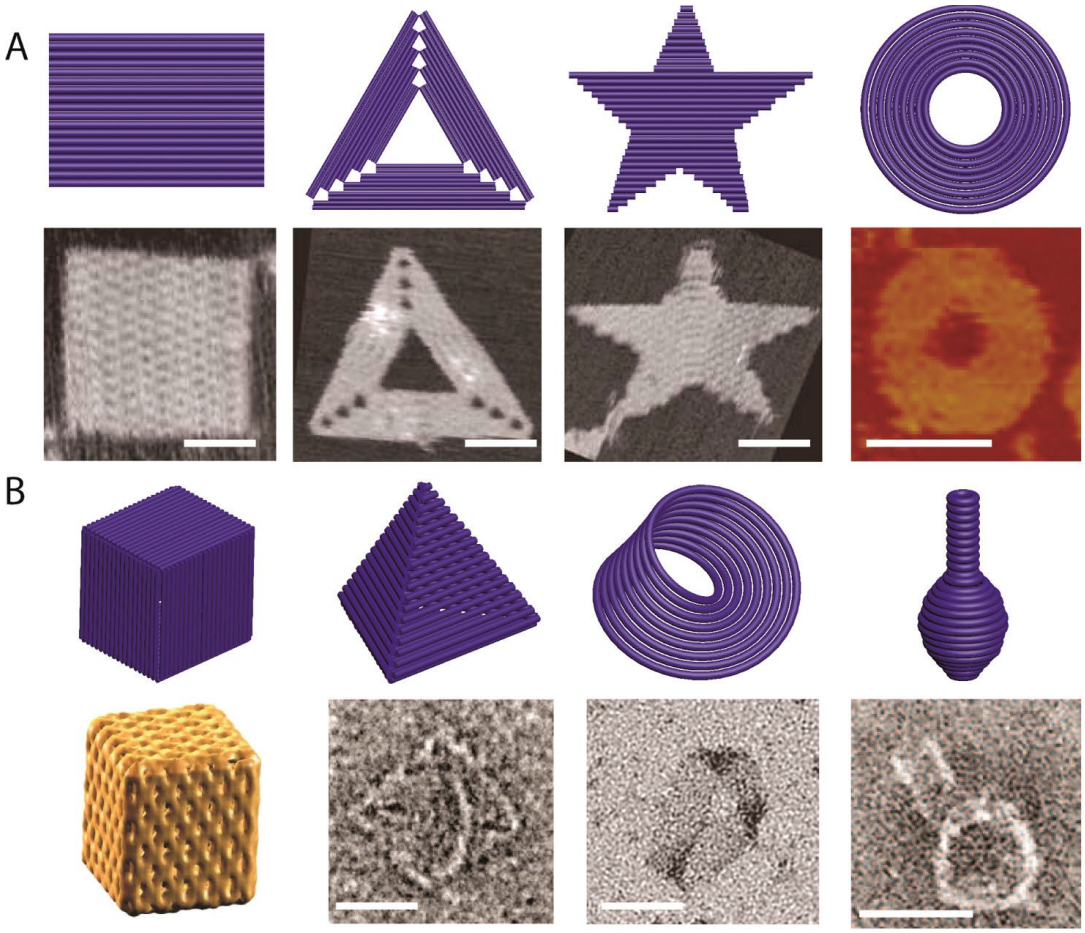

Figure 1.12. (A) is a selection of single layer 2D DNA origami designs (B) is a selection of 3D DNA origami designs 3D [123,128,130–134,138]. All scale bars are 50 nm.

1.4.1.3 DNA origami

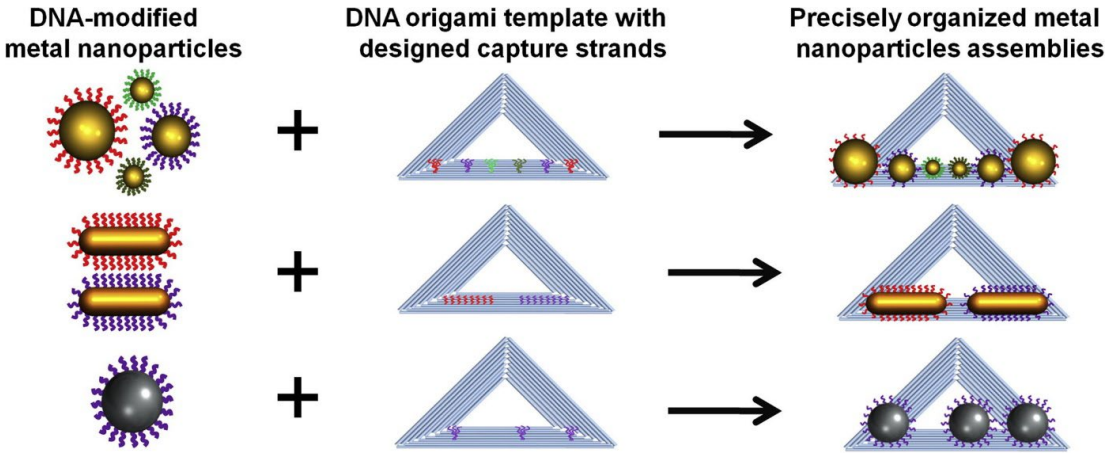

Figure 1.13. Schematic showing the assembly of biofunctionalized nanoparticles on a DNA origami surface[139].

Given that 200+ staples can be modified to act as a binding site, DNA origami is a versatile programmable breadboard for placing nanoscale objects with nanometer precision [128]. Many techniques have been developed for conjugating molecules or particles to DNA[70,140–144]. Extending a staple with the complement of that conjugated sequence makes it possible to assemble an array of materials on one DNA origami. DNA origami has been used as a template for site-specific binding of metallic nanoparticles[145–148], quantum dots[149], fluorophores[150], and carbon nanotubes[151]. It has since become common to attach gold nanoparticles (AuNPs) to origami structures, linking the AuNPs to DNA via a thiol bond[21].

Purified AuNC-DNA conjugates can be assembled on a DNA origami surface similarly. In Chapter 4 of this dissertation, we achieve the first AuNC-DNA origami self-assemblies. We can characterize these assemblies using steady-state fluorescent measurements by achieving precise separation distances from a fluorescent dye.

1.5. Scope of dissertation

AuNC-DNA conjugates are promising materials for imaging, sensing, and theragnostics. While reports of such bioconjugates were first published nearly 20 years ago, no publications have furthered their application since that time. Given the gaps in advancing these materials in the AuNC field, an in-depth understanding of the conjugation process is needed. The sensitivity of AuNC properties to the composition of their monolayer will also make it necessary to characterize AuNC-DNA conjugates by the number of LDNA incorporated into the monolayer. This requires sensitive, scalable purification techniques. Moreover, to better utilize and characterize the coupling properties of AuNCs, self-assembly techniques need to achieve precise geometric arrangements. The work presented in this dissertation hopes to address these gaps.

Chapter 2 of this dissertation uses PAGE and densitometric analysis to characterize AuNC LERs between the captopril monolayer and thiolated DNA. We determined that salt concentrations and the stoichiometric ratios of DNA to AuNC affect the overall yield and the number of discrete LDNA per AuNC. Our analysis also indicates that the noncovalent interactions between LDNAs play a role in yield and LDNA load per AuNC. In Chapter 3, we investigate IP-RP HPLC as a method for isolating AuNC-$(DNA)_n$ from AuNC-$(DNA)_{n\pm1}$. We conjugated AuNCs to Cyanine5 (Cy5) functionalized DNA to demonstrate their suitability for self-assembly applications. We used steady-state fluorescence spectroscopic studies to characterize the AuNC-Cy5 conjugates. These

spectroscopic results demonstrated that our IP-RP HPLC method has successfully isolated the mono- and di-conjugates. Finally, Chapter 4 presents the first AuNC DNA origami self-assemblies. Here we placed multiple AuNCs at different precise distances from a fluorescent dye. Steady-state fluorescence spectroscopy measurements demonstrated the annealing kinetics with a decrease in relative fluorescence proportional to the number of fAuNCs relative to Cy5 over time. By presenting this research, we hope to advance the field of AuNC-DNA conjugate applications.

1.6. References

1. Cheng D, Liu R, Hu K. Gold nanoclusters: Photophysical properties and photocatalytic applications. *Front Chem*. 2022;10. doi:10.3389/fchem.2022.958626

2. Bayda S, Adeel M, Tuccinardi T, Cordani M, Rizzolio F. The history of nanoscience and nanotechnology: From chemical-physical applications to nanomedicine. *Molecules*. 2020;25(1). doi:10.3390/molecules25010112

3. Zhu M, Aikens CM, Hollander FJ, Schatz GC. Correlating the Crystal Structure of A Thiol-Protected Au 25 Cluster and Optical Properties. *J Am Chem Soc*. 2008;130:5883-5885. doi:10.1021/ja801173r

4. Jadzinsky PD, Calero G, Ackerson CJ, Bushnell DA, Kornberg RD. Structure of a Thiol Monolayer-Protected Gold Nanoparticle at 1.1 A Resolution. *Science (1979)*. 2007;318(5849):426-430. doi:10.1126/science.1147241

5. Yukatsu Shichibu †, Yuichi Negishi ‡, Tatsuya Tsukuda *,‡ and, Toshiharu Teranishi* §. Large-Scale Synthesis of Thiolated Au25 Clusters via Ligand Exchange Reactions of Phosphine-Stabilized Au11 Clusters. *J Am Chem Soc*. 2005;127(39):13464-13465. doi:10.1021/JA053915S

6. Alivisatos AP, Johnsson KP, Peng X, et al. Organization of "nanocrystal molecules" using DNA. *Nature*. 1996;382(6592):609-611. doi:10.1038/382609A0

7. Schaaff TG, Shafigullin MN, Khoury JT, et al. Isolation of smaller nanocrystal Au molecules: Robust quantum effects in optical spectra. *Journal of Physical Chemistry B*. 1997;101(40). doi:10.1021/jp971438x

8. Zhu M, Lanni E, Garg N, Bier ME, Jin R. Kinetically controlled, high-yield synthesis of Au25 clusters. *J Am Chem Soc*. 2008;130(4):1138-1139. doi:10.1021/JA0782448

9. Jadzinsky PD, Calero G, Ackerson CJ, Bushnell DA, Kornberg RD. Structure of a Thiol Monolayer-Protected Gold Nano Particle. *Science*. 2007;318(5849):430-433. doi:10.1126/science.1147241

10. Polavarapu L, Manna M, Xu QH. Biocompatible glutathione capped gold clusters as one- and two-photon excitation fluorescence contrast agents for live cells imaging. *Nanoscale*. 2011;3(2):429-434. doi:10.1039/C0NR00458H

11. Niu J, Wang X, Lv J, Li Y, Tang B. Luminescent nanoprobes for in-vivo bioimaging. *TrAC - Trends in Analytical Chemistry*. 2014;58:112-119. doi:10.1016/j.trac.2014.02.013

12. Zhang L, Wang E. Metal nanoclusters: New fluorescent probes for sensors and bioimaging. *Nano Today*. 2014;9(1). doi:10.1016/j.nantod.2014.02.010

13. Yang K, Wang S, Wang Y, Miao H, Yang X. Dual-channel probe of carbon dots cooperating with gold nanoclusters employed for assaying multiple targets. Published online 2017. doi:10.1016/j.bios.2017.01.014

14. Fernández TD, Pearson JR, Leal MP, et al. Intracellular accumulation and immunological properties of fluorescent gold nanoclusters in human dendritic cells. *Biomaterials*. 2015;43(1):1-12. doi:10.1016/J.BIOMATERIALS.2014.11.045

15. Zhang XD, Chen J, Luo Z, et al. Enhanced Tumor Accumulation of Sub-2 nm Gold Nanoclusters for Cancer Radiation Therapy. Published online 2013. doi:10.1002/adhm.201300189

16. Blanco E, Shen H, Ferrari M. Principles of nanoparticle design for overcoming biological barriers to drug delivery. *Nat Biotechnol*. 2015;33(9). doi:10.1038/nbt.3330

17. Ehlerding EB, Chen F, Cai W. Biodegradable and renal clearable inorganic nanoparticles. *Advanced Science*. 2015;3(2). doi:10.1002/advs.201500223

18. Liu J, Yu M, Zhou C, Yang S, Ning X, Zheng J. Passive tumor targeting of renal-clearable luminescent gold nanoparticles: Long tumor retention and fast normal tissue clearance. *J Am Chem Soc*. 2013;135(13). doi:10.1021/ja401612x

19. Zheng J, Zhang C, Dickson RM. Highly fluorescent, water-soluble, size-tunable gold quantum dots. *Phys Rev Lett*. 2004;93(7). doi:10.1103/PhysRevLett.93.077402

20. Liu J, Yu M, Ning X, Zhou C, Yang S, Zheng J. PEGylation and zwitterionization: Pros and cons in the renal clearance and tumor targeting of near-IR-emitting gold nanoparticles. *Angewandte Chemie - International Edition*. 2013;52(48). doi:10.1002/anie.201304465

21. Ning X, Peng C, Li ES, et al. Physiological stability and renal clearance of ultrasmall zwitterionic gold nanoparticles: Ligand length matters. *APL Mater*. 2017;5(5). doi:10.1063/1.4978381

22. Rambukwella M. Ligand Effect on Gold Nanomolecules Demonstrated Using Ligand Effect on Gold Nanomolecules Demonstrated Using Aliphatic, Aromatic and Bulky Thiolate Ligands Aliphatic, Aromatic and Bulky Thiolate Ligands. Published online 2018. https://egrove.olemiss.edu/etd

23. Hong G, Antaris AL, Dai H. Near-infrared fluorophores for biomedical imaging. *Nat Biomed Eng*. 2017;1(1). doi:10.1038/s41551-016-0010

24. Link S, Beeby A, FitzGerald S, El-Sayed MA, Schaaff TG, Whetten RL. Visible to infrared luminescence from a 28-atom gold cluster. *Journal of Physical Chemistry B*. 2002;106(13). doi:10.1021/jp014259v

25. Guevel X Le, Tagit O, Rodríguez CE, Trouillet V, Pernia Leal M, Hildebrandt N. Ligand effect on the size, valence state and red/near infrared photoluminescence of bidentate thiol gold nanoclusters. *Nanoscale*. 2014;6(14). doi:10.1039/c4nr01130a

26. Pyo K, Thanthirige VD, Kwak K, Pandurangan P, Ramakrishna G, Lee D. Ultrabright Luminescence from Gold Nanoclusters: Rigidifying the Au(I)-Thiolate Shell. *J Am Chem Soc*. Published online 2015. doi:10.1021/jacs.5b04210

27. Wang S, Meng X, Das A, et al. A 200-fold Quantum Yield Boost in the Photoluminescence of Silver-Doped $Ag_x Au_{25-x}$ Nanoclusters: The 13 th Silver Atom Matters. *Angewandte Chemie International Edition*. 2014;53(9):2376-2380. doi:10.1002/anie.201307480

28. Oh E, Delehanty JB, Field LD, et al. Synthesis and Characterization of PEGylated Luminescent Gold Nanoclusters Doped with Silver and Other Metals. *Chemistry of Materials*. 2016;28(23). doi:10.1021/acs.chemmater.6b03838

29. Ackerson CJ, Jadzinsky PD, Kornberg RD. Thiolate ligands for synthesis of water-soluble gold clusters. *J Am Chem Soc*. 2005;127(18). doi:10.1021/ja046114i

30. Yuan X, Zhang B, Luo Z, et al. Balancing the Rate of Cluster Growth and Etching for Gram-Scale Synthesis of Thiolate-Protected Au 25 Nanoclusters with Atomic Precision . *Angewandte Chemie*. 2014;126(18). doi:10.1002/ange.201311177

31. Negishi Y, Nobusada K, Tsukuda T. Glutathione-protected gold clusters revisited: Bridging the gap between gold(I)-thiolate complexes and thiolate-protected gold nanocrystals. *J Am Chem Soc*. 2005;127(14). doi:10.1021/ja042218h

32. Vinluan RD, Liu J, Zhou C, et al. Glutathione-coated luminescent gold nanoparticles: A surface ligand for minimizing serum protein adsorption. *ACS Appl Mater Interfaces*. 2014;6(15). doi:10.1021/am5031374

33. Xie J, Zheng Y, Ying JY. Protein-directed synthesis of highly fluorescent gold nanoclusters. *J Am Chem Soc*. 2009;131(3). doi:10.1021/ja806804u

34. Liu G, Shao Y, Ma K, Cui Q, Wu F, Xu S. Synthesis of DNA-templated fluorescent gold nanoclusters. *Gold Bull*. 2012;45(2):69-74. doi:10.1007/s13404-012-0049-6

35. Sahoo AK, Sailapu SK, Dutta D, Banerjee S, Ghosh SS, Chattopadhyay A. DNA-Templated Single Thermal Cycle Based Synthesis of Highly Luminescent Au Nanoclusters for Probing Gene Expression. *ACS Sustain Chem Eng*. 2018;6(2):2142-2151. doi:10.1021/acssuschemeng.7b03568

36. Wang Y, Dai C, Yan XP. Fabrication of folate bioconjugated near-infrared fluorescent silver nanoclusters for targeted in vitro and in vivo bioimaging. *Chemical Communications*. 2014;50(92). doi:10.1039/c4cc06329e

37. Zhang P, Yang XX, Wang Y, Zhao NW, Xiong ZH, Huang CZ. Rapid synthesis of highly luminescent and stable Au20 nanoclusters for active tumor-targeted imaging in vitro and in vivo. *Nanoscale*. 2014;6(4). doi:10.1039/c3nr05269a

38. Chen H, Li S, Li B, et al. Folate-modified gold nanoclusters as near-infrared fluorescent probes for tumor imaging and therapy. *Nanoscale*. 2012;4(19). doi:10.1039/c2nr31616a

39. Hong G, Diao S, Chang J, et al. Through-skull fluorescence imaging of the brain in a new near-infrared window. *Nat Photonics*. 2014;8(9). doi:10.1038/nphoton.2014.166

40. Hong G, Lee JC, Robinson JT, et al. Multifunctional in vivo vascular imaging using near-infrared II fluorescence. *Nat Med*. 2012;18(12). doi:10.1038/nm.2995

41. Zhang XD, Chen J, Luo Z, et al. Enhanced Tumor Accumulation of Sub-2 nm Gold Nanoclusters for Cancer Radiation Therapy. Published online 2013. doi:10.1002/adhm.201300189

42. Zhang XD, Luo Z, Chen J, et al. Ultrasmall glutathione-protected gold nanoclusters as next generation radiotherapy sensitizers with high tumor uptake and high renal clearance. *Sci Rep*. 2015;5. doi:10.1038/srep08669

43. Kawasaki H, Kumar S, Li G, et al. Generation of singlet oxygen by photoexcited Au25(SR) 18 clusters. *Chemistry of Materials*. 2014;26(9). doi:10.1021/cm500260z

44. Nair L V., Nazeer SS, Jayasree RS, Ajayaghosh A. Fluorescence Imaging Assisted Photodynamic Therapy Using Photosensitizer-Linked Gold Quantum Clusters. *ACS Nano*. 2015;9(6). doi:10.1021/acsnano.5b00406

45. Chen D, Li B, Cai S, et al. Dual targeting luminescent gold nanoclusters for tumor imaging and deep tissue therapy. *Biomaterials*. 2016;100:1-16. doi:10.1016/j.biomaterials.2016.05.017

46. Huang P, Lin J, Wang S, et al. Photosensitizer-conjugated silica-coated gold nanoclusters for fluorescence imaging-guided photodynamic therapy. *Biomaterials*. 2013;34(19). doi:10.1016/j.biomaterials.2013.02.063

47. Fang X, Tan W. Aptamers Generated from Cell-SELEX for Molecular Medicine: A Chemical Biology Approach. *Acc Chem Res*. 2009;43(1):48-57. doi:10.1021/ar900101s

48. Aldeek F, Muhammed MAH, Palui G, Zhan N, Mattoussi H. Growth of highly fluorescent polyethylene glycol- and zwitterion- functionalized gold nanoclusters. *ACS Nano*. 2013;7(3). doi:10.1021/nn305856t

49. Yuan X, Zhang B, Luo Z, et al. Balancing the rate of cluster growth and etching for gram-scale synthesis of thiolate-protected Au25 nanoclusters with atomic precision. *Angewandte Chemie - International Edition*. 2014;53(18). doi:10.1002/anie.201311177

50. Oh E, Fatemi FK, Currie M, et al. PEGylated luminescent gold nanoclusters: Synthesis, characterization, bioconjugation, and application to one- and two-photon cellular imaging. *Particle and Particle Systems Characterization*. 2013;30(5). doi:10.1002/ppsc.201200140

51. Wang JY, Chen J, Yang J, et al. Effects of surface charges of gold nanoclusters on long-term in vivo biodistribution, toxicity, and cancer radiation therapy. *Int J Nanomedicine*. 2016;11. doi:10.2147/IJN.S106073

52. Zhao Y, Detering L, Sultan D, et al. Gold Nanoclusters Doped with 64Cu for CXCR4 Positron Emission Tomography Imaging of Breast Cancer and Metastasis. *ACS Nano*. 2016;10(6). doi:10.1021/acsnano.6b01326

53. Shibu ES, Muhammed MAH, Tsukuda T, Pradeep T. Ligand Exchange of Au 25 SG 18 Leading to Functionalized Gold Clusters: Spectroscopy, Kinetics, and Luminescence. doi:10.1021/jp800508d

54. Shibu ES, Muhammed MAH, Tsukuda T, Pradeep T. Ligand exchange of Au25SG18 leading to functionalized gold clusters: Spectroscopy, kinetics, and luminescence. *Journal of Physical Chemistry C*. 2008;112(32):12168-12176. doi:10.1021/jp800508d

55. Zhang C, Li C, Liu Y, et al. Gold nanoclusters-based nanoprobes for simultaneous fluorescence imaging and targeted photodynamic therapy with superior penetration and retention behavior in tumors. *Adv Funct Mater*. 2015;25(8). doi:10.1002/adfm.201403095

56. J. Hostetler M, C. Templeton A, W. Murray R. Dynamics of Place-Exchange Reactions on Monolayer-Protected Gold Cluster Molecules. *Langmuir*. 1999;15(11):3782-3789. doi:10.1021/la981598f

57. L. Heinecke C, W. Ni T, Malola S, et al. Structural and Theoretical Basis for Ligand Exchange on Thiolate Monolayer Protected Gold Nanoclusters. *J Am Chem Soc*. 2012;134(32):13316-13322. doi:10.1021/ja3032339

58. Mani G, Johnson DM, Marton D, et al. Stability of self-assembled monolayers on titanium and gold. *Langmuir*. 2008;24(13):6774-6784. doi:10.1021/la8003646

59. Guo R, Song Y, Wang G, Murray RW. Does core size matter in the kinetics of ligand exchanges of monolayer-protected Au clusters? *J Am Chem Soc*. 2005;127(8):2752-2757. doi:10.1021/ja044638c

60. Song Y, Murray RW. Dynamics and extent of ligand exchange depend on electronic charge of metal nanoparticles. *J Am Chem Soc*. 2002;124(24):7096-7102. doi:10.1021/ja0174985

61. Rojas-Cervellera V, Raich L, Akola J, Rovira C. The molecular mechanism of the ligand exchange reaction of an antibody against a glutathione-coated gold cluster. *Nanoscale*. 2017;9(9):3121-3127. doi:10.1039/C6NR08498B

62. Suzuki W, Takahata R, Chiga Y, et al. Control over Ligand-Exchange Positions of Thiolate-Protected Gold Nanoclusters Using Steric Repulsion of Protecting Ligands. *J Am Chem Soc*. 2022;144(27):12310-12320. doi:10.1021/jacs.2c03670

63. Li Z, Cheng E, Huang W, et al. Improving the yield of mono-DNA-functionalized gold nanoparticles through dual steric hindrance. *J Am Chem Soc*. 2011;133(39):15284-15287. doi:10.1021/JA205712A/SUPPL_FILE/JA205712A_SI_001.PDF

64. Li Y, Juarez-Mosqueda R, Song Y, et al. Ligand exchange on Au38(SR)24: Substituent site effects of aromatic thiols. *Nanoscale*. 2020;12(17). doi:10.1039/d0nr01430c

65. Liu M, Che F, Sun B, et al. Controlled Steric Hindrance Enables Efficient Ligand Exchange for Stable, Infrared-Bandgap Quantum Dot Inks. *ACS Energy Lett*. 2019;4(6). doi:10.1021/acsenergylett.9b00388

66. Wang Y, Chen AA, Balto KP, et al. Curvature-Selective Nanocrystal Surface Ligation Using Sterically-Encumbered Metal-Coordinating Ligands. *ACS Nano*. 2022;16(8). doi:10.1021/acsnano.2c04595

67. Ackerson CJ, Sykes MT, Kornberg RD. Defined DNA/nanoparticle conjugates. *Proc Natl Acad Sci U S A*. 2005;102(38):13383-13385. doi:10.1073/pnas.0506290102

68. Porret E, Le Guével X, Coll JL. Gold nanoclusters for biomedical applications: Toward: In vivo studies. *J Mater Chem B*. 2020;8(11):2216-2232. doi:10.1039/c9tb02767j

69. Jhaveri SD, Foos EE, Lowy DA, Chang EL, Snow AW, Ancona MG. Isolation and Characterization of Trioxyethylene-Encapsulated Gold Nanoclusters Functionalized with a Single DNA Strand. *Nano Lett*. 2004;4(4):737-740. doi:10.1021/nl0499591

70. Ackerson CJ, Sykes MT, Kornberg RD. Defined DNA/nanoparticle conjugates. *Proc Natl Acad Sci U S A*. 2005;102(38):13383-13385. doi:10.1073/PNAS.0506290102

71. Li D, Kumari B, Zhang X, Wang C, Mei X, Rotello VM. Purification and separation of ultra-small metal nanoclusters. *Adv Colloid Interface Sci*. 2020;276:102090. doi:10.1016/J.CIS.2019.102090

72. Konishi K, Iwasaki M, Sugiuchi M, Shichibu Y. Ligand-Based Toolboxes for Tuning of the Optical Properties of Subnanometer Gold Clusters. *Journal of Physical Chemistry Letters*. 2016;7(21):4267-4274. doi:10.1021/acs.jpclett.6b01999

73. Yuan X, Goswami N, Chen W, Yao Q, Xie J. Insights into the effect of surface ligands on the optical properties of thiolated Au25nanoclusters. *Chemical Communications*. 2016;52(30). doi:10.1039/c6cc00857g

74. Kumar S, Jin R. Water-soluble Au25(Capt)18 nanoclusters: synthesis, thermal stability, and optical properties. *Nanoscale*. 2012;4(14):4222-4227. doi:10.1039/c2nr30833a

75. Liu J, Krishna KS, Losovyj YB, et al. Ligand-stabilized and atomically precise gold nanocluster catalysis: A case study for correlating fundamental electronic properties with catalysis. *Chemistry - A European Journal*. 2013;19(31):10201-10208. doi:10.1002/chem.201300600

76. Xiong H, Wang W, Liang J, Wen W, Zhang X, Wang S. A convenient purification method for metal nanoclusters based on pH-induced aggregation and cyclic regeneration and its applications in fluorescent pH sensors. *Sens Actuators B Chem*. 2017;239. doi:10.1016/j.snb.2016.08.114

77. Li P, Kumar A, Ma J, Kuang Y, Luo L, Sun X. Density gradient ultracentrifugation for colloidal nanostructures separation and investigation. *Sci Bull (Beijing)*. 2018;63(10). doi:10.1016/j.scib.2018.04.014

78. Tang Y, Xu J, Xiong C, Xiao Y, Zhang X, Wang S. Enhanced electrochemiluminescence of gold nanoclusters: Via silver doping and their application for ultrasensitive detection of dopamine. *Analyst*. 2019;144(8). doi:10.1039/c9an00032a

79. Li HW, Ai K, Wu Y. Fluorescence visual gel-separation of dansylated BSA-protected gold-nanoclusters. *Chemical Communications*. 2011;47(35). doi:10.1039/c1cc12588e

80. Amartely H, Avraham O, Friedler A, Livnah O, Lebendiker M. Coupling Multi Angle Light Scattering to Ion Exchange chromatography (IEX-MALS) for protein characterization. *Sci Rep*. 2018;8(1). doi:10.1038/s41598-018-25246-6

81. Zanchet D, M. Micheel C, J. Parak W, Gerion D, Paul Alivisatos A. Electrophoretic Isolation of Discrete Au Nanocrystal/DNA Conjugates. *Nano Lett*. 2000;1(1):32-35. doi:10.1021/nl005508e

82. Claridge SA, Liang HW, Basu SR, Fréchet JMJ, Alivisatos AP. Isolation of Discrete Nanoparticle−DNA Conjugates for Plasmonic Applications. *Nano Lett*. 2008;8(4):1202-1206. doi:10.1021/nl0802032

83. Sperling RA, Pellegrino T, Li JK, Chang WH, Parak WJ. Electrophoretic separation of nanoparticles with a discrete number of functional groups. *Adv Funct Mater*. 2006;16(7):943-948. doi:10.1002/ADFM.200500589

84. Pellegrino T, Sperling RA, Alivisatos AP, Parak WJ. Gel Electrophoresis of Gold-DNA Nanoconjugates. *J Biomed Biotechnol*. 2007;26796. doi:10.1155/2007/26796

85. E. Sapsford K, Russ Algar W, Berti L, et al. Functionalizing Nanoparticles with Biological Molecules: Developing Chemistries that Facilitate Nanotechnology. *Chem Rev*. 2013;113(3):1904-2074. doi:10.1021/cr300143v

86. Wang W, Tao N. Detection, Counting, and Imaging of Single Nanoparticles. *Anal Chem*. 2013;86(1):2-14. doi:10.1021/ac403890n

87. C. Breger J, G. Ancona M, A. Walper S, et al. Understanding How Nanoparticle Attachment Enhances Phosphotriesterase Kinetic Efficiency. *ACS Nano*. 2015;9(8):8491-8503. doi:10.1021/acsnano.5b03459

88. Colangelo E, Comenge J, Paramelle D, Volk M, Chen Q, Lévy R. Characterizing Self-Assembled Monolayers on Gold Nanoparticles. *Bioconjug Chem*. 2016;28(1):11-22. doi:10.1021/acs.bioconjchem.6b00587

89. Sambrook J, Russell DW. Recovery of DNA from Agarose Gels: Electrophoresis onto DEAE-cellulose Membranes. *Cold Spring Harb Protoc*. 2006;2006(1). doi:10.1101/pdb.prot3214

90. Green MR, Sambrook J. Isolation of DNA fragments from polyacrylamide gels by the crush and soak method. *Cold Spring Harb Protoc*. 2019;2019(2). doi:10.1101/pdb.prot100479

91. Tautz D, Renz M. An optimized freeze-squeeze method for the recovery of DNA fragments from agarose gels. *Anal Biochem*. 1983;132(1). doi:10.1016/0003-2697(83)90419-0

92. Vogelstein B, Gillespie D. Preparative and analytical purification of DNA from agarose. *Proc Natl Acad Sci U S A*. 1979;76(2). doi:10.1073/pnas.76.2.615

93. Method of Oligonucleotide Purification. https://www.biosyn.com/tew/method-of-oligonucleotide-purification.aspx

94. Niihori Y, Uchida C, Kurashige W, Negishi Y. High-resolution separation of thiolate-protected gold clusters by reversed-phase high-performance liquid chromatography. *Physical Chemistry Chemical Physics*. 2016;18(6). doi:10.1039/c5cp04660b

95. Niihori Y, Shima D, Yoshida K, et al. High-performance liquid chromatography mass spectrometry of gold and alloy clusters protected by hydrophilic thiolates. *Nanoscale*. 2018;10(4):1641-1649. doi:10.1039/c7nr07840d

96. Niihori Y, Matsuzaki M, Uchida C, Negishi Y. Advanced use of high-performance liquid chromatography for synthesis of controlled metal clusters. *Nanoscale*. 2014;6(14):7889-7896. doi:10.1039/C4NR01144A

97. Victoria L. Jimenez, Michael C. Leopold †, Carolyn Mazzitelli, James W. Jorgenson and, Murray* RW. HPLC of Monolayer-Protected Gold Nanoclusters. *Anal Chem*. 2002;75(2):199-206. doi:10.1021/AC0260589

98. Zhang Y, Shuang S, Dong C, Lo CK, Paau MC, Choi MMF. Application of HPLC and MALDI-TOF MS for Studying As-Synthesized Ligand-Protected Gold Nanoclusters Products. *Anal Chem*. 2009;81(4):1676-1685. doi:10.1021/AC8026349

99. Niihori Y, Matsuzaki M, Pradeep T, Negishi Y. Separation of Precise Compositions of Noble Metal Clusters Protected with Mixed Ligands. *J Am Chem Soc*. 2013;135(13):4946-4949. doi:10.1021/JA4009369

100. Martin M. F. Choi †, Alicia D. Douglas and, Murray* RW. Ion-Pair Chromatographic Separation of Water-Soluble Gold Monolayer-Protected Clusters. *Anal Chem*. 2006;78(8):2779-2785. doi:10.1021/AC052167M

101. Niihori Y, Kikuchi Y, Shima D, et al. Separation of Glutathionate-Protected Gold Clusters by Reversed-Phase Ion-Pair High-Performance Liquid Chromatography. *Ind Eng Chem Res*. 2017;56(4):1029-1035. doi:10.1021/acs.iecr.6b03814

102. Gilar M, Fountain KJ, Budman Y, et al. Ion-pair reversed-phase high-performance liquid chromatography analysis of oligonucleotides:: Retention prediction. *J Chromatogr A*. 2002;958(1-2):167-182. doi:10.1016/S0021-9673(02)00306-0

103. Donegan M, Nguyen JM, Gilar M. Effect of ion-pairing reagent hydrophobicity on liquid chromatography and mass spectrometry analysis of oligonucleotides. *J Chromatogr A*. 2022;1666:462860. doi:10.1016/J.CHROMA.2022.462860

104. Enmark M, Harun S, Samuelsson J, et al. Selectivity limits of and opportunities for ion pair chromatographic separation of oligonucleotides. *J Chromatogr A*. 2021;1651:462269. doi:10.1016/J.CHROMA.2021.462269

105. Close ED, Nwokeoji AO, Milton D, et al. Nucleic acid separations using superficially porous silica particles. *J Chromatogr A*. 2016;1440:135. doi:10.1016/J.CHROMA.2016.02.057

106. Macnair JE, Lewis KC, Jorgenson JW, et al. Effect of Pressure, Particle Size, and Time on Optimizing Performance in Liquid Chromatography. *Anal Chem*. 2009;81(13):5342-5353. doi:10.1021/AC9001244

107. Gong L. Analysis of oligonucleotides by ion-pairing hydrophilic interaction liquid chromatography/electrospray ionization mass spectrometry. *Rapid Communications in Mass Spectrometry*. 2017;31(24):2125-2134. doi:10.1002/rcm.8004

108. Fountain KJ, Gilar M, Gebler JC. Analysis of native and chemically modified oligonucleotides by tandem ion-pair reversed-phase high-performance liquid chromatography/electrospray ionization mass spectrometry. *Rapid Communications in Mass Spectrometry*. 2003;17(7):646-653. doi:10.1002/rcm.959

109. Huber CG, Krajete A. Analysis of nucleic acids by capillary ion-pair reversed-phase HPLC coupled to negative-ion electrospray ionization mass spectrometry. *Anal Chem*. 1999;71(17):3730-3739. doi:10.1021/ac990378j

110. Rival J V., Mymoona P, Lakshmi KM, Nonappa, Pradeep T, Shibu ES. Self-Assembly of Precision Noble Metal Nanoclusters: Hierarchical Structural Complexity, Colloidal Superstructures, and Applications. *Small*. 2021;17(27). doi:10.1002/smll.202005718

111. Yoon B, Luedtke WD, Barnett RN, et al. Hydrogen-bonded structure and mechanical chiral response of a silver nanoparticle superlattice. *Nat Mater*. 2014;13(8). doi:10.1038/nmat3923

112. Qiu Y, Chen Y, Zhang GGZ, Yu L, Mantri R V. *Developing Solid Oral Dosage Forms: Pharmaceutical Theory and Practice: Second Edition*.; 2016.

113. Wu Z, Yao Q, Zang S, Xie J. Directed Self-Assembly of Ultrasmall Metal Nanoclusters. *ACS Mater Lett*. 2019;1(2). doi:10.1021/acsmaterialslett.9b00136

114. Grzelczak M, Vermant J, Furst EM, Liz-Marzán LM. Directed self-assembly of nanoparticles. *ACS Nano*. 2010;4(7). doi:10.1021/nn100869j

115. Ouyang X, Wang M, Guo L, et al. DNA Nanoribbon-Templated Self-Assembly of Ultrasmall Fluorescent Copper Nanoclusters with Enhanced Luminescence. *Angewandte Chemie - International Edition*. 2020;59(29). doi:10.1002/anie.202003905

116. Mirkin CA, Letsinger RL, Mucic RC, Storhoff JJ. *A DNA-Based Method for Rationally Assembling Nanoparticles into Macroscopic Materials*.

117. Watson JD, Crick FHC. Molecular Structure of Nucleic Acids: A Structure for Deoxyribose Nucleic Acid. *Nature 1953 171:4356*. 1953;171(4356):737-738. doi:10.1038/171737a0

118. Pauling L, Corey RB. Structure of the Nucleic Acids. *Nature*. 1953;171(4347):346. doi:10.1038/171346a0

119. Donald Voet, Judith G. Voet CWP. Fundamentals of Biochemistry: Life at the Molecular Level, 5th Edition. Published online 2016:1184.

120. Philips R, Kondev J, Theriot J. *Physical Biology of the Cell*. Garland Science; 2009.

121. Babatunde B, Arias DS, Cagan J, Taylor RE. Generating dna origami nanostructures through shape annealing. *Applied Sciences (Switzerland)*. 2021;11(7). doi:10.3390/app11072950

122. Seeman NC. Nucleic acid junctions and lattices. *J Theor Biol*. 1982;99(2):237-247. doi:10.1016/0022-5193(82)90002-9

123. Goodman RP, Turberfield AJ. The single-step synthesis of a DNA tetrahedron. *Chem Commun (Camb)*. 2004;4(12):1372-1373. doi:10.1039/B402293A

124. Shih WM, Quispe JD, Joyce GF. A 1.7-kilobase single-stranded DNA that folds into a nanoscale octahedron. *Nature 2004 427:6975*. 2004;427(6975):618-621. doi:10.1038/nature02307

125. Seeman NC. DNA nanotechnology: novel DNA constructions. *Annu Rev Biophys Biomol Struct*. 1998;27:225-248. doi:10.1146/annurev.biophys.27.1.225

126. Zhang Y, Seeman NC. Construction of a DNA-Truncated Octahedron. *J Am Chem Soc*. 1994;116(5):1661-1669. doi:10.1021/JA00084A006/ASSET/JA00084A006.FP.PNG_V03

127. Chen J, Seeman NC. Synthesis from DNA of a molecule with the connectivity of a cube. *Nature 1991 350:6319*. 1991;350(6319):631-633. doi:10.1038/350631a0

128. Rothemund PWKK. *Folding DNA to Create Nanoscale Shapes and Patterns*. Vol 440. Nature Publishing Group; 2006:297-302. doi:10.1038/nature04586

129. Dietz H, Douglas SM, Shih WM. Folding DNA into twisted and curved nanoscale shapes. *Science (1979)*. 2009;325(5941):725-730. doi:10.1126/SCIENCE.1174251/SUPPL_FILE/DIETZ.SOM.PDF

130. Andersen ES, Dong M, Nielsen MM, et al. Self-assembly of a nanoscale DNA box with a controllable lid. *Nature*. 2009;459(7243):73-76. doi:10.1038/nature07971

131. Hong F, Zhang F, Liu Y, Yan H. DNA Origami: Scaffolds for Creating Higher Order Structures. *Chem Rev*. 2017;117(20). doi:10.1021/acs.chemrev.6b00825

132. Ke Y, Sharma J, Liu M, Jahn K, Liu Y, Yan H. Scaffolded DNA origami of a DNA tetrahedron molecular container. *Nano Lett*. 2009;9(6). doi:10.1021/nl901165f

133. Han D, Pal S, Liu Y, Yan H. Folding and cutting DNA into reconfigurable topological nanostructures. *Nat Nanotechnol*. 2010;5(10). doi:10.1038/nnano.2010.193

134. Andersen ES, Dong M, Nielsen MM, et al. DNA origami design of dolphin-shaped structures with flexible tails. *ACS Nano*. 2008;2(6):1213-1218. doi:10.1021/nn800215j

135. Han D, Pal S, Nangreave J, Deng Z, Liu Y, Yan H. DNA origami with complex curvatures in three-dimensional space. *Science (1979)*. 2011;332(6027). doi:10.1126/science.1202998

136. Han D, Pal S, Liu Y, Yan H. Folding and cutting DNA into reconfigurable topological nanostructures. *Nature Nanotechnology 2010 5:10*. 2010;5(10):712-717. doi:10.1038/nnano.2010.193

137. Han D, Pal S, Liu Y, Yan H. Folding and cutting DNA into reconfigurable topological nanostructures. *Nature Nanotechnology 2010 5:10*. 2010;5(10):712-717. doi:10.1038/nnano.2010.193

138. Han D, Pal S, Nangreave J, Deng Z, Liu Y, Yan H. DNA origami with complex curvatures in three-dimensional space. *Science (1979)*. 2011;332(6027):342-346. doi:10.1126/SCIENCE.1202998/SUPPL_FILE/HAN_SOM.PDF

139. Liu Q, Song C, Wang ZG, Li N, Ding B. Precise organization of metal nanoparticles on DNA origami template. *Methods*. 2014;67(2):205-214. doi:10.1016/j.ymeth.2013.10.006

140. J. Ackerson C, D. Jadzinsky P, J. Jensen G, D. Kornberg R. Rigid, Specific, and Discrete Gold Nanoparticle/Antibody Conjugates. *J Am Chem Soc*. 2006;128(8):2635-2640. doi:10.1021/ja0555668

141. Gorshkov K, Susumu K, Chen J, et al. Quantum Dot-Conjugated SARS-CoV-2 Spike Pseudo-Virions Enable Tracking of Angiotensin Converting Enzyme 2 Binding and Endocytosis. *ACS Nano*. 2020;14(9):12234-12247. doi:10.1021/acsnano.0c05975

142. Mullen DG, Fang M, Desai A, James R. Baker Jr, Orr BG, Holl MMB. A Quantitative Assessment of Nanoparticle−Ligand Distributions: Implications for Targeted Drug and Imaging Delivery in Dendrimer Conjugates. *ACS Nano*. 2010;4(2):657-670. doi:10.1021/NN900999C

143. Rahmani P, Goodlad M, Zhang Y, Li Y, Ye T. One-Step Ligand-Exchange Method to Produce Quantum Dot–DNA Conjugates for DNA-Directed Self-Assembly. *ACS Appl Mater Interfaces*. 14(42):47359-47368. doi:10.1021/acsami.2c10580

144. Qin WJ, Yung LYL. Nanoparticle-DNA conjugates bearing a specific number of short DNA strands by enzymatic manipulation of nanoparticle-bound DNA. *Langmuir*. 2005;21(24):11330-11334. doi:10.1021/LA051630N

145. Ding B, Deng Z, Yan H, Cabrini S, Zuckermann RN, Bokor J. Gold Nanoparticle Self-Similar Chain Structure Organized by DNA Origami. *J Am Chem Soc*. 2010;132(10):3248-3249. doi:10.1021/ja9101198

146. Hung AM, Micheel CM, Bozano LD, Osterbur LW, Wallraff GM, Cha JN. Large-area spatially ordered arrays of gold nanoparticles directed by lithographically confined DNA origami. Published online 2010. doi:10.1038/NNANO.2009.450

147. Pal S, Deng Z, Ding B, Yan H, Liu Y. DNA-Origami-Directed Self-Assembly of Discrete Silver-Nanoparticle Architectures. *Angewandte Chemie*. 2010;122(15):2760-2764. doi:10.1002/ANGE.201000330

148. Pilo-Pais M, Goldberg S, Samano E, Labean TH, Finkelstein G. Connecting the nanodots: Programmable nanofabrication of fused metal shapes on DNA templates. *Nano Lett*. 2011;11(8). doi:10.1021/nl202066c

149. Bui H, Onodera C, Kidwell C, et al. Programmable periodicity of quantum dot arrays with DNA origami nanotubes. *Nano Lett*. 2010;10(9). doi:10.1021/nl101079u

150. Steinhauer C, Jungmann R, Sobey TL, Simmel FC, Tinnefeld P. DNA Origami as a Nanoscopic Ruler for Super-Resolution Microscopy. *Angewandte Chemie International Edition*. 2009;48(47):8870-8873. doi:10.1002/anie.200903308

151. Maune HT, Han SP, Barish RD, et al. Self-assembly of carbon nanotubes into two-dimensional geometries using DNA origami templates. *Nat Nanotechnol*. 2010;5(1). doi:10.1038/nnano.2009.311

1.7. Appendix

1.7.1. Energy transfer

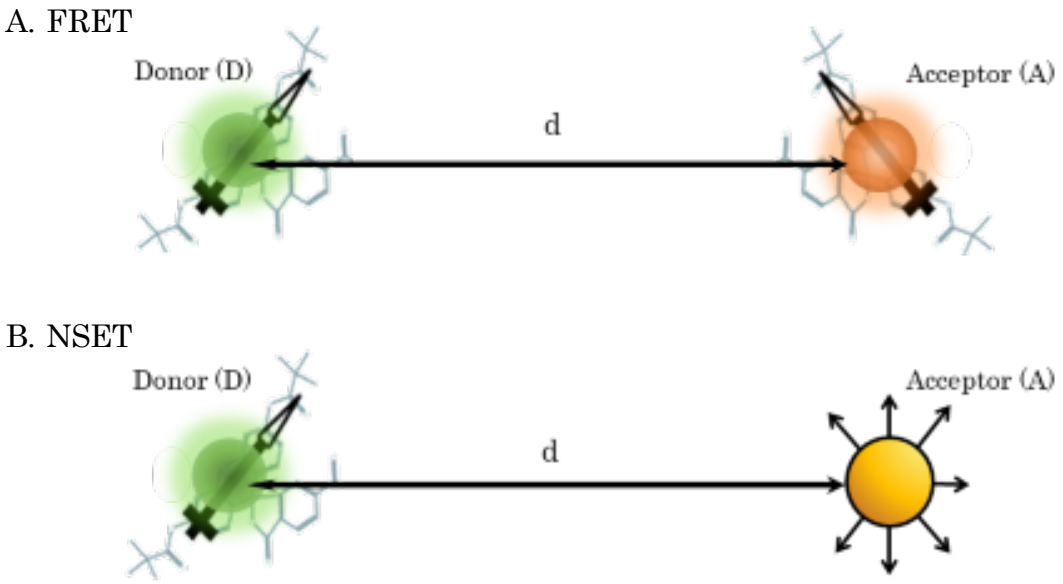

Figure 1.1. A schematic comparison of the (A) FRET and (B) NSET mechanisms

Energy transfer is a non-radiative distance-dependent energy transfer from a donor to an acceptor[1–3]. The donor is typically an excited fluorophore, while the acceptor can be a variety of materials, such as lower-energy fluorophores, quenchers, or metal nanomaterials. Energy transfer results in the reduction of fluorescent emission of the donor and, if paired with a lower-energy fluorophore, an emission from the acceptor. Energy transfer has been used extensively to monitor *in vitro* and *in vivo* processes such as diffusion dynamics, cellular membrane dynamics, and DNA hybridization[4–8]. Energy transfer studies dependent on coupled fluorophores are limited to smaller separation distances[9]. Initial studies have indicated that AuNCs can potentially have a significantly larger detection range than traditional FRET pairs[10–12]. Combined with their small size, low toxicity, and photostability AuNCs could greatly expand the utility of energy transfer applications. In this section, we review both Förster resonance energy transfer (FRET) and nanosurface energy transfer (NSET) to understand coupling mechanism of AuNCs better.

1.7.1. Förster resonance energy transfer (FRET)

The first published observations of what we would now consider fluorescence energy transfer (FRET) occurred over 100 years ago. Researchers excited a mercury vapor in the presence of thallium and observed that it was the thallium that fluoresced[13]. Several similar experiments with additional publications afterward attempted to explain the phenomenon throughout the 1920s. Of these, Jean Batiste Perrin published a theory closest to the FRET model. The most critical error of his theory is that it relied on an exact resonance between donor and acceptor. His son made the next theoretical advance in 1933 by incorporating the need for overlapping spectra between the donor emission into his father's model. The continued reliance on exact resonance between donor and acceptor overestimated the transfer efficiency[14]. Förster's theory was able to tie this spectral overlap with a quantum mechanical treatment of collisions that dismissed the need for an exact resonance. His theoretical model is consistent with the experimental distance dependence and efficiency of previously published data[15]. The FRET energy transfer rate is expressed with Equation 1.1.

$$k_{FRET} = \frac{9\,000(ln\,10)\,\kappa^2\Phi_D}{128\pi^5\eta^4 N_A d^6 \tau_D} J(\lambda) \qquad (1.1)$$

The variables and units for the FRET equations are summarized in Table 1.

Table 1.1. Summary of variables and units for FRET equations.

Variable		Value	Unit
Φ_D	the quantum yield of door		
η	refractive index	1.33	
d	separation distance		$\AA$
N_A	Avogadro's number	6.022×10^{23}	mol^{-1}
τ_D	donor lifetime		s
κ	orientation factor	2/3	
$J(\lambda)$	Overlap integral		$M^{-1}cm^{-1}nm^4$
R_0	Förster's distance		$\AA$

The value of κ can vary from 0 to 4 depending on whether the relative between donor and acceptor dipole orientation is perpendicular or parallel. $\kappa = 2/3$ is the generally agreed upon and commonly used value for FRET experiments conducted in solution [15]. The value of η is the refractive index of water. The spectral overlap, $J(\lambda)$, is expressed in Equation 1.2:

$$J(\lambda) = \int_0^\infty f_{donor(\lambda)}\varepsilon_a(\lambda)\lambda^4 d\lambda \qquad (1.2)$$

where $f_{\text{donor}}(\lambda)$ is the normalized fluorescent emission of the donor, and $\varepsilon_A(\lambda)$ is the normalized absorption spectrum of the acceptor. The Förster's distance (R_0)

is the critical distance at which spontaneous emission and energy transfer are equally probable. Therefore, to solve for R_0 we set k_{FRET} equal to τ_D^{-1}, which gives us Equation 1.3:

$$R_0 = \left(\frac{9\,(ln\,10)\,\kappa^2 \Phi_{donor}}{128\pi^5 \eta^4 N_A} J(\lambda) \right)^{\frac{1}{6}} \tag{1.3}$$

FRET is now a ubiquitous tool for studying biological systems, but it took decades after Förster's published theory for it to be incorporated into such studies. 1991RET was used as a spectroscopic ruler in living cells to study signaling pathways[16]. FRET is now used in various microscopy and imaging techniques to examine single molecule interactions to whole tissues for diagnostics[5,17–19].

There are limitations to the applicability of FRET probes. The most significant is the limited separation distance between FRET pairs. FRET imaging techniques typically have high signal-to-noise ratios. Most FRET pairs are limited to distances of 10 Å, which limits their use in studying macromolecular systems. Most molecular fluorophores used in FRET assays have small Stokes shifts, making them susceptible to self-quenching behavior at high concentrations[20]. AuNCs show promise in addressing some of these limitations.

1.7.2. Nanosurface energy transfer (NSET)

Nanosurface energy transfer (NSET) is a mechanism similar to FRET. Where FRET is the coupling between two oscillating dipoles, NSET is the more efficient coupling between an oscillating dipole and the conduction electrons of an accepting metal. The NSET model is an extension of one developed by Persson and Lang to describe the damping of the rate of vibration due to the excitation of electron-hole pairs in the metal [21]. The rate of energy transfer (k_{ET}) is roughly proportional to the interaction elements of the donor and acceptor, where a point dipole will have a distance-dependent interaction of d^{-3}, and a 2D surface will have a distance-dependent interaction of d^{-1}. Thus, NSET has a distance-dependent rate of d^{-4}, and FRET has a distance-dependent rate of d^{-6}. Their energy transfer rate is summarized by Equation 1.4:

$$k_{NSET} = 0.225 \frac{c^3 \Phi_D}{\omega_{dye}^2 \omega_F k_F d^4 \tau_D} \quad (1.4)$$

Table 1.2. Summary of variables and units for NSET equations.

Variable		Value	Unit
c	speed of light	3.00×10^8	$m \cdot s^{-1}$
Φ_D	quantum yield		
d	separation distance		m
ω_{dye}	angular frequency of donor emission		sec^{-1}
ω_F	Fermi frequency of the metal	1.2×10^{10}	m^{-1}
k_F	Fermi wave vector of the metal	8.4×10^{15}	s^{-1}
τ_D	donor lifetime		s
d_0	critical distance		m

The variables for the NSET equations are summarized in Tables 2[7,21,22]. The critical distance (d_0) is the separation distance at which the energy transfer efficiency equals 50%. It can be calculated from *Equation 1.5*.

$$d_0 = \left(0.225 \frac{c^3 \Phi_{dye}}{\omega_{dye}^2 \omega_F k_F}\right)^{1/4} \quad (1.5)$$

In 2006, Strouse et al. confirmed that NSET is the energy transfer mechanism between 1.5 nm AuNCs and fluorophores. In this experiment, they successfully used separation distances up to 23.2 nm to probe the validity of the NSET model [7]. This is more than twice the typical distance limit of FRET pairs. The easily conjugatable surface of AuNCs led to quickly incorporating this new tool into biological studies. In 2008 it was used to study how ribonucleic acid (RNA) folds in the presence of Mg^{2+} ions[23]. It has since been used in biosensing, imaging, and detecting[24–26]. One of the most recent studies has been combined with a FRET acceptor to triangulate viral gene replication in living cells[27].

Energy transfer efficiency is the fraction of photon energy absorbed by the donor and transferred to the acceptor[3]. It is a fundamental parameter used to express the proximity of the donor and acceptor in an energy transfer system. If k_{ET} is the rate of energy transfer from a single donor to a single acceptor, the ET efficiency for a system with a single donor and multiple acceptors can be expressed as:

$$E = \frac{\sum_i k_{D \to A_i}}{\sum_i k_{D \to A_i} + k_{D_0}} \quad (1.6)$$

$$k_{D\to A_i} = k_{D_0}\left(\frac{d_0}{d}\right)^n \tag{1.7}$$

where $k_{D\to A_i}$ is the ET rate between the donor and a single acceptor, k_{D_0} is the decay rate of the donor in the absence of an acceptor. The "n" in equation 1.7 depends on which ET mechanism is employed; n=4 for NSET and n=6 for FRET.

1.7.2. Appendix references

1. Selvin PR. The renaissance of fluorescence resonance energy transfer. *Nat Struct Biol*. 2000;7(9):730-734. doi:10.1038/78948

2. Clapp AR, Medintz IL, Mattoussi H. Förster resonance energy transfer investigations using quantum-dot fluorophores. *ChemPhysChem*. 2006;7(1):47-57. doi:10.1002/cphc.200500217

3. Lakowicz JR. *Principles of Fluorescence Spectroscopy*. Springer; 2006. doi:10.1007/978-0-387-46312-4

4. Pons T, Medintz IL, Sapsford KE, et al. On the Quenching of Semiconductor Quantum Dot Photoluminescence by Proximal Gold Nanoparticles. Published online 2007. https://pubs.acs.org/doi/full/10.1021/nl071729+

5. Ha T. Single-Molecule Fluorescence Resonance Energy Transfer. *METHODS*. 2001;25:78-86. doi:10.1006/meth.2001.1217

6. Weiss S. Fluorescence spectroscopy of single biomolecules. *Science*. 1999;283(5408):1676-1683. doi:10.1126/SCIENCE.283.5408.1676

7. T. L. Jennings, M. P. Singh and, Strouse* GF, Jennings TL, Singh MP, Strouse GF. Fluorescent lifetime quenching near d = 1.5 nm gold nanoparticles: Probing NSET validity. *J Am Chem Soc*. 2006;128(16):5462-5467. doi:10.1021/ja0583665

8. Sapsford KE, Tyner KM, Dair BJ, Deschamps JR, Medintz IL. Analyzing nanomaterial bioconjugates: A review of current and emerging purification and characterization techniques. *Anal Chem*. 2011;83(12):4453-4488. doi:10.1021/AC200853A/ASSET/IMAGES/LARGE/AC-2011-00853A_0011.JPEG

9. Rowland CE, Brown CW, Medintz IL, Delehanty JB. Intracellular FRET-based Probes: A Review. http://iopscience.iop.org/article/10.1088/2050-6120/3/4/042006/ampdf

10. Yun CS, Javier A, Jennings T, et al. Nanometal surface energy transfer in optical rulers, breaking the FRET barrier. *J Am Chem Soc*. 2005;127(9):3115-3119. doi:10.1021/ja043940i

11. Chowdhury S, Wu Z, Jaquins-Gerstl A, et al. Wavelength Dependence of the Fluorescence Quenching Efficiency of Nearby Dyes by Gold Nanoclusters and Nanoparticles: The Roles of Spectral Overlap and Particle Size. *J Phys Chem C*. 2011;115:20105-20112. doi:10.1021/jp204836w

12. Oh E, Huston AL, Shabaev A, et al. Energy Transfer Sensitization of Luminescent Gold Nanoclusters: More than Just the Classical Förster Mechanism. *Sci Rep*. 2016;6:35538. doi:10.1038/srep35538

13. Clegg RM. The history of FRET : From conception through the labors of birth. *Rev Fluoresc*. 2006;3.

14. Jones GA, Bradshaw DS. Resonance energy transfer: From fundamental theory to recent applications. *Front Phys*. 2019;7(JULY). doi:10.3389/fphy.2019.00111

15. Förster Th. Zwischenmolekulare Energiewanderung und Fluoreszenz. *Ann Phys*. 1948;437(1-2):55-75. doi:10.1002/andp.19484370105

16. Adams SR, Harootunian AT, Buechler YJ, Taylor SS, Tsien RY. Fluorescence ratio imaging of cyclic AMP in single cells. *Nature*. 1991;349(6311). doi:10.1038/349694a0

17. McGinty J, Stuckey DW, Soloviev VY, et al. In vivo fluorescence lifetime tomography of a FRET probe expressed in mouse. *Biomed Opt Express*. 2011;2(7). doi:10.1364/boe.2.001907

18. Mills JD, Stone JR, Rubin DG, et al. Illuminating protein interactions in tissue using confocal and two-photon excitation fluorescent resonance energy transfer microscopy. *J Biomed Opt*. 2003;8(3). doi:10.1117/1.1584443

19. Larionov S, Wielgat P, Wang Y, Thal DR, Neumann H. Spatially pathogenic forms of tau detected in Alzheimer's disease brain tissue by fluorescence lifetime-based Förster resonance energy transfer. *J Neurosci Methods*. 2010;192(1). doi:10.1016/j.jneumeth.2010.07.021

20. Penzkofer A, Lu ' Y. *FLUORESCENCE QUENCHING OF RHODAMINE 6C IN METHANOL AT HIGH CONCENTRATION*. Vol 103.; 1986.

21. Persson BNJ, Lang ND. Electron-hole-pair quenching of excited states near a metal. *Phys Rev B*. 1982;26(10):5409-5415. doi:10.1103/PhysRevB.26.5409

22. Breshike CJ, Riskowski RA, Strouse GF. Leaving Fö rster Resonance Energy Transfer Behind: Nanometal Surface Energy Transfer Predicts the Size-Enhanced Energy Coupling between a Metal Nanoparticle and an Emitting Dipole. *J Phys Chem C*. 2013;117. doi:10.1021/jp407259r

23. Griffin J, Ray PC. Gold Nanoparticle Based NSET For Monitoring Mg 2+ Dependent RNA Folding. doi:10.1021/jp8059322

24. Lee H, Lee K, Kim IK, Park TG. Synthesis, characterization, and in vivo diagnostic applications of hyaluronic acid immobilized gold nanoprobes. *Biomaterials*. 2008;29(35). doi:10.1016/j.biomaterials.2008.08.038

25. Darbha GK, Ray A, Ray PC. Gold nanoparticle-based miniaturized nanomaterial surface energy transfer probe for rapid and ultrasensitive detection of mercury in soil, water, and fish. *ACS Nano*. 2007;1(3). doi:10.1021/nn7001954

26. van de Looij SM, Hebels ER, Viola M, Hembury M, Oliveira S, Vermonden T. Gold Nanoclusters: Imaging, Therapy, and Theranostic Roles in Biomedical Applications. *Bioconjug Chem*. 2022;33(1):4-23. doi:10.1021/acs.bioconjchem.1c00475

27. Zheng LL, Shuai XJ, Liu Y, et al. One-donor-two-acceptors coupled energy transfer nanoprobe for recording of viral gene replication in living cells. *Chemical Engineering Journal*. 2022;434. doi:10.1016/j.cej.2022.134658

Chapter 2

Ligand Exchange Reactions of Thiolated DNA on Monolayer Protected Gold Nanoclusters

2.1. Introduction

The ligand monolayer contributes to the physical and chemical properties of AuNCs[1]. These properties determine the suitability of AuNCs for delivery and sensing applications. To impart these properties to the AuNCs, LER that can conjugate AuNCs to thiol-functionalized biomolecules is a promising route. AuNC-DNA conjugates are of particular interest for constructing self-assembled materials. The specificity of nucleic acid base-pairing allows for the programmed assembly of multiple nanomaterials on a single platform. Therefore, LERs incorporating thiol-modified ssDNA into the AuNC monolayer would serve as a promising route toward programmable self-assembly of AuNCs into multifunctional materials [2,3].

Despite the promise of AuNC-DNA materials there has been little research into how variables such as stoichiometric ratios and salt concentrations affect yields. To date there have only been two studies that tested the viability of such LERs [4,5]. One of the challenges specific to DNA LER studies is that the DNA ligand is a bio-polymer with substantially more significant nonvalent interactions with AuNCs and each other. E.g., the sequence-specific properties that make DNA well-suited for self-assembly applications mean that each sequence could behave differently in the LER. Hence the behaviors of LERs between DNA ligands and monolayer-protected AuNCs cannot be readily extrapolated from those between small molecule ligands and AuNCs.

On the other hand, the surface functionalization of gold nanoparticles (AuNP) with thiolated DNA ligands has been extensively studied. Those studies established how DNA sequences affect conjugation yields, stability, and surface coverage[6–10]. However, insights from those studies may not be easily extrapolated to LERs involving atomically precise AuNCs and DNA ligands as those studies focus on larger nanoparticles (5 nm or larger) capped with more labile ligands such as citrate and phosphine, where the interactions between DNA ligands and the surface of AuNP are likely substantially different.

To fill the gap in the mechanistic understanding of thiolated DNA LERs on monolayer-protected AuNCs, here we leverage the small size of monolayer-protected Au_{25} NCs to enable PAGE and densitometric analysis to characterize the distribution of AuNCs with discrete numbers of LDNA under different LER conditions. We determined that both AuNC and salt concentrations affect ligand exchange products. The highest yields of AuNC-DNA conjugates were achieved with high ratios of AuNC to DNA. The DNA load per conjugated AuNC was maximized with a low AuNC to DNA with conditions that minimized electrostatic repulsion between anionic oligonucleotide sequences

and AuNCs. The highest yields of monoconjugates can be achieved in salt-free solutions with high AuNC-to-DNA ratios. Our results show that yield and loading vary with DNA sequence. There is some evidence that noncovalent interactions play a role in the DNA load per conjugate. The poly-thiamine sequence was an interesting outlier under all LER conditions and should be investigated further. Hopefully, the insights in this chapter will provide the groundwork for advancing AuNC-DNA conjugation research.

2.2. Methods and materials

2.2.1. DNA preparation

Table 2.1. Summary of DNA sequences used in experiments.

Description	Name Length	DNA Sequence and Modifications
Thiolated 16 mer ssDNA	**M16** 16 mer	5' – thiol – C6 – TTTT TTGG GCGG TTGG – 3'
Thiolated poly thiamine ssDNA	**Poly-T** 16 mer	5' – thiol – C6 – TTTT TTTT TTTT TTTT – 3'
Thiolated 29 mer ssDNA	**M29** 29 mer	5' – thiol – C6 – TTTT TGCA TGAC GAGT GCCT CATC G – 3'
Thiolated 48 mer ssDNA	**M48** 48 mer	5' – thiol – C6 – TTTT TTGG GCGG TTGG TTTT TTGG GCGG TTGG TTTT TTGG GCGG TTGG – 3'

All oligonucleotide sequences were purchased from Integrated DNA Technologies (Coralville, IA). The sample arrived lyophilized in disulfide form and was then reconstituted to 200 µM with ultrapure water from the Barnstead Nanopure system (Thermo Fisher Scientific, Houston, TX, US). The DNA sequences used in these experiments are summarized in Table 2.1.

We reduced the disulfide form to the thiol form needed for the AuNC ligand exchange by mixing the TssDNA with Tris (2 carboxyethyl) phosphine hydrochloride (TCEP) (Thermo Fisher) in a 200 µL PCR tube in a 1000:1 TCEP to DNA ratio. The PCR tube was backfilled with nitrogen gas and vortexed for 30 minutes. The reduced TssDNA was purified using a 3 kDa molecular cutoff

filter (Sigma Millipore, St. Louis, MO, US). The TCEP/TssDNA solution was added to the filter, filled to 450 µL, and spun for 30 minutes at 14,000×g. We repeated these steps three times. 250 µL was added and spun for 5 minutes at 14,000×g for the final solvent exchange. After the last spin, the filter was inverted and centrifuged at 10,000×g for 5 minutes. Multiple solvent exchange steps are necessary to remove any remaining TCEP; otherwise, it will degrade the AuNC in the ligand exchange step. The final TssDNA concentration was determined using a NanoDrop™ ND-1000 spectrophotometer (Thermo Fisher Scientific).

2.2.2. Gold nanocluster synthesis

$Au_{25}(Captopril)_{18}$ samples were synthesized and characterized by the Jin research group according to methods described in a previous publication[11]. $HAuCl_4 \cdot 3H_2O$ (78.7 mg) and TOABr (126.8 mg) were stirred vigorously in 10 mL of methanol. After 20 minutes, 5 mL of methanol containing 217.2 mg of captopril was injected into the solution. After 30 minutes, 2 mmol of $NaBH_4$ was added, and the solution was mixed for another 8 hours. The mixture was then centrifuged, and the AuNCs were precipitated with a methanol extraction.

2.2.3. Preparation of DNA-conjugated gold nanoclusters

First, ultrapure water was added to PAGE purified and desiccated AuNCs. The AuNC solution concentration was determined using Nanodrop and the extinction coefficient at 310 nm, $\varepsilon_{310} = 3.6 \times 10^4\ M^{-1}\ cm^{-1}$. Next, 50 µL ligand exchange solutions were made with ssDNA, AuNCs, and NaCl in a 200 µL PCR tube. All LER solutions were made with a final concentration of 5 µM ssDNA. The corresponding ratios of ssDNA to AuNC and salt concentration are indicated in the figures. The PCR tube was then backfilled with nitrogen gas and vortexed gently overnight.

2.2.4. Transmission electron microscopy (TEM)

Transmission electron microscopy (TEM) imaging of gold nanoclusters was carried out using a Talos F200C G2 transmission electron microscope operating at 200 kV in UC Merced Imaging and Microscopy Facility. Typically, 4-5 µl of the sample was deposited onto an Argon plasma-treated formvar/carbon-coated (copper mesh) grid (Ted Pella, Inc., Redding, CA, USA; prod no. 01753-f) for up to 5 min. The excess liquid was then blotted off, and the grid was washed and stained using a 2% aqueous uranyl formate solution and let dry overnight. ImageJ software was used to measure the diameter of the AuNCs.

2.2.5. Polyacrylamide gel electrophoresis (PAGE)

PAGE experiments were carried out using Enduro Vertical Gel Electrophoresis System (Labnet, Edison, NJ, US) with 10 × 10 cm Novex Wedgewell 10%-20% Bis-tris gels. 8 µL of glycerol was added to 20 µL of ligand exchange solution and controls. Samples were run at 80 V for 220 minutes in 1×TBE buffer (Thermo Fisher Scientific). In addition, the gel was stained with 10 µL of SYBR Green II 10,000× stain (Invitrogen, Thermo Fisher Scientific, Houston, TX, US) in 100 mL 0.5× TBE buffer for five minutes. It was then visualized on an Ultra Slim transilluminator (New England BioGroup, Atkinson, NH, US) with a 470 nm wavelength blue light.

2.2.6. Dynamic light scattering (DLS) measurements

All DLS experiments were performed using a Malvern Zetasizer Nano-S90 (Malvern Instruments Ltd., Malvern, UK). The hydrodynamic diameters of the AuNCs and fAuNCs were measured at a 50 µM concentration in a 250 mM NaCl solution. Measurements were taken in a 50 µL cuvette using a laser wavelength of 633 nm, a scattering angle of 90°, a room temperature of 25°C, and an accumulation time of 100 sec.

2.3. Results and discussion

Our goal for this chapter was to provide a detailed characterization of LERs involving thiolated oligonucleotides and AuNCs. We can broadly divide the work into two parts. The first examines fAuNC yields and ligand speciation for four oligonucleotide sequences under varied salt and AuNC concentrations. We found the sequence to be a surprisingly significant determinant in yield and speciation. The second section investigates whether the initial findings can be justified with cooperative binding models. We found that the oligonucleotide sequence determines the ligands' cooperativity; the higher the cooperativity, the more diverse the fAuNC population.

2.3.1. Ligand exchange reactions (LERs) produce AuNCs conjugated with discrete numbers of ssDNA ligands.

The $Au_{25}(Captopril)_{18}$ clusters used in these experiments were synthesized and characterized by the Jin Group at Carnegie-Mellon. These nanoclusters

are water-soluble, stable at temperatures up to 80 °C, and stable under salt and pH changes[12]. We characterized AuNC size with TEM and analyzed the size distribution using ImageJ software. According to the histogram's Gaussian fit seen in Figure 2.1.b, the average size of the AuNCs is 1.09 ± 0.36 nm. These results agree with previously published papers studying Au_{25} clusters [13].

We first characterized the LER between AuNCs and thiolated ssDNA using PAGE. Gel electrophoresis (GE) is a widely used technique to characterize the bioconjugation of nanomaterials. This technique uses a gel matrix and electric field to separate mixtures by mass, shape, and charge. Highly charged small molecules travel more quickly through the matrix, while larger, less charged molecules travel more slowly. For an oligonucleotide bioconjugation, attaching each additional ssDNA ligand to a nanoparticle increases its effective size and slows its electrophoretic mobility through the gel. Zanchet *et al.* were the first to demonstrate that GE could isolate discrete bioconjugation products[14]. Using agarose gel and AuNPs bioconjugated with thiolated oligonucleotides, their study showed that each band represented AuNPs with a specific number of DNA-ligands. Importantly, non-thiolated ssDNA did not produce bands other than that of the AuNPs, suggesting that the ligands on AuNCs effectively reduce interactions between non-thiolated ssDNA and gold. They also eliminated the possibility that these bands were the product of AuNP dimers and trimers using TEM. The conclusion is that each discrete band in the gel represents a product of bioconjugation and cannot be attributed to either AuNPs or ssDNA[14]. A later publication by Ackerson *et al.* performed a similar experiment, this time with AuNCs and PAGE. This group again found that bands represented AuNC bioconjugation products with specific numbers of DNA-ligands[5].

For the LER in Figure 2.1.a., we mixed 18 μM of the M16 oligonucleotides with 180 μM of AuNCs in 200 mM NaCl and vortexed the solution overnight. In Figure 2.1.a. Lane 2, we can see the LER resulted in fAuNCs with 1, 2, and 3 LDNA. fAuNCs with a single LDNA (fAuNC-(LDNA)) appear above the excess ssDNA and fAuNC-($LDNA)_3$ appear near the top of the gel image.

We further characterized the LER products using DLS to measure the hydrodynamic diameter of the fAuNC-LDNA conjugates (Figure 2.1.a.). The LER used to produce the conjugates was a 1:10 TssDNA to AuNC with no additional salt, which previous experiments have shown to produce fAuNCs with a single LDNA. The hydrodynamic diameter of the AuNCs was measured to be 1.6 nm, and the expected length of a 16-mer oligonucleotide would be 3.94±1.41 nm. The hydrodynamic diameter of the conjugates was measured to

be 6.7 nm, which agrees with our predictions given the variability of the ssDNA length in the solution.

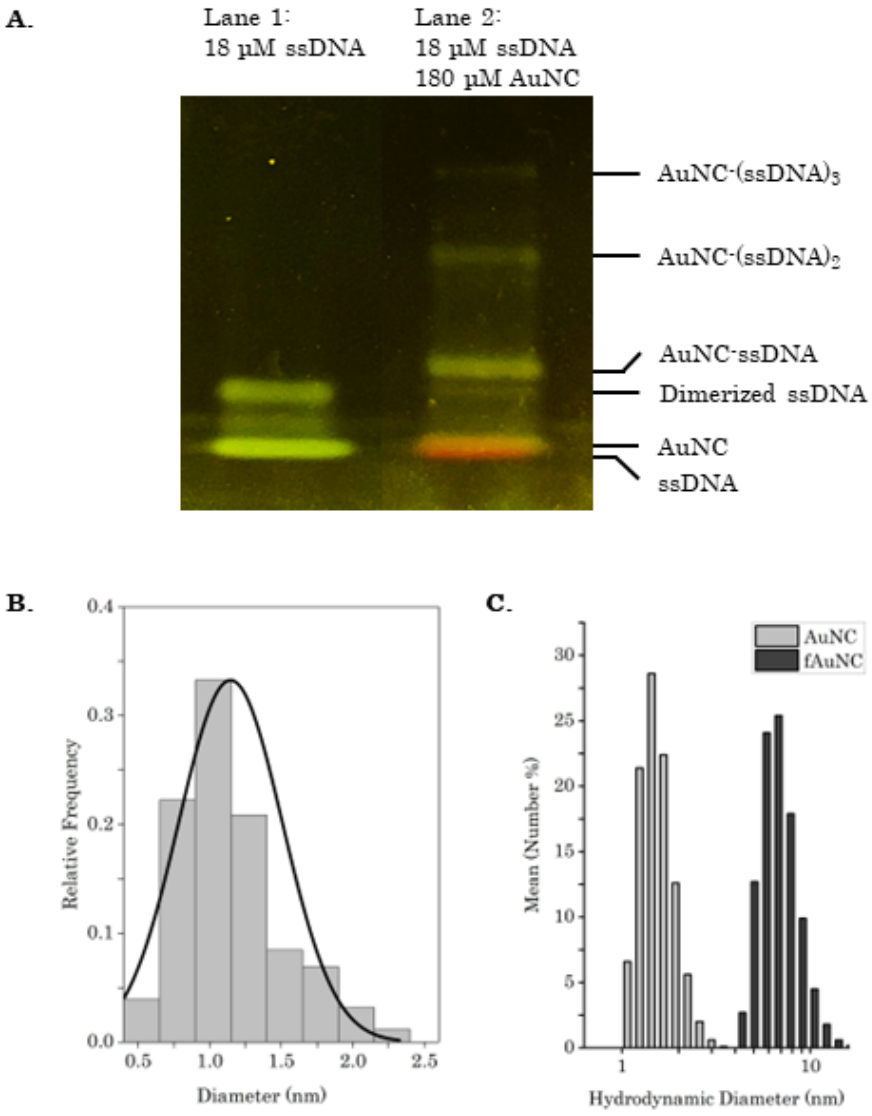

Figure 2.1. Initial characterization of AuNCs and LER. (A) True color photograph of 10%-20% polyacrylamide gel electrophoresis (PAGE) of 16-mer thiolated ssDNA (TssDNA)/AuNC conjugates. Lane 1. 16-mer thiolated ssDNA (TssDNA) Lane 2. Products of 16-mer TssDNA and AuNC ligand exchange in 0.1M NaCl. The appearance of discrete bands indicates the conjugation of a defined number of TssDNA attached to the AuNCs. (B) Histogram of AuNC size.

2.3.2. The distribution of LERs per AuNC is influenced by DNA: AuNC molar ratio, salt, length, and sequence of DNA ligands.

In the following experiments, we sought to determine the effects of salt, DNA: AuNC ratio, and oligonucleotide sequence on fAuNC yields and ligand speciation. We compared the LERs of four oligonucleotide sequences at various salt and AuNC concentrations. We chose sequences that included a 16-mer poly-thiamine sequence and 16-, 29-, and 48-mer thiolated mixed base oligonucleotide sequences, referred to as PolyT, M16, M29, and M48, respectively. The exact sequences are summarized in Table 2.1. The LER conditions evaluated for each sequence were 0-200 mM NaCl solutions with ssDNA to AuNC ratios of 1:2, 1:5, and 1:10. The concentration of DNA in each LER was 5 µM. Early experiments determined that equilibrium for the LER was reached with an hour of mixing, so overnight vertexing of the LER solutions was more than sufficient to reach equilibrium for all sequences. We visualized the DNA gel migration using Sybr Green II excited at 420 nm on a transilluminator. Gel images were recorded as true color photographs.

Gel densitometry is a quantitative measurement technique often used to correlate optical density to biomolecule concentrations[15,16]. We applied this technique to quantify fAuNC: $(LDNA)_n$ concentrations using Image Studio™ Lite software. Syber Green II (SGII) and AuNCs fluoresce when excited at 420 nm. We found that the AuNC signal did not contain any green pixel data, while the SGII had a red-to-green pixel ratio of 1:2. Therefore, we filtered our data only to include "green" pixels to eliminate the pixels corresponding to AuNC. Therefore, the pixel density of each LER band represents the concentration of LDNA. fAuNC-$(LDNA)_n$ concentrations for each discrete band were determined by dividing the total LDNA concentration by the number of LDNAs conjugated to AuNC. Total fAuNC concentration is the sum of all fAuNC-$(LDNA)_n$ concentrations. In Figure 2.2., we have summarized the fAuNC concentrations for each ligand exchange reaction condition.

We found the low yields of PolyT LERs to be the most surprising results. The only PolyT LER to produce visible PAGE results was 200 mM NaCl with a 1:10 ratio, as seen in Figure 2.2.a. This observation contrasts with M16, M29, and M48 LER yields seen in Figures 2.2.b-d. For these LERs, every combination of salt and DNA: AuNC ratios produced significantly higher fAuNC yields.

In Figures 2.2.b-d, we also see a trend of decreasing yield with increasing oligonucleotide length. M16 has some of the highest yields in these figures, while M48 has the lowest. These findings may partly be explained using previous research on the diffusional behavior of oligonucleotides in

solution. A study by Werner used single-stranded ribonucleic acid's (ssRNA's) radius of gyration (R_G) to determine its diffusional velocity. Since R_G increases with the oligonucleotide size, larger oligonucleotides have slower diffusional velocity[17]. A shorter, faster-moving LDNA increases the probability of successful LERs. This justifies the higher fAuNC yield of M16 compared to M48.

The length of M48 makes it sterically more challenging for a LER to occur. These AuNCs are 1.09 ± 0.36 nm, while the contour length of a 48-mer ssDNA would be approximately 32 nm[18]. A 32 nm sequence must align its thiol with a vertex of the 1.09 nm AuNC for a LER to occur. Thus, we can attribute the reduced fAuNC yield associated with longer LDNAs to slower translational diffusion and steric inhibition.

Looking again at Figures 2.2.b-d., we see that salt concentration also affected fAuNC yields. We see the greatest impact of salt concentration at high DNA: AuNC ratios. Figure 2.2.b. shows that M16 fAuNC yield doubles when the LER occurs in a salt solution. Since AuNCs and DNA are anionic, DNA adsorption is affected by the long-range electrostatic repulsion, which is related to the salt-dependent Debye length (λ_D). Only when DNA is sufficiently close to the AuNC can attractive short-range forces take place and enable LERs. Na^+ ions screen the repulsion between DNA and AuNCs. Thus, as Na^+ ions increase, the Debye length decreases, and the probability of successful LERs increases. This effect is the most significant at higher DNA: AuNC ratios, where we see the largest yield increase when comparing the salt-free and 200 mM NaCl conditions. At higher ionic strengths the free energy of self-dimerization decreases[19]. As discussed previously, higher salt concentrations also increase the diffusion coefficients of oligonucleotides and accelerate the collision between DNA and the AuNC[18], thus increasing the number of DNA dimers in solution. As discussed later in this chapter, these DNA dimers, acting as bivalent ligands, increase the thermodynamic probability of successful ligand exchanges.

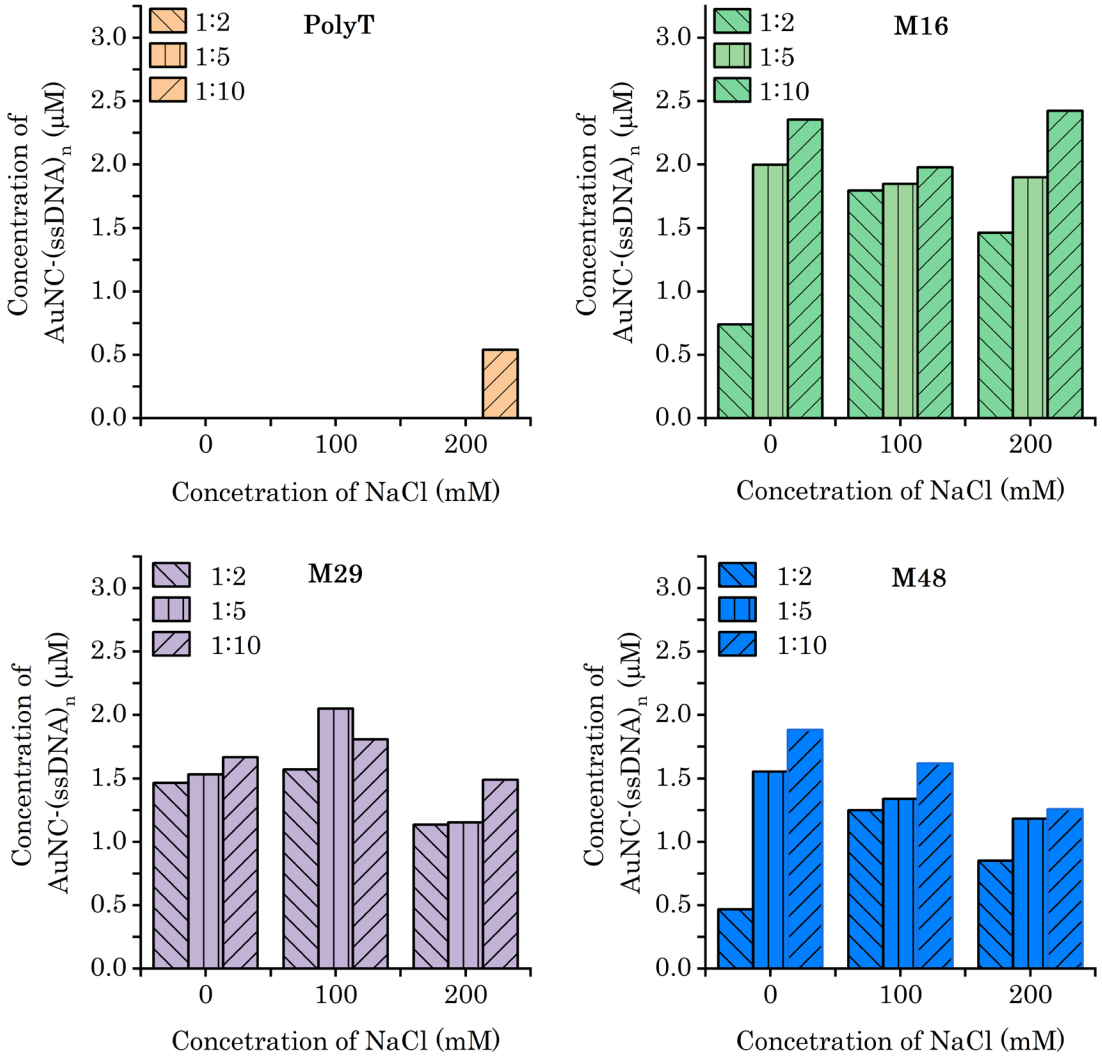

Figure 2.2. Calculated fAuNC yields for each PolyT (A), M16 (B), M29 (C), and M48 (D) under different DNA: AuNC ratios and salt concentrations.

The contrast between PolyT and M16 fAuNC yields warrants further consideration. PolyT and M16 have 16-mer oligonucleotide sequences, yet M16 LERs produced significantly higher yields in every reaction condition. We examined various explanations for the PolyT disparity. PolyT sequences have been used to assemble copolymer micelles[20] and copper nanoclusters[21]. If the PolyT were forming micelles, additional gel bands should have been observed in all gel lanes, including the control lane. Moreover, unlike copper, which has a strong affinity for thymine, thymine has the weakest interactions with gold. Any chemical interactions between thymine and the captopril ligands should have also been seen with all other sequences since they all contain a 5-6 thymine spacer sequence after the thiol. Since the reaction conditions cannot

explain these divergent yields, the remaining variable is oligonucleotide sequences. The PolyT sequence is a 16-mer oligonucleotide composed entirely of thymine bases. M16 has a 6-thymine sequence and a high percentage of cytosine and guanine bases. If we compare these sequences, the most significant difference is that PolyT lacks a base pairing capacity. The implication is that the base pairing plays a significant role in AuNC-DNA LERs. We will examine this further in later sections of this chapter.

2.3.3. LDNA: AuNC

Table 2.2. The average number of DNA ligands per conjugated fAuNC

	Mean LDNA: fAuNC											
DNA Sequence	**PolyT**			**M16**			**M29**			**M48**		
DNA: AuNC	**1:2**	**1:5**	**1:10**	**1:2**	**1:5**	**1:10**	**1:2**	**1:5**	**1:10**	**1:2**	**1:5**	**1:10**
No Salt	0.00	0.00	0.00	1.00	1.26	1.07	1.00	1.28	1.18	1.00	1.31	1.47
100 mM NaCl	0.00	0.00	0.00	1.65	1.41	1.31	2.50	1.41	2.17	1.47	1.24	1.29
200 mM NaCl	0.00	0.00	1.00	2.78	1.98	1.47	3.03	1.53	2.14	1.53	1.64	1.35

While yields are an essential indicator of LERs' success, it is also important to consider the ligand speciation produced by LERs. Ligand speciation is the number of LDNAs per fAuNC (LDNA: fAuNC). The LDNA: fAuNC determines which downstream applications best suits a particular bioconjugate. Bioconjugates in dyad assemblies ideally should be mono-functionalized, *i.e.*, have a LDNA: fAuNC of 1. On the other hand, those destined for network solids would benefit from having greater LDNA: fAuNC. Thus, we thought it important to consider this in our characterization of AuNC-DNA LERs.

For this analysis, we looked exclusively at the AuNC-DNA conjugates to determine the quantity of DNA ligands conjugated to AuNCs for each reaction condition, i.e., AuNCs that did not undergo LERs were not taken into account. We applied a weighted average to the fAuNC-$(LDNA)_n$ concentrations to determine each reaction's average number of LDNA: fAuNC. These are summarized these results in Table 2.2. The overall LDNA: fAuNC average for PolyT, M16, M29, and M48 is 1.00, 1.55, 1.80, and 1.37, respectively.

We again see that PolyT is an outlier with an average of 1.0 LDNA: fAuNC. Again, comparing these results to M16, we see that M16 has a 14× higher LDNA: fAuNC. While the PolyT results are interesting, concluding with limited data is difficult. The intriguing PolyT results in the last two sections should be explored in future studies.

The M48 LDNA: fAuNC is lower than M16 and M29. In data summarized in Table 2, we see that LDNA: fAuNC never averages above 2 with any M48 reaction condition. The size of a M48 ligand could be sterically inhibiting the integration of multiple M48s into the ligand monolayer. Longer oligonucleotide sequences also have higher probabilities of forming secondary structures. Evidence for secondary structure can be found in the gel image in Figure 2.3.a. Lane 1 is the control lane containing only 5 μM M48. A sequence with no secondary interactions would have only a single DNA band. Instead, we observed multiple bands. To determine if there was a thermodynamically favored M48 secondary structure, we used NUPACK[22,23], a thermodynamic design and analysis tool for nucleic acid systems. The NUPACK calculations were performed with the following parameters: 25 °C, 100 and 200 mM NaCl, allowed complex size of 4, and dangles set to "all." The NUPACK predicted secondary structure is seen in Figure 2.3.b. Therefore, the formation of secondary structures may increase the footprint of the ligand, inhibiting additional LERs on the same AuNC, which is only ~1 nm in diameter.

We next compared the dimerization probabilities of M29 and M16, as seen in Figure 2.4. M29 had free energies of -2.19 kcal/mol and -2.40 kcal/mol for 100 mM NaCl and 200 mM NaCl, respectively, suggesting that M29 would spontaneously self-dimerize under these conditions. In the 200 mM solution with 5 μM of M29, one would expect 0.12 μM to be dimers. In contrast, the calculated free energies for M16 in solution were 0.00 kcal/mol at 100 mM NaCl and -0.20 kcal/mol at 200 mM NaCl, suggesting that M16 sequences are at or near equilibrium and not dimerized under these conditions. We had initially designed these oligonucleotides as capture sequences for self-assembly experiments. As such, we designed them specifically to limit dimerization and secondary structures.

To assess whether M16 and M29 LERs were occurring as independent events, we compared the experimentally determined LDNA: AuNC distributions to Poisson distributions that describe discrete, independent LERs. We calculated the Poisson distributions using Equation 2.1, where λ is the mean LDNA: AuNC and x are 8, the highest number of LDNA: AuNC observed.

$$P(x) = \frac{\lambda^x e^{-\lambda}}{x!} \tag{2.1}$$

Figures 2.5 and 2.6 show that both M16 and M29 deviate from the predicted Poisson distributions. The deviation is greatest at the lowest salt concentrations, where the experimental results produce more AuNCs with a single LDNA than would be predicted if these LERs were behaving independently and randomly. The deviation suggests that electrostatic repulsion between these DNA ligands favors the incorporation of single ligands as opposed to multiple ligands. This finding offers a means of tailoring the number of ligands for various applications. *E.g.*, those that require mono-functionalized fAuNCs can carry out LERs at lower salt concentrations, and those that require multiple ligands can use higher salt conditions.

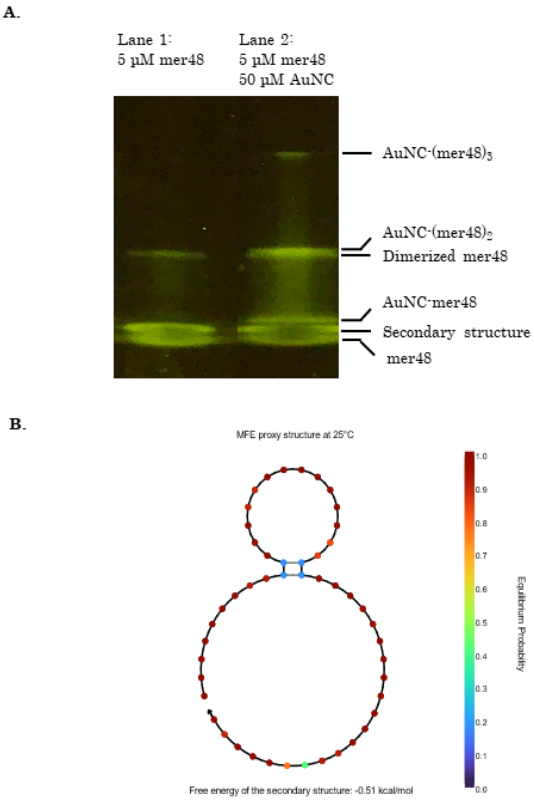

Figure 2.3. PAGE and secondary structure of M48. (A) PAGE of 5 uM M48 and 40 uM AuNC. The secondary structure can be seen as two bands above the M48 band. (B) Most likely secondary structure for M48, as predicted by NUPACK

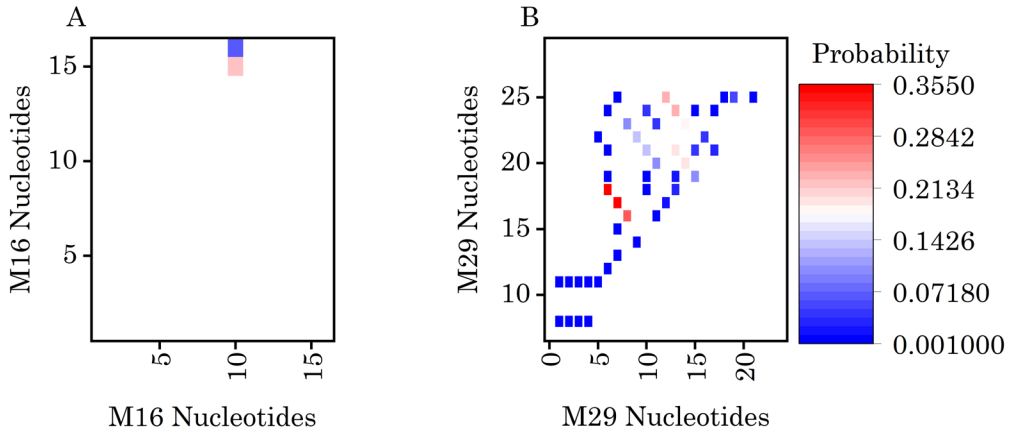

Figure 2.4. NUPACK self-dimerization probabilities at 25 °C in 200 mM NaCl for M16 (A) and M29 (B)

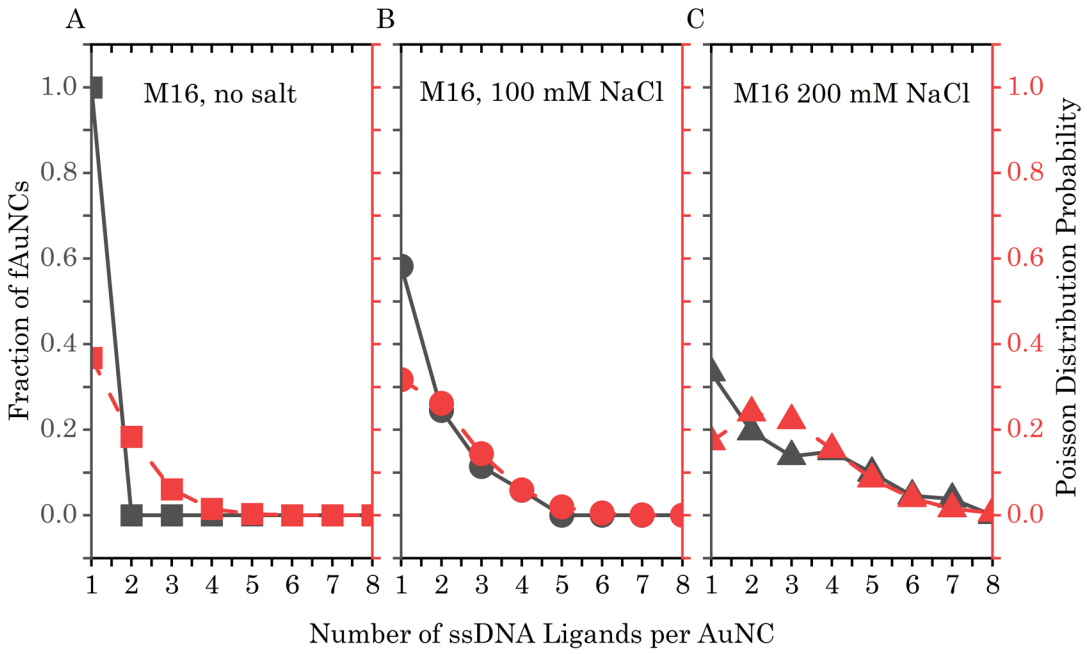

Figure 2.5. Comparison of M16 experimental LDNA: AuNC (black, solid line) and predicted Poisson distribution (red, dashed line). All data is for 5 µM M16: 10 µM AuNC.

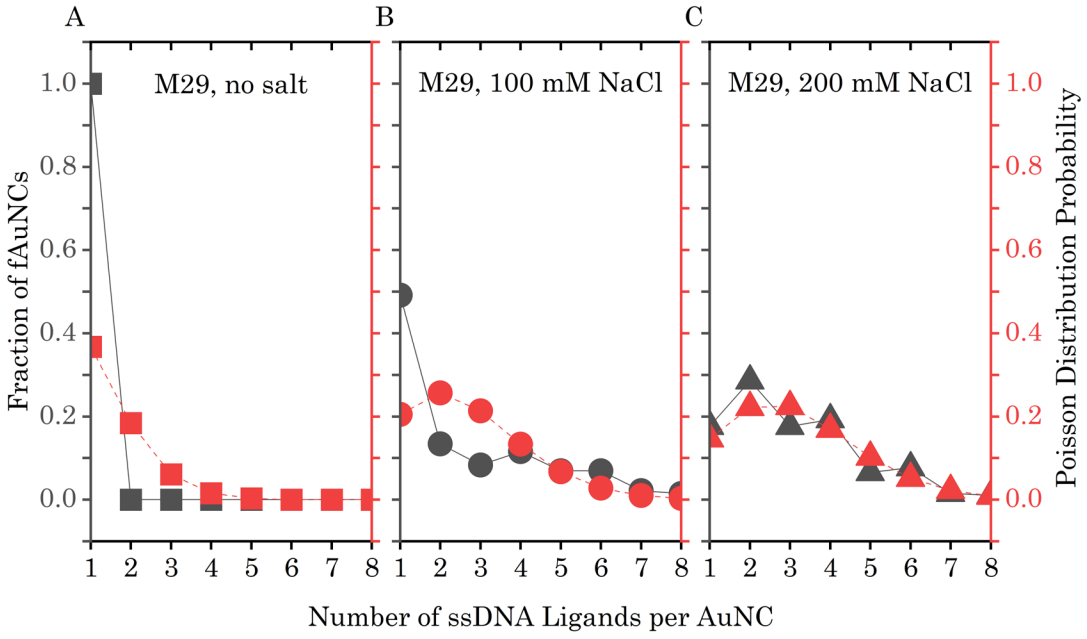

Figure 2.6. Comparison of M29 experimental LDNA: AuNC (black, solid line) and predicted Poisson distribution (red, dashed line). All data is for 5 µM M29: 10 µM AuNC.

2.3.4. Cooperative, Independent, and Negative Cooperativity Binding Models of Oligonucleotide LER with AuNCs

The above results indicate a relationship between oligonucleotide sequence and length with both the fAuNC yields and LDNA: AuNC. The deviance of LDNA: AuNC from the Poisson distribution suggests that these LER are not independent or random. We applied the Hill equation further to parse the thermodynamics of the oligomer LERs. The Hill equation is a mathematical model that illustrates the binding relationship between biological molecules and multiple ligands, such as the cooperative binding of oxygen molecules and hemoglobin. For cooperative binding to occur, a substrate must have multiple binding sites available, and the binding of one ligand must alter the affinity for the following binding event[24–26]. When hemoglobin binds to an O_2 molecule, it undergoes a conformational change, increasing the probability of binding to the next O_2. Other studies have also utilized the Hill equation to demonstrate the cooperative binding of proteins on nanoparticles[27,28].

The Hill coefficient (α_H) is the term that describes the extent of cooperativity in this binding and is summarized below:

$$\alpha_H > 1 \; cooperative \; binding$$

$$\alpha_H = 1 \; independent \; binding$$

$$\alpha_H < 1 \; negative \; coopertivity$$

Then the equilibrium disassociation constant (K_D) that describes the extent that the DNA-ligand disassociates from the AuNCs would be:

$$K_D = \frac{n[ssDNA]^n \left[Au_{25}(Captopril)_{18}\right]}{\left[Au_{25}(Captopril)_{18-n}(ssDNA)_n\right]} \tag{2.2}$$

The fractional saturation (ν) describes how much of the DNA is bound to the AuNCs in relationship to the total concentration of AuNC, and the binding site saturation is described by θ:

$$\nu = \frac{[ssDNA]_b}{[AuNC]_t} \tag{2.3}$$

$$\theta = \frac{\nu}{n} \tag{2.4}$$

Since PAGE bands showed no more than 8 DNA-ligands attached to AuNCs, we assumed *n* to be 8 for our calculations. Therefore, we calculated the free DNA as the excess DNA band.

$$\theta = \frac{DNA_{free}^{\alpha_H}}{K^{\alpha_H} + DNA_{free}^{\alpha_H}} \quad (2.5)$$

$$\frac{\theta}{1-\theta} = \frac{DNA_{free}^{\alpha_H}}{K_A^{\alpha_H}} = \frac{DNA_{free}^{\alpha_H}}{K_D} \quad (2.6)$$

Which then gives us the linear form below:

$$\log\left(\frac{\theta}{1-\theta}\right) = \alpha_H \log DNA_{free} - \log K_D \quad (2.7)$$

We have summarized the results from these calculations in Figure 2.8 and Table 2.3. The results from the M48 DNA experiments were inconclusive. The steric hindrance from the DNA ligand surrounding the AuNC makes it unsuitable for this model. The M16 ligand has a clear linear relationship and a Hill coefficient of 1.00, indicating that monomeric binding did not change the affinity for subsequent ligands. The M29 ligand has Hill coefficients between 3.23 and 33.73 for the different salt conditions, indicating that these ligands exhibit cooperative binding. For the M29, we suspect that the dimerized ligands act as cooperative bivalent ligands. In a bivalent ligand system, the second ligand is spatially restricted and near the binding site after the binding of first ligand to the substrate. As such, rotational and translational entropy is lost for the second LER, making the conditions more favorable. Kinetically, the forced proximity of the second ligand acts as an increased localized concentration surrounding the substrate and will therefore increase the binding rate.

Table 2.3. Calculated Hill Coefficients for M16 and M29

DNA	[NaCl]	K_D	α_H	R
M16	No Salt	0.125	1.00	1.00
	100 mM	0.125	1.00	1.00
	200 mM	0.125	1.00	1.00
M29	No Salt	$1.430\ 10^{-16}$	3.23±0.38	0.9729
	100 mM	$4.57\ 10^{-25}$	4.43±0.43	0.9811
	200 mM	0	33.73±1.99	0.9930

We have illustrated our proposed mechanism in Figure 2.7. We propose that the first bound ligand of the DNA dimer acts as a tether restricting the

second ligand's degrees of freedom. Thus, it pays the entropic cost for the second ligand, making the second LER more probable. Once both ligands have been conjugated to the AuNC, they can separate and dimerize with free ligands in the solution, making each subsequent LER they participate in more thermodynamically favorable.

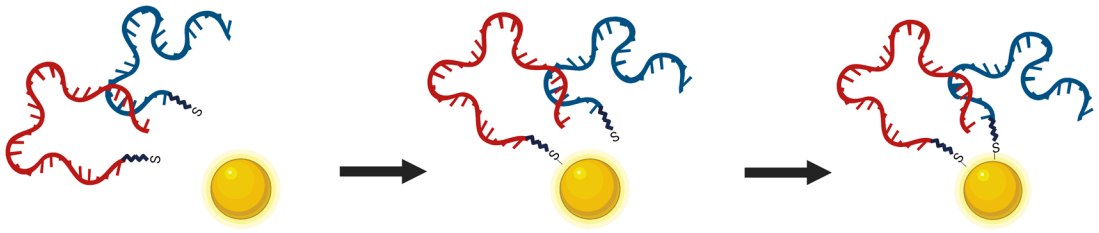

Figure 2.7. Schematic of proposed ligand exchange pathway exhibiting cooperative binding.

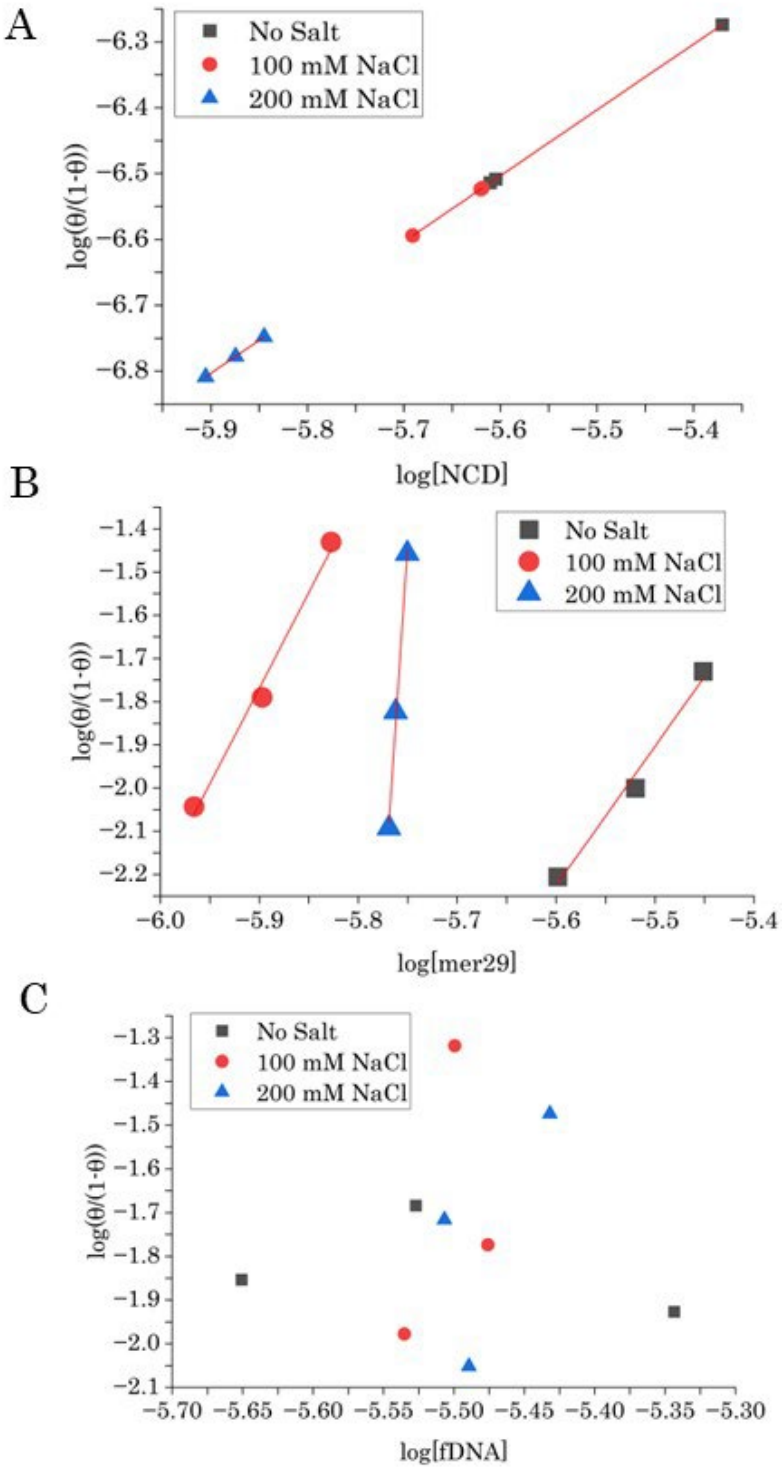

Figure 2.8. Hill equation results for (A) M16, (B) M29, and (C) M48.

2.4. Conclusion and Outlook

In summary, we have found that both AuNC and salt concentrations affect ligand exchange products and that the noncovalent interactions of DNA are a nontrivial and complex variable in these LERs. By better understanding how these variables affect ligand exchanges, it is possible to design targeted experiments that will produce either mono- or multi-conjugated AuNCs. While there is a cross-over from previous small-molecule thiolate ligand exchange studies, we have illustrated here that the complexity of the biomolecule conjugations warrants independent investigation. The final conjugation products of such reactions are affected by both the length and sequence of the DNA ligands. The complexity of noncovalent DNA interactions and their effect on final products is not inconsequential. The thermodynamics of dimerization and secondary structures should be modeled before undertaking these conjugations to predict products better.

While these experiments provide insight into the DNA LERs of AuNCs, there are limitations to our findings. First, this set of experiments is a quantitative analysis of a qualitative technique. Capillary electrolysis coupled with a diode array or mass spectrometry technique would provide significantly more information and could be applied to kinetics studies. The second is that densitometric analysis will underestimate the concentrations of intense bands if they saturate the pixels.

Poly-thiamine sequences and poly sequences of other nucleotides are regularly used as control sequences when studying LERs. As we have seen in these experiments, PolyT sequences had significantly different behavior from mixed nucleotide sequences in these reactions. There should be follow-up experiments exploring other poly-nucleotide oligomers under more varied conditions than those available for PAGE analysis.

There has yet to be a study of the effect of self-dimerizing DNA sequences on LERs that have not been applied to AuNPs and 2D gold surfaces. Much of this is due to the difficulty of quantifying each ligand coverage. The small size of AuNCs makes studying this process more amenable to various techniques. Atomically precise AuNCs represent a well-organized microcosm of gold-thiol-DNA interactions that eliminates many unknowns in larger systems. Further study of these mechanisms could provide profound insight into AuNPs and 2D surfaces, allowing for more efficient and effective designs.

2.5. References

1. Wu Z, Jin R. On the ligand's role in the fluorescence of gold nanoclusters. *Nano Lett*. 2010;10(7):2568-2573. doi:10.1021/nl101225f

2. Dillenback LM, Goodrich GP, Keating CD. Temperature-programmed assembly of DNA:Au nanoparticle bioconjugates. *Nano Lett*. 2006;6(1):16-23. doi:10.1021/NL0508873

3. Rinker S, Ke Y, Liu Y, Chhabra R, Yan H. Self-assembled DNA nanostructures for distance-dependent multivalent ligand–protein binding. *Nature Nanotech*. 2008;3(7):418-422. doi:10.1038/nnano.2008.164

4. Jhaveri SD, Foos EE, Lowy DA, Chang EL, Snow AW, Ancona MG. Isolation and Characterization of Trioxyethylene-Encapsulated Gold Nanoclusters Functionalized with a Single DNA Strand. *Nano Lett*. 2004;4(4):737-740. doi:10.1021/nl0499591

5. Ackerson CJ, Sykes MT, Kornberg RD. Defined DNA/nanoparticle conjugates. *Proc Natl Acad Sci U S A*. 2005;102(38):13383-13385. doi:10.1073/PNAS.0506290102

6. Storhoff JJ, Elghanian R, Mirkin CA, Letsinger RL. Sequence-dependent stability of DNA-modified gold nanoparticles. *Langmuir*. 2002;18(17):6666-6670. doi:10.1021/LA0202428

7. Li Z, Cheng E, Huang W, et al. Improving the yield of mono-DNA-functionalized gold nanoparticles through dual steric hindrance. *J Am Chem Soc*. 2011;133(39):15284-15287. doi:10.1021/JA205712A/SUPPL_FILE/JA205712A_SI_001.PDF

8. Liu B, Liu J. Methods for preparing DNA-functionalized gold nanoparticles, a key reagent of bioanalytical chemistry. *Analytical Methods*. 2017;9(18):2633-2643. doi:10.1039/C7AY00368D

9. Li F, Zhang H, Dever B, Li XF, Chris Le X. Thermal Stability of DNA Functionalized Gold Nanoparticles. *Bioconjug Chem*. 2013;24(11):1790-1797. doi:10.1021/bc300687z

10. Bhatt N, Huang PJJ, Dave N, Liu J. Dissociation and degradation of thiol-modified DNA on gold nanoparticles in aqueous and organic solvents. *Langmuir*. 2011;27(10):6132-6137. doi:10.1021/la200241d

11. Kumar S, Jin R. Water-soluble Au25(Capt)18 nanoclusters: synthesis, thermal stability, and optical properties. *Nanoscale*. 2012;4(14):4222-4227. doi:10.1039/c2nr30833a

12. Kumar S, Jin R. Water-Soluble Au 25 (Capt) 18 Nanoclusters: Synthesis, Thermal Stability, and Optical Properties. Accessed August 8, 2017. http://www.rsc.org/suppdata/nr/c2/c2nr30833a/c2nr30833a.pdf

13. Abràmoff MD, Magalhães PJ, Ram SJ. Image processing with imageJ. *Biophotonics International*. 2004;11(7). doi:10.1201/9781420005615.ax4

14. Zanchet D, Micheel CM, Parak WJ, Gerion D, Alivisatos AP. Electrophoretic Isolation of Discrete Au Nanocrystal/DNA Conjugates. *Nano Lett*. 2001;1(1):32-35. doi:10.1021/NL005508E

15. Pillai-Kastoori L, Schutz-Geschwender AR, Harford JA. A systematic approach to quantitative Western blot analysis. *Anal Biochem*. 2020;593. doi:10.1016/j.ab.2020.113608

16. Blanche PJ, Gong EL, Forte TM, Nichols A V. Characterization of human high-density lipoproteins by gradient gel electrophoresis. *Biochimica et Biophysica Acta (BBA)/Lipids and Lipid Metabolism*. 1981;665(3). doi:10.1016/0005-2760(81)90253-8

17. Werner A. Predicting translational diffusion of evolutionary conserved RNA structures by the nucleotide number. *Nucleic Acids Res*. 2011;39(3). doi:10.1093/nar/gkq808

18. Roth E, Glick Azaria A, Girshevitz O, Bitler A, Garini Y. Measuring the Conformation and Persistence Length of Single-Stranded DNA Using a DNA Origami Structure. *Nano Lett*. 2018;18(11):6703-6709. doi:10.1021/ACS.NANOLETT.8B02093

19. Huguet JM, Bizarro C V., Forns N, Smith SB, Bustamante C, Ritort F. Single-molecule derivation of salt dependent base-pair free energies in DNA. *Proc Natl Acad Sci U S A*. 2010;107(35). doi:10.1073/pnas.1001454107

20. Rizzuto FJ, Dore MD, Rafique MG, Luo X, Sleiman HF. DNA Sequence and Length Dictate the Assembly of Nucleic Acid Block Copolymers. *J Am Chem Soc*. 2022;144(27). doi:10.1021/jacs.2c03506

21. Qing Z, He X, Qing T, et al. Poly(thymine)-templated fluorescent copper nanoparticles for ultrasensitive label-free nuclease assay and its inhibitors screening. *Anal Chem*. 2013;85(24). doi:10.1021/ac403354c

22. Zadeh JN, Steenberg CD, Bois JS, et al. NUPACK: Analysis and design of nucleic acid systems. *J Comput Chem*. 2011;32(1). doi:10.1002/jcc.21596

23. E. Fornace M, J. Porubsky N, A. Pierce N. A Unified Dynamic Programming Framework for the Analysis of Interacting Nucleic Acid Strands: Enhanced Models, Scalability, and Speed. *ACS Synth Biol*. 2020;9(10):2665-2678. doi:10.1021/acssynbio.9b00523

24. Lavrinenko IA, Vashanov GA, Cáceres JLH, Nechipurenko YD. Fitting Parameters of a Modified Hill’s Equation and Their Influence on the Shape of the Model Hemoglobin Oxygenation Curve. *Oxygen 2023, Vol 3, Pages 90-101*. 2023;3(1):90-101. doi:10.3390/OXYGEN3010007

25. Sousa AA. A Note on the use of Steady-State Fluorescence Quenching to Quantify Nanoparticle-Protein Interactions. *J Fluoresc*. 2015;25(6):1567-1575. doi:10.1007/S10895-015-1665-3/FIGURES/4

26. Somvanshi PR, Venkatesh K V. Hill Equation. *Encyclopedia of Systems Biology*. Published online 2013:892-895. doi:10.1007/978-1-4419-9863-7_946

27. Li N, Zeng S, He L, Zhong W. Probing Nanoparticle−Protein Interaction by Capillary Electrophoresis. *Anal Chem*. 2010;82(17):7460-7466. doi:10.1021/ac101627p

28. Mishra A, Das PK. Thermodynamics of multilayer protein adsorption on a gold nanoparticle surface. *Physical Chemistry Chemical Physics*. 2022;24(37). doi:10.1039/d2cp02439j

2.6. Appendix

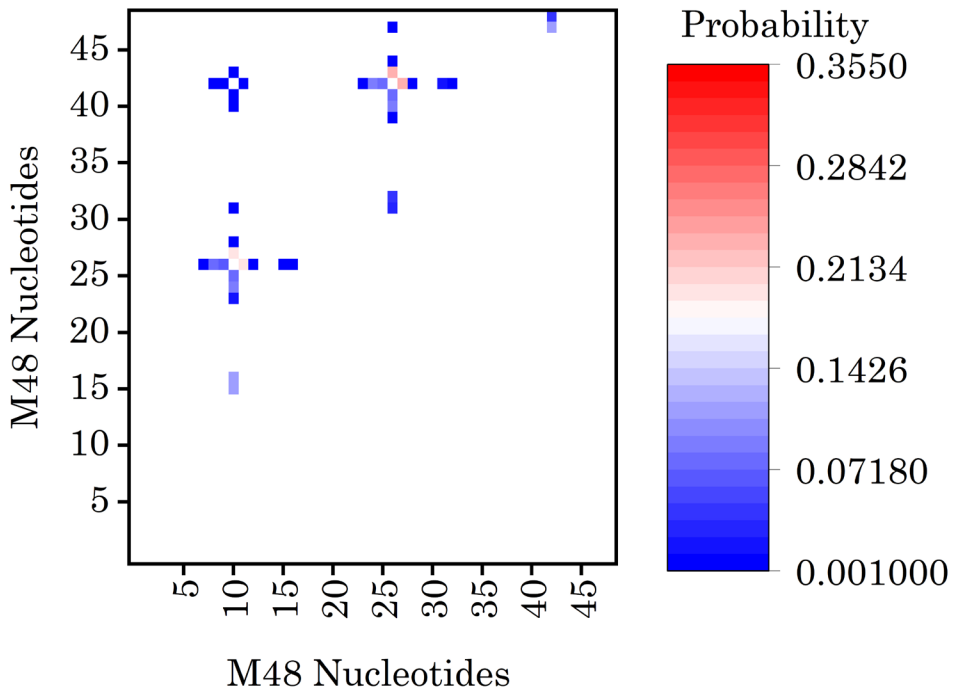

Appendix 2.1. NUPACK self-dimerization probabilities for M48 at 25 °C in 200 mM NaCl.

Chapter 3

Isolation of Oligonucleotide-Gold Nanocluster Conjugates for Self-Assembly Applications

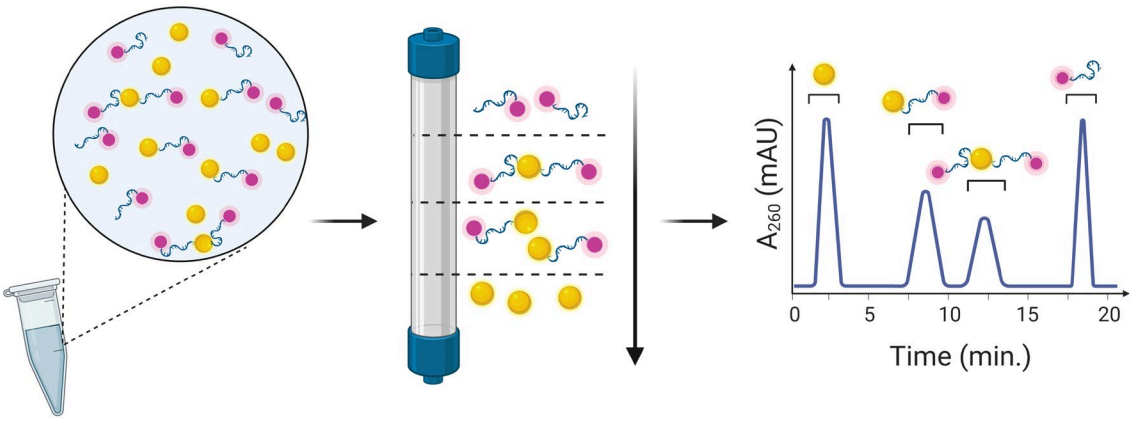

Figure 3.1. Schematic of bioconjugated gold nanocluster (fAuNC) purification. A mixture of gold nanoclusters (AuNCs) and Cy5-modified oligonucleotides is vortexed overnight in a salt solution. The final solution contains excess reactants as well as mono- and di-fAuNCs. An ion-paired reversed-phased method can separate fAuNCs from the excess reactants by the number of oligonucleotides attached to the AuNCs. Fractions of the fAuNCs were collected and concentrated.

3.1. Introduction

Many emerging nanomedicine applications require the conjugation of biomolecules to interface AuNCs within biological systems or aid in self-assembly. The success of LERs in conjugating DNA to AuNCs is an important first step to incorporating them into bioimaging [1–3], sensing, and diagnostic therapies[4–6]. As discussed earlier, the ligand monolayer significantly contributes to the physiochemical properties of AuNCs[7–10] and their ability to interface with biological systems. Thus, it is important to characterize these bioconjugates' self-assembly and targeting abilities and their unintended effects on a biological system if they are to be used *in vivo* nanomedicine applications. A recent study that changed the ligand monolayer from a single residue to a di-peptide observed a 22× decrease in liver-to-blood ratios[11]. A second study comparing AuNC protein and peptide conjugates found that at 28 days, only 5% of the protein conjugates had renal clearance vs. 94% of the peptide conjugates. Researchers concluded that the protein's size and propensity to form toxic aggregates inhibited kidney uptake[12]. From such examples, we see that the biomolecule composition of the AuNC ligand monolayer significantly impacts biodistribution, tumor uptake, and biodegradability. For *in vivo* applications to advance, it is essential to develop scalable purification techniques to isolate and quantify AuNC bioconjugates based on the number and type of conjugated biomolecules. For AuNC-DNA

conjugates, a purification technique must isolate AuNC-$(DNA)_n$ from AuNC-$(DNA)_{n\pm1}$.

While GE is the most common method for isolating the AuNC-DNA bioconjugates by the number of DNA ligands is gel electrophoresis (GE)[13–16], HPLC methods offer superior resolution, scalability, and purity. IP-RP HPLC methods have been used to separate both AuNCs and oligonucleotides. IP-RP HPLC methods compatible with water-soluble ligands have thus far focused on AuNC size separations[17,18]. Niihori et al. achieved a high-resolution separation of Au_n(Glutathionate)$_n$ clusters using an IP-RP method[18]. There is a much more extensive body of research using IP-RP methods for oligonucleotide separations. These methods have purified oligonucleotides by their length, type, and presence of chemical modifications [19–26]. IP-RP methods' success in purifying both AuNCs and DNA indicates that it could be a successful method for separating AuNC-$(DNA)_n$ from AuNC-$(DNA)_{n\pm1}$. Thus far, there has been no publication using this method to purify such AuNC-DNA conjugates.

In this chapter, we investigate IP-RP HPLC as a method for isolating AuNC-$(DNA)_n$ from AuNC-$(DNA)_{n\pm1}$. An Au_{25}(Captopril)$_{18}$ was chosen for these experiments due to its water-solubility and robustness[27–29]. The AuNCs were conjugated to thiolated ssDNA via a LER with the captopril ligands, resulting in (Au_{25}(Captopril)$_{18-n}$(ssDNA)$_n$). We determined that by utilizing TEAA as our IPR and employing a shallow gradient increase in acetonitrile, it is possible to purify AuNC-DNA conjugates by the extent of their bio-ligand coverage. To demonstrate that these conjugates would be suitable for self-assembly applications, we conjugated AuNCs to Cyanine5 (Cy5) functionalized oligonucleotides. Since AuNCs have a distance-dependent ability to act as quenchers to fluorescent dyes, we used steady-state fluorescence spectroscopic studies to characterize the AuNC-Cy5 conjugates. The spectroscopic results demonstrated that our IP-RP HPLC method has successfully isolated the mono- and di-conjugates.

3.2. Methods and materials

3.2.1. DNA preparation

Table 3.1. Summary of DNA sequences used in experiments.

Description	Name Length	DNA Sequence and Modifications
	NCD	5' – thiol – C6 – TTTT TTGG GCGG TTGG – 3'

Thiolated ssDNA with C6 tether	16 mer	
Cy5 & Thiol Modified ssDNA	**Cy5-NCD**	5' – Cy5 – GTAG TCGC AGAT TATT TT – C3 – thiol – 3'
	18 mer	
Compliment to Cy5 – NCD	**cDNA**	5' – AAAA TAAT CTGC GACT AC – 3'
	18 mer	
NCD with C11 tether	**C11NCD**	5' – thiol – C11 – TTTT TTGG GCGG TTGG – 3'
	16 mer	
Unmodified DNA	**UMD**	5'– CCAA TACT CCTG ACTA – 3'
	16 mer	

NCD, Cy5-NCD, cDNA, and UMD oligonucleotide sequences were purchased from Integrated DNA Technologies (Coralville, IA). The sample arrived lyophilized in disulfide form and was then reconstituted to 200 µM with ultrapure water from the Barnstead Nanopure system (Thermo Fisher Scientific, Houston, TX, US). In addition, we purchased C11NCD from LGC Biosearch Technologies (Petaluma. CA). The DNA sequences used in these experiments are summarized in Table 3.1.

We reduced the disulfide form to the thiol form needed for the AuNC ligand exchange by mixing the TssDNA with Tris (2 carboxyethyl) phosphine hydrochloride (TCEP) (Thermo Fisher) in a 200 µL PCR tube in a 1000:1 TCEP to DNA ratio. The PCR tube was backfilled with nitrogen gas and vortexed for 30 minutes. The reduced TssDNA was purified using a 3 kDa molecular cutoff filter (Sigma Millipore, St. Louis, MO, US). The TCEP/TssDNA solution was added to the filter, filled to 450 µL, and spun for 30 minutes at 14,000×g. We repeated these steps three times. For the final solvent exchange, 250 µL was added and spun for 5 minutes at 14,000×g. After the last spin, the filter was inverted and centrifuged at 10,000×g for 5 minutes. Multiple solvent exchange steps are necessary to remove any remaining TCEP; otherwise, it will degrade the AuNC in the ligand exchange step. The final TssDNA concentration was determined using a NanoDrop™ ND-1000 spectrophotometer (Thermo Fisher Scientific).

3.2.2. Gold nanocluster synthesis

$Au_{25}(Captopril)_{18}$ samples were obtained through a collaboration with the Jin research group and characterized in a previous publication[30]. $HAuCl_4 \cdot 3H_2O$ (78.7 mg) and TOABr (126.8 mg) were stirred vigorously in 10

mL of methanol. After 20 minutes, 5 mL of methanol containing 217.2 mg of captopril was injected into the solution. After 30 minutes, 2 mmol of $NaBH_4$ was added, and the solution was mixed for an additional 8 hours. The mixture was then centrifuged, and the AuNCs were precipitated with a methanol extraction.

3.2.3. Preparation of DNA-conjugated gold nanoclusters

First, ultrapure water was added to PAGE purified and desiccated AuNCs. The AuNC solution concentration was determined using Nanodrop and ε_{310} for AuNCs, 3.6 $\times 10^4$ M^{-1} cm^{-1}. Next, 50 µL ligand exchange solutions were made with TssDNA, AuNCs, and 0.1 M NaCl in a 200 µL PCR tube. The PCR tube was then backfilled with nitrogen gas and vortexed overnight. The final concentrations of solutions used for HPLC analysis were 10 µM TssDNA, 50 µM AuNC and 0.1M NaCl. The final concentrations of solutions for HPLC purification were 18 µM Cy5-ON, 90 µM AuNC, and 0.1 M NaCl.

3.2.4. High-performance liquid chromatography

High-performance liquid chromatography (HPLC) experiments were carried out on an Agilent 1100 series HPLC with an in-line degasser, autosampler, heated column compartment, and diode array detector (DAD). fAuNCs were separated using an ion-paired reverse-phase (IP-RP) method using an AdvanceBio Oligonucleotide C18 4.6 x 150 mm column.

TEA-HFIP mobile phase preparation: 4 mM TEA-100 mM HFIP ion-pairing buffer prepared by mixing 2.60 mL of HPLC grade HFIP (Thermo Fisher) and 0.15 mL HPLC grade TEA (Thermo Fisher) to 100 mL of ultrapure H_2O in a 250 mL volumetric flask. Water was then added to the 250 mL mark on the flask. The pH was then adjusted to 7 ± 0.05. HPLC grade methanol (Thermo Fisher) was used as mobile phase B.

TEAA mobile phase preparation: The 75 mM triethyl ammonium acetate (TEAA) ion-pairing buffer was prepared by mixing 2.61 mL HPLC grade TEA (Thermo Fisher) and 1.05 mL HPLC grade glacial acetic acid (Thermo Fisher) to 100 mL of ultrapure H_2O in a 250 mL volumetric flask. Water was then added to the 250 mL mark on the flask. The pH was then adjusted to 7.00 ± 0.05. HPLC grade acetonitrile (Thermo Fisher) was used as mobile phase B.

HPLC-DAD analysis was performed by monitoring two wavelengths; 260 nm to indicate the presence of DNA and 370 nm to indicate the presence of AuNCs. In addition, absorption spectra for peaks of interest were collected between 225-550 nm.

3.2.5. Liquid chromatography peak analysis

Chromatographic analysis was performed using OpenChrom® (Lablicate GmbH, Hamburg, Germany) and Origin (OriginLab Corporation, Northhampton, Massachusetts).

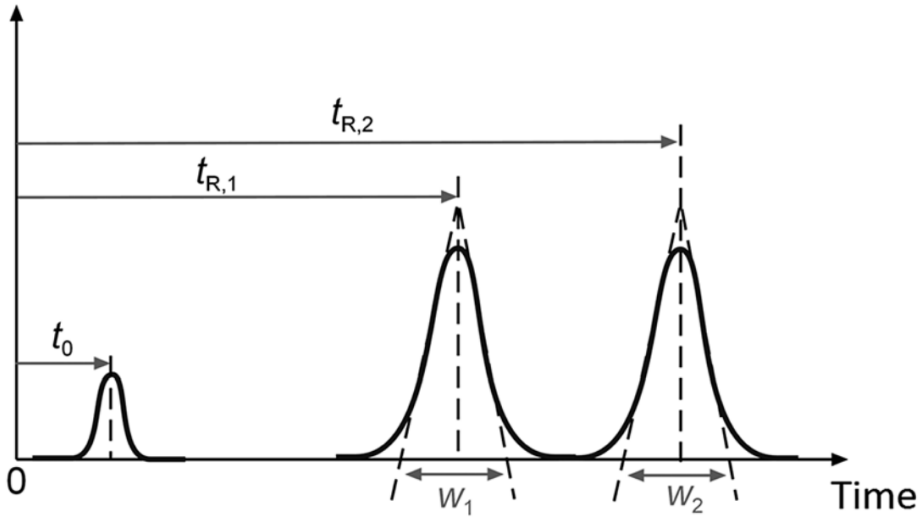

Figure 3.2. Schematic representation of an analytical chromatogram for a binary sample mixture where retention time (t_R) and peak widths at the base (w_b) are given in units of time[31].

Peak resolution (R_s) was calculated according to *Equation 3.1*:

$$R_s = 2\left(\frac{t_{R_2} - t_{R_1}}{w_{b1} + w_{b2}}\right) \qquad (3.1)$$

where retention time (t_R) and peak widths at the base (w_b) are given in units of time. An R_s value >1.5 indicates the baseline resolution of adjacent peaks. R_s fails to describe resolution when baseline resolution is not achieved, and peaks widths cannot be determined. In these cases, *Equation 3.2* was used:

$$d_0 = \frac{(h_p - h_v)}{h_p} \qquad (3.2)$$

where h_p is the height of the smaller peak, and h_v is the height of the valley between the two peaks. The discrimination factor (d_0) value varies between 0, indicating that peaks are coeluting, and 1, indicating the peaks are fully resolved.

3.2.6. oxDNA course-grained modeling

Structural analysis of the fluorescent dye functionalized oligonucleotides, ON-Cy5, was achieved using the course-grained MD simulation program oxDNA[32–35]. Initial ssDNA and dsDNA probe sequences were generated using oxView. After the initial probe sequences were rendered, the molecular behavior was simulated by sequence-dependent virtual move Monte Carlo (VMMC) simulation conditions. Salt conditions were set to 0.5 M NaCl, and the temperature was set to 20 °C. Default values were used for all additional settings. The end-to-end distance of the DNA sequences was measured and recorded for 310 configurations. The obtained data were used to construct distance histograms.

3.2.7. Nanometal surface energy transfer (NSET)

In NSET, a non-radiative transfer of energy from an oscillating dipole to a noble metal surface. The critical distance (d_0) is the separation distance at which the energy transfer efficiency equals 50%. It can be calculated from *Equation 1.5.* , For our calculations ω_F is the Fermi frequency of the metal ($1.2 \times 10^8 cm^{-1}$) and k_F is the Fermi wave vector of the metal ($8.4 \times 10^{15} s^{-1}$) [36–38]. Therefore, the theoretical quenching efficiency between a single donor and acceptor is expressed in *Equation 3.3.*

$$Q_{Eff}(d) = \frac{1}{1+\left(\frac{d}{d_0}\right)^4} \tag{3.3}$$

3.2.8. Fluorescence resonance energy transfer (FRET)

FRET is a non-radiative transfer of energy due to a dipole-dipole interaction. The critical radius (R_0) is the separation distance at which the energy transfer efficiency equals 50%. It can be calculated from *Equation 1.3.* For our calculations $J(\lambda) = 15.69 \times 10^{15}\ cm^3\ M^{-1}$, $\varepsilon_A = 2.5 \times 10^5\ cm^{-1}\ M^{-1}$, η=1.33 and κ=0.667.

3.2.9. Fluorescence measurements of probe quenching

After purification, half the AuNC-Cy5-NCD and AuNC-(Cy5-NCD)$_2$ fractions were diluted to a DNA concentration of 1 nM. The remaining aliquots and an unconjugated Cy5-NCD control probe were annealed to their complementary sequence in a 5:1 cDNA to Cy5-NCD ratio at 25 °C for 3 hours. All samples were backfilled with N_2 and stored at 4 °C.

Steady-state fluorescence measurements were taken with a Horiba Jobin-Yvon Fluorolog with a Xenon lamp excitation source and Horiba

Microsense cuvette. Excitation and emission band passes were set to 5 nm, and the integration time was 30 seconds. 8 µL of annealed fAuNC solutions or control tile solutions were excited at 590 nm. Relative quenching measurements were taken of both ssDNA and ssDNA fAuNC-ON-Cy5 conjugates. Experimental quenching efficiency of the monoconjugate was calculated using *Equation 3.4*[39],

$$E_{1d} = 1 - \frac{I_Q}{I} \tag{3.4}$$

Where I is the fluorescent intensity of the unquenching dye and I_Q is the quenched fluorescent intensity of the dye in the presence of AuNCs. The quenching efficiency for the two donor, single acceptor system of bi-conjugate was calculated using the Gennis-Cantor formula[40]. In a two donor system there is an enhancement effect due to multiple pathways available for the excitement energy to reach the AuNCs. For the bi-conjugate there is NSET between $Cy5_1$ to AuNC, E_1, $Cy5_2$ to AuNC, E_2. If there is enough proximity between the two Cy5 dyes there will also be FRET between the two Cy5 dyes. FRET from $Cy5_1$ to $Cy5_2$, T_1, FRET from $Cy5_2$ to $Cy5_1$, T_2. For the calculation of bi-conjugate efficiency we will consider four different pathways summarized in Table 3.2:

Table 3.2. Four potential FRET pathways.

Path I	Excitation energy is absorbed by $Cy5_1$, bounced from $Cy5_1$ to $Cy5_2$ and back, then to AuNC	$E_I = \frac{E_1}{1-(T_{12}\times T_{21})}$ (3.5)
Path II	Excitation energy is absorbed by $Cy5_1$ transferred to $Cy5_2$ then to AuNC	$E_{II} = \frac{T_{12}\times E_2}{1-(T_{12}\times T_{21})}$ (3.6)
Path III	Excitation energy is absorbed by $Cy5_2$, bounced from $Cy5_2$ to $Cy5_1$ and back, then to AuNC	$E_{III} = \frac{E_2}{1-(T_{12}\times T_{21})}$ (3.7)
Path IV	Excitation energy is absorbed by $Cy5_2$ transferred to $Cy5_1$ then to AuNC	$E_{IV} = \frac{T_{12}\times E_1}{1-(T_{12}\times T_{21})}$ (3.8)

Which gives a combined energy formula of:

$$E_{2d} = \frac{1}{2}\left(\frac{E_1(1+T_{21})+E_2(1+T_{12})}{1-(T_{12}\times T_{21})}\right) \tag{3.9}$$

If we replace E_1 and E_2 with an average NSET efficiency, E_0, and the two FRET efficiencies with an average efficiency, T, then the above equation can be simplified to:

$$E_{2d} = \frac{E_0}{(1-T)} \tag{3.10}$$

3.3. Results and discussion

3.3.1. Isolation of mono- and bi-Conjugates

Our first goal in this chapter was to develop the ability to isolate individual species of AuNC-DNA conjugates using IP-RP HPLC. Our second goal was to demonstrate their potential for self-assembly applications utilizing the quenching properties of AuNCs. With these goals in mind, we first investigated which IPRs would meet these needs. TEAA and TEA-HFIP are the most utilized IPRs in oligonucleotide characterization and purification methods. Compared to TEAA, TEA-HFIP has shown superior resolution, especially when paired with MS, due to its volatility and low adduct formation[24,41,42]. Despite these advantages, we found that fAuNCs purified

with the TEA-HFIP exhibited short shelf lives, making them unsuitable for downstream self-assembly applications.

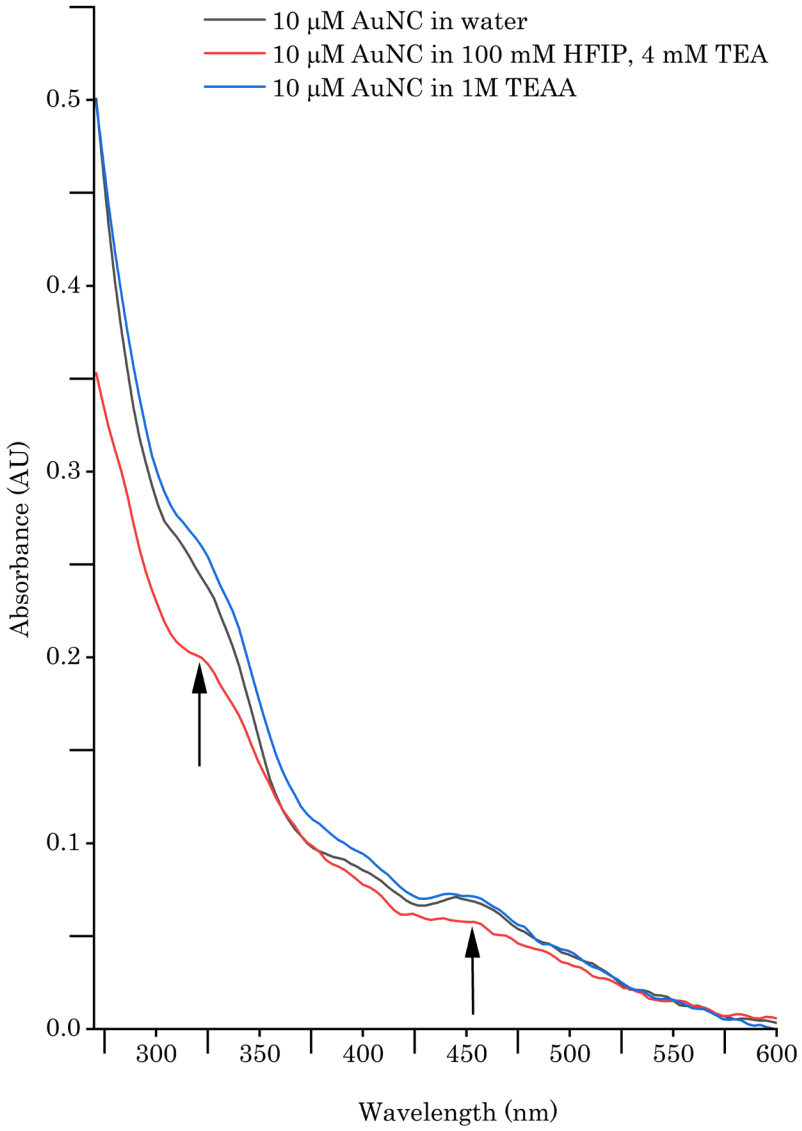

Figure 3.2. The UV-Vis spectrum of AuNC in water (black line), TEA-HFIP (red line), and TEAA (green line).

As seen in the AuNC absorbance spectra of Figure 3.3., a 10 μM AuNC sample stored in HFIP-TEA shows substantial attenuation of the characteristic peaks at 320 nm and 450 nm. The samples stored in the TEAA buffer did not show the same attenuation. An Au_{25} nanocluster has an inner core of 13 Au atoms surrounded by an outer shell of 12 Au atoms and 18 ligands. Previous optical characterization of thiol-ligand-protected Au_{25} nanoclusters

has shown that transitions at these wavelengths correlate to the outer shell of the AuNC[43]. The attenuation of these peaks indicates that HFIP is degrading the outer shell of the AuNCs. Since AuNC stability stems from the thiol-gold bonds of this outer shell, this explains the short shelf-life we observed. There are alternative MS-compatible IPRs that could be less damaging to AuNCs than HFIP-TEA [44–46]. However, since our experiments were not MS-reliant, we moved forward with TEAA as our IPR.

To evaluate the effect of different flow rates, we measured the resolution of fAuNCs using a 4.6 × 150 mm AdvanceBio Oligonucleotide C_{18}, 2.7 µm column at a flow rate range of 0.5–0.8 ml/min. The flow rates were evaluated with 75 mM TEAA and 100% HPLC grade acetonitrile for mobiles phases A and B, respectively. Elution was observed by monitoring the UV–vis absorption at the DNA absorption peak of 260 nm. For other HPLC conditions, see the figure captions. Retention time and resolution values are shown in Table 3.2. and visualized in Figure 3.4.a. We evaluated the resolution for our two peaks of interest, the mono- and di-conjugated AuNCs, using *Equation 3.2*.

Table 3.3. Resolution between Peak 2, fAuNC-(ssDNA), and Peak 3, fAuNC-$(ssDNA)_2$, was calculated using equation 3.2. For details, see the Experimental section.

Mobile Phase Flowrate (mL/min)	**Retention Time (min)**				**Resolution**
	Peak 1: AuNC	Peak 2: fAuNC-(ssDNA)	Peak 3: fAuNC-$(ssDNA)_2$	Peak 4: ssDNA	Peak 2/ Peak 3
0.5	12.20	13.63	14.09	18.09	0.583
0.7	10.44	12.00	12.44	16.12	0.683
0.8	10.18	11.78	12.21	15.92	0.680

In contrast with previous IP-RP oligonucleotide publications, we observed better resolution with higher flow rates.[24,41,47] This is because early publications used stationary phases with fully porous particles, while our experiments used superficially porous particles with a solid core. Solid core particles reduce an analyte's diffusion path through the particle, leading to more efficient mass transfer across all flow rates [48]. This more efficient mass transfer means we could utilize higher flow rates for more rapid separation of fAuNCs.

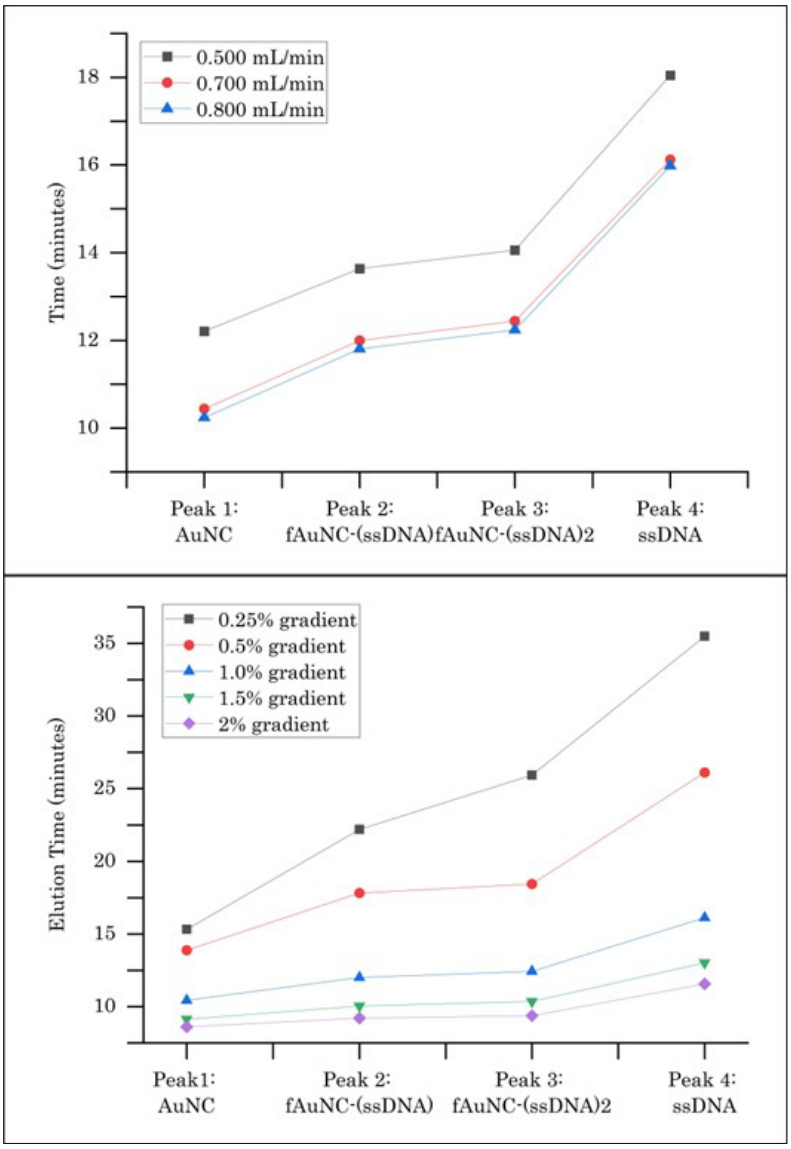

Figure 3.3. Retention of AuNC, fAuNC-ssDNA conjugates, and ssDNA with changes to flow rate (A) and method gradient(B).
(A) Other HPLC conditions: All flow rates were evaluated at 60 °C. All runs started with a 2-minute hold at 5% acetonitrile and then increased to a final concentration of 35% in 30 minutes. Higher flow rates decreased run times and resolution.
(B) Other HPLC conditions: All gradients were evaluated at 60 °C with a 0.7 mL/min flow rate. All runs started with a 2-minute hold at 5% acetonitrile and then increased to a final concentration of 35% acetonitrile according to the gradient specified. The gradient that increased the amount of acetonitrile by 0.25%/minute had the highest resolution of those evaluated.

We next evaluated method gradients that increased the percentage of acetonitrile between 0.25%/min to 2%/minute. We summarized these results in

Fig 5.b. and Appendix 1. As one would expect, the steeper gradient shortened the analysis time; however, it also reduced the separation selectivity. We achieved the highest resolution with a 0.25%/min increase of acetonitrile, with the last peak eluting at 35.49 minutes. However, despite this shallow gradient, we could still not achieve the baseline resolution necessary for purification.

Several published studies illustrate the influence of IPR concentration on peak resolution and retention[19,45,47]. Increasing the concentration of the IPR increases the hydrophobicity and retention of oligonucleotides. Following this logic, we adjusted the concentration of mobile phase A from 75 mM TEAA to 100 mM TEAA. As a result, we achieved baseline resolution between our peaks of interest with a gradient of 0.25% ACN, which started at 12% ACN, and a flow rate of 0.800 mL/min (Figure 3.5.a).

A representative chromatogram from our method is shown in Figure 3.5.a. As seen in the absorbance spectra of AuNC and TssDNA in Figure 3.5.b., DNA only absorbs at 260 nm, while AuNCs absorb at 260 and 370 nm. Therefore, absorbance at 370 nm would indicate the presence of AuNCs. Peaks 2 and 3 absorb at both 370 and 260 nm, with a higher absorbance at 260 nm than seen at Peak 1, leading us to conclude that these peaks are the mono- and di-conjugated fAuNCs. We examined the absorbance spectra collected for peaks 1-3 and 5 to support this conclusion, as seen in Figure 3.5.b. The spectra associated with peaks 2 and 3 show characteristics of both AuNC and DNA. These characteristics are most apparent at 260 nm and 325 nm.

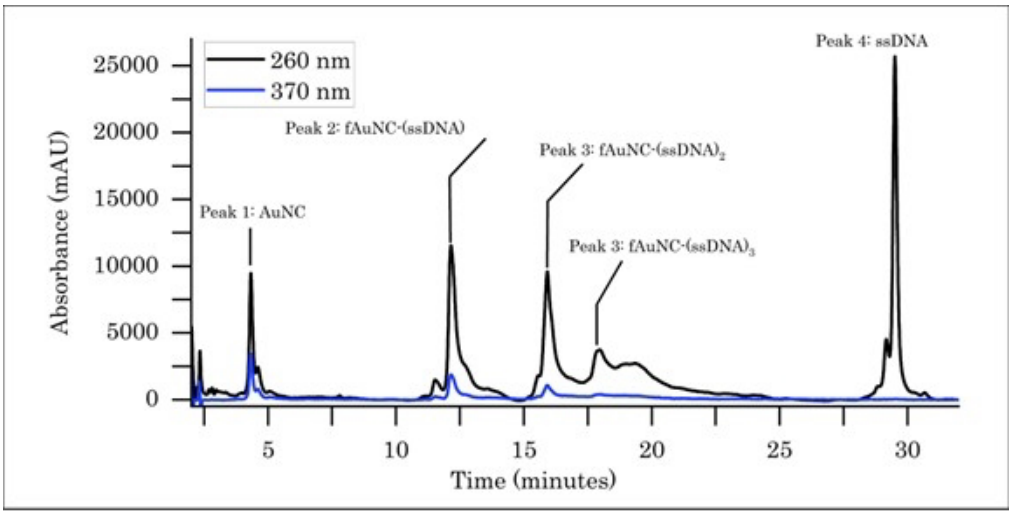

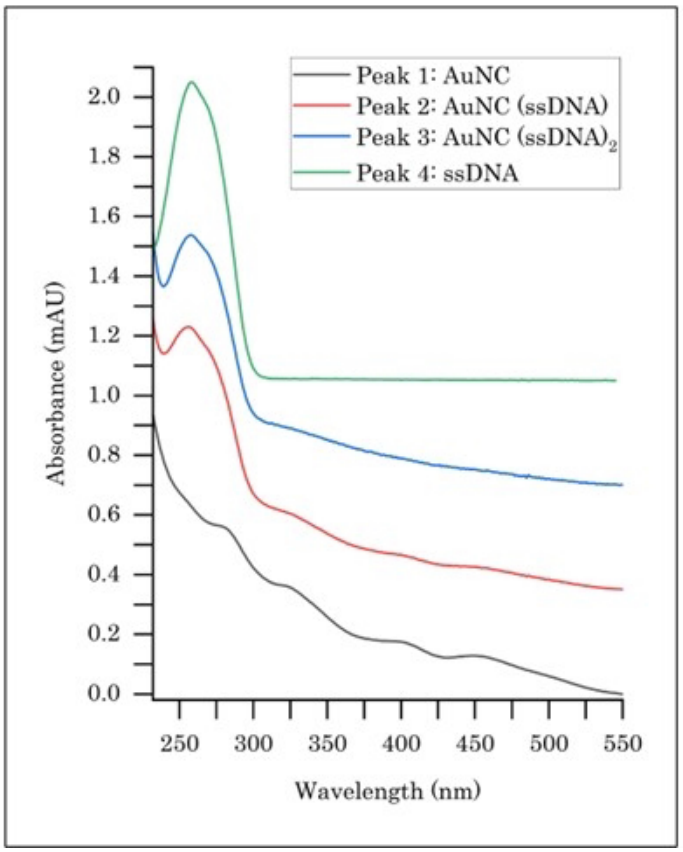

Figure 3.4. (A) Chromatogram showing baseline separation of the mono- and di-conjugates. The R_s were calculated using Equation 3.1 and determined to be 5.14. The absorbance at 260 nm (black) and 370 nm (blue) was monitored to indicate the presence of AuNCs and ssDNA. The method was run at 60 °C with a 0.800 mL/min flow rate. The method began with a 2-minute hold at 12% acetonitrile and increased by 0.25% acetonitrile/minute for 40 minutes. (B) The absorbance for peaks 1,2,3, and 5 was collected between 225 nm and 500 nm.

It is worth noting that the excess ssDNA is eluting after both conjugates. We attribute the longer retention time to the 6-carbon tether that connects the thiol to the oligonucleotide. Our investigations found that oligonucleotide modifications such as thiols, carbon tethers, and fluorescent dyes significantly affect the retention time of the oligonucleotide. As seen in Figure 3.7.b., unmodified ssDNA sequences elute early. The modifications on the other three oligonucleotides increase their hydrophobicity and, thus, their retention times. The 6-carbon tether on the thiolated ssDNA becomes buried within the ligand monolayer of the AuNC after the ligand exchange, causing the AuNC-DNA to elute before the free thiolated ssDNA with the 6-carbon tether. The hydrophobicity of the Cy5 dye causes the most significant increase in the retention of the modified oligonucleotides.

To demonstrate that HPLC-purified conjugates are suitable substrates for self-assembly, we designed an 18-mer thiolated oligonucleotide functionalized with a Cy5 (Figure 3.6.). We conjugated these ssDNA-Cy5 oligonucleotides to AuNCs as in the previous experiment. Due to the increased retention of the Cy5 oligonucleotides, we modified the HPLC method to begin at 20% acetonitrile. All other running conditions remained the same, and we achieved a high-resolution separation of AuNC-ssDNA-Cy5 conjugates, as seen in Figure 3.7.a.

In summary, we found that a shallow gradient combined with a high concentration of IPR achieves the resolution necessary to purify the fAuNCs by the extent of their oligo-ligand coverage, even when the DNA has been modified.

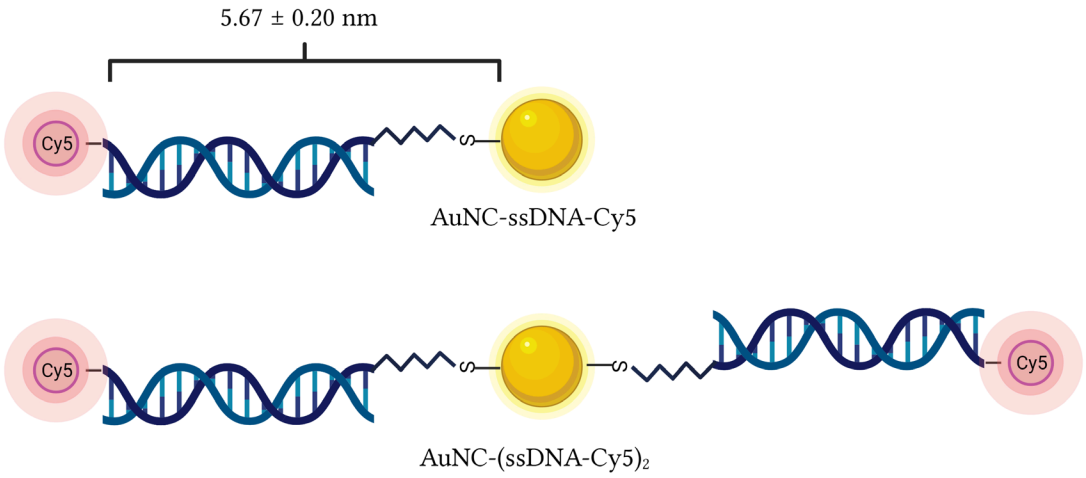

Figure 3.5. Schematic of fAuNC-(ssDNA-Cy5) and fAuNC-(ssDNA-Cy5)$_2$.

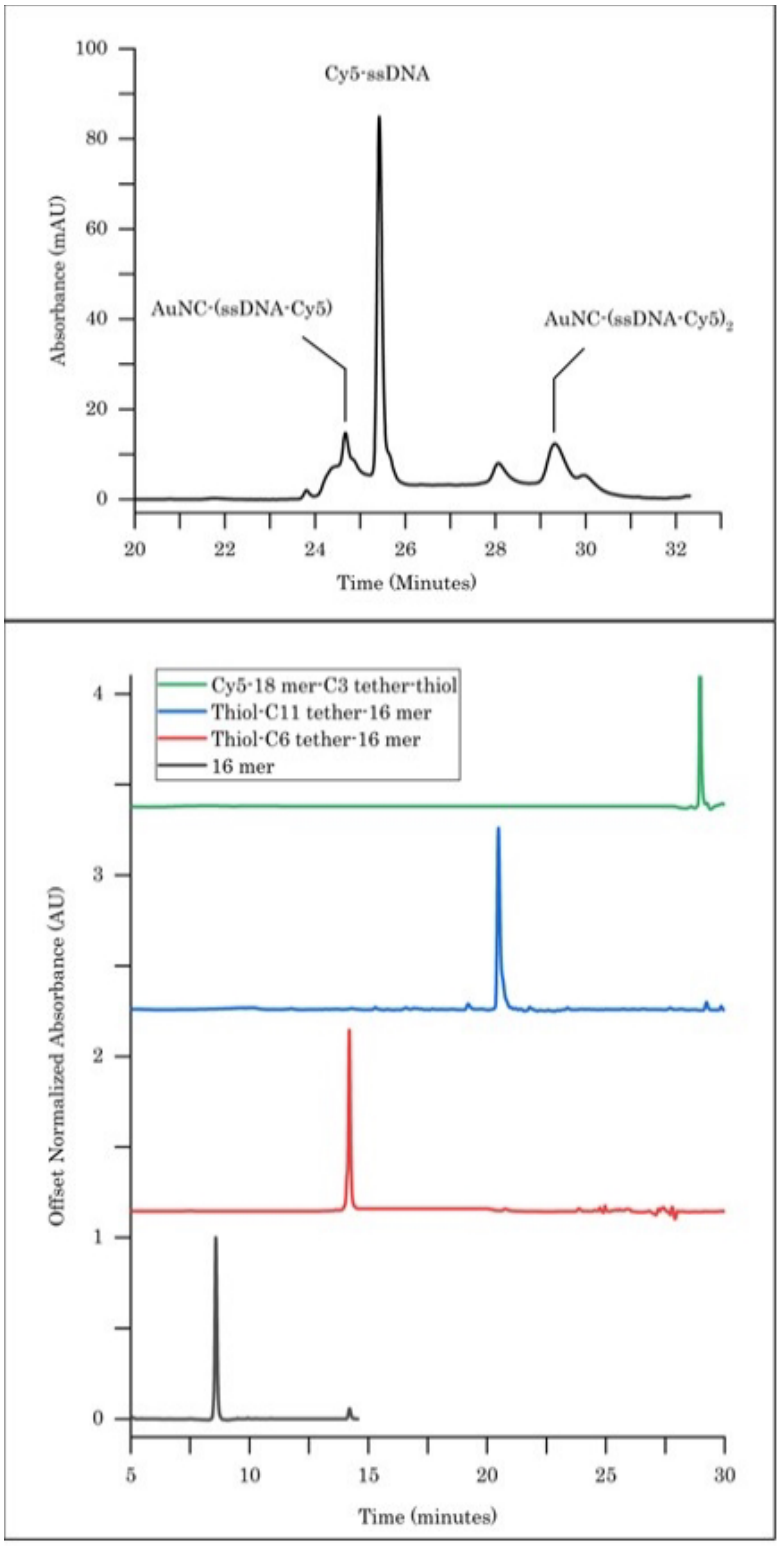

Figure 3.6. (A) Chromatogram from AuNC-ssDNA-Cy5 bioconjugation purification. (B) Staggered chromatogram showing the effect of different oligonucleotide modifications on elution times.

3.3.2. Steady-state fluorescent characterization of AuNC-(DNA-Cy5) conjugates

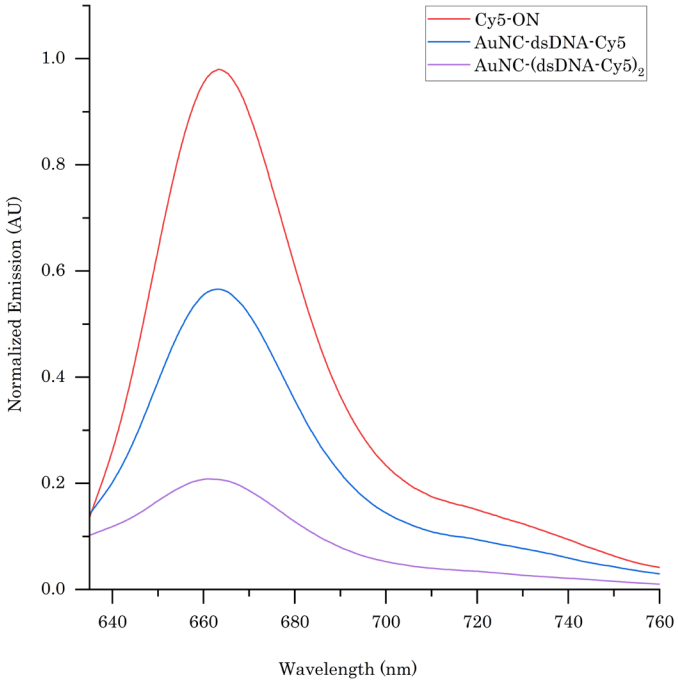

Figure 3.7. Relative fluorescent emission of 1 nM dsDNA-Cy5 (red), 1 nM AuNC-(dsDNA-Cy5) (blue) and 500 pM AuNC-$(dsDNA\text{-}Cy5)_2$ (purple).

In this section we sought to characterize the purified bio-conjugates using steady-state fluorescence spectroscopy. We used surface energy transfer (SET) to predict the quenching efficiency of the AuNC conjugated to the DNA-Cy5. Our experimental results for the mono-conjugates fell within an allowable margin of error, while the bi-conjugate showed significantly more quenching than predicted. We believe the addition quenching observed to be due self-quenching between the Cy5s at each end of the DNA ligand.

Once the ssDNA had been annealed to its complementary DNA (cDNA), our 18-mer sequence would theoretically have an end-to-end separation distance of 6.12 nm. However, the salt conditions and temperature affect oligonucleotide end-to-end distances in solutions. We simulated our experimental conditions in the course-grained modeling program oxDNA to model the end-to-end distance more accurately. The results of the end-to-end distance distribution

simulated by oxDNA can be seen in *Appendix 1.a*. At 20 °C in 0.5 M NaCl solution, we determined the mean separation distance (d) to be 5.77±0.2 nm.

AuNCs have a distance-dependent ability to quench fluorescent dyes as characterized by nanometal surface energy transfer (SET)[37,49–51]. In SET processes, energy from a photoexcited chromophore is dampened in the presence of a nanometal surface with a $1/d^4$, with d being the separation distance between the dye and metal surface[36]. To determine the theoretical quenching efficiencies between Cy5 and AuNC, d_0 was calculated using *Equation 1.5.* D_0 is the distance at which energy transfer and fluorescent emission are equally probable. We calculated a d_0 to be 5.58 nm for the Cy5 - Au_{25}(Captopril)$_{18}$ coupling. We calculated the theoretical quenching for AuNCs using *Equation 3.3.* The theoretical quenching of the assemblies is 0.46±0.03 (Appendix 2.b).

For the steady-state fluorescent experiments, we used HPLC-purified AuNC-DNA conjugates, as described in the above section. We annealed cDNA to each of the fractions collected. To ensure an equal Cy5 concentration when measuring both the mono-conjugate and bi-conjugate we diluted each sample solution to a 1 nM DNA concentration. Meaning 1 nM concentration of control and mono-conjugate, and 500 pM of b-conjugate was used for our fluorescence measurements. Using Equation 3.4 we determined the quenching efficiency of the AuNC-(dsDNA-Cy5) was 0.40±0.08. If the bi-conjugate were only energy transfer between the two dyes and the AuNC then the using the quenching efficiency was 0.76±0.04. While the quenching efficiency for the mono-conjugate is within the margin of error, the di-conjugate had a statistically significant deviation from predicted values ($p<0.001$, two-tailed, one-sample t-test, 95% confidence interval, n=8). The bio-conjugates quenching capacity was monitored for 7 days to determine their shelf-life. As can be seen in Figure 3.9., the quenching efficiency of AuNC-(dsDNA-Cy5)$_2$ has a 19% increase in quenching efficiency in that time, while the mono-conjugate losses 6% quenching capacity.

We propose that the self-quenching of Cy5 is the likely cause for the divergent behavior of the bi-conjugate. Self-quenching is typically observed at high fluorophore concentrations where the decreased mean distance between dyes leads to increased collisional quenching, formation of non-fluorescent dimers, and energy transfer[52–55]. Self-quenching has also been documented in assemblies and bio-conjugation that can eliminate the inner filter effect, and make dimerization, and collisional quenching probable[56–58]. Characterization of these assemblies indicates that dyes with small Stokes shifts have sufficient spectral overlap to participate in single-pair fluorescence resonance energy transfer (spFRET). The spFRET is due to dipole-dipole interaction and the rate

is proportional to $1/r^6$, where r is the separation distance between the dye centers. The spFRET of Cy5-Cy5 coupling has been documented in previous studies[59,60].

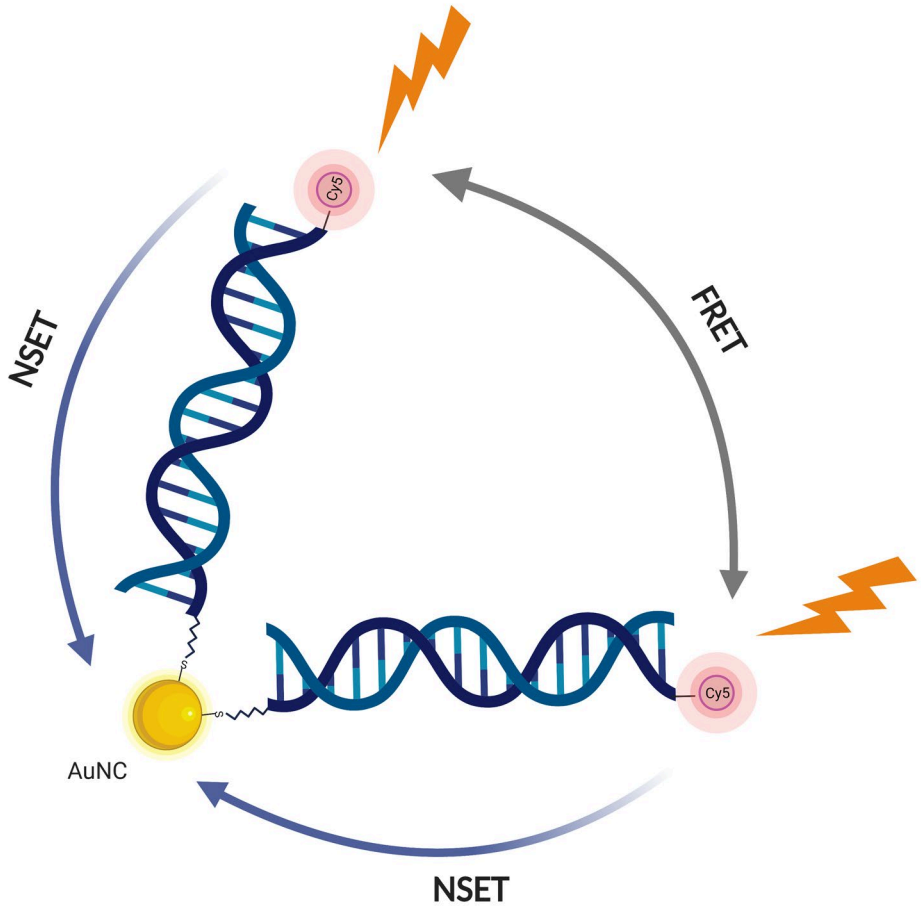

Figure 3.8. Schematic of spFRET and NSET pathways of AuNC-DNA bi-conjugate.

By tethering the two dyes to the AuNC, it increases the proximity of the dyes to each other. Thus, creating a localized concentration of dyes surrounding the AuNC. Using *Equation 1.3,* spFRET critical radius of Cy5 is 5.8 nm. With an $1/r^6$ proportionality to the energy transfer rate, the separation distances between the dyes that would produce a measurable change in photoluminescence (PL) would be 2.9-8.7 nm. The Au_{25} nanocluster is just over 1 nm in size, while each of the dsDNA ligands is roughly 2 nm in diameter and 6 nm in length. The AuNC with its captopril monolayer would provide little resistance to the ligand's range of motion. If we treat the AuNC as a hinge holding the two dsDNA-Cy5 ligands together then it would only take an 88.8° angle of separation to have a detectible change in PL. If the bi-conjugate is

behaving as a hinge it is probable that the dyes could be closer to each other than they are to the AuNC. Overall, this suggests that self-quenching, in the form of ET, collisions, or formation of dimers is likely for the AuNC-(dsDNA-Cy5)$_2$. Therefore, we suspect that the increased quenching seen in Figure 3.8. is due to a combination of SET between both dyes and the AuNC, spFRET between the two Cy5 dyes, and finally the formation of dimers. The formation of non-fluorescent dimers is permanent and will accumulate over time. Looking at the shelf-life data collected for the mono- and bi-conjugates in Figure 3.10., we see that the quenching efficiency of the bi-conjugate increases over the 7 days. We believe that this is due to the formation of non-fluorescent Cy5-Cy5 dimers over time. If we calculate the quenching efficiency of the bi-conjugate using Equation 3.10, and assume the quenching efficiency of the monoconjugate to be E_0 and the overall quenching observed to be E_{d2}, then quenching efficiency off the Cy5 FRET pair would be 0.47±0.12, which is reasonable.

Overall, we see that the AuNC-(dsDNA-Cy5) conjugate met the expectations of the model, while AuNC-(dsDNA-Cy5)$_2$ produced unpredicted results. The divergent behaviors of these two bioconjugates emphasize the need to fully characterize these moieties, especially if intended for *in vivo* applications.

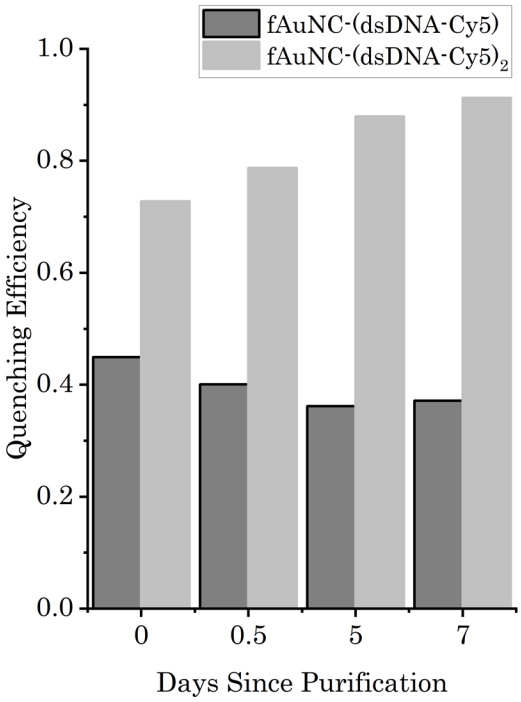

Figure 3.9. Comparison of the changes in quenching efficiency by AuNC-(dsDNA-Cy5) and AuNC-(dsDNA-Cy5)$_2$ over 7 days.

3.4. Conclusion and outlook

In conclusion, we have successfully developed a purification method that can isolate AuNC-DNA bioconjugates, $Au_{25}(Captopril)_{17}(ssDNA)$ from $Au_{25}(Captopril)_{16}(ssDNA)_2$. The IP-RP method using 100 mM TEAA, 0.800 mL/min flow rate, and a 0.25% increase in acetonitrile/min was sufficient to achieve the baseline separation necessary for purification. We further demonstrated the necessity of isolating and characterizing the individual conjugates to determine their suitability for downstream self-assembly. This method is not only more scalable than the widely used electrophoretic methods and more applicable than the purifications dependent on AuNC ligand properties. The IP-RP HPLC method presented here is likely suitable for other water-soluble AuNC-DNA conjugates. Confirming this theory is a direction worth exploring. While our experiments did not utilize MS, the size- and ligand-dependent properties of AuNC mean that MS confirmation of the AuNC-DNA conjugate composition should also be completed. One practical challenge is that HFIP, a commonly used IPR for MS detection, degrades $Au_{25}(Captopril)_{18}$. While these AuNCs are more stable in TEAA, this IPR is unsuitable for MS detection. Hence, other fluorinated alcohols compatible with MS and do not cause degradation should be explored.

3.5. References

1. Polavarapu L, Manna M, Xu QH. Biocompatible glutathione capped gold clusters as one- and two-photon excitation fluorescence contrast agents for live cells imaging. *Nanoscale*. 2011;3(2):429-434. doi:10.1039/C0NR00458H

2. Niu J, Wang X, Lv J, Li Y, Tang B. Luminescent nanoprobes for in-vivo bioimaging. *TrAC - Trends in Analytical Chemistry*. 2014;58:112-119. doi:10.1016/j.trac.2014.02.013

3. Zhang L, Wang E. Metal nanoclusters: New fluorescent probes for sensors and bioimaging. *Nano Today*. 2014;9(1). doi:10.1016/j.nantod.2014.02.010

4. Yang K, Wang S, Wang Y, Miao H, Yang X. Dual-channel probe of carbon dots cooperating with gold nanoclusters employed for assaying multiple targets. Published online 2017. doi:10.1016/j.bios.2017.01.014

5. Fernández TD, Pearson JR, Leal MP, et al. Intracellular accumulation and immunological properties of fluorescent gold nanoclusters in human dendritic cells. *Biomaterials*. 2015;43(1):1-12. doi:10.1016/J.BIOMATERIALS.2014.11.045

6. Zhang XD, Chen J, Luo Z, et al. Enhanced Tumor Accumulation of Sub-2 nm Gold Nanoclusters for Cancer Radiation Therapy. Published online 2013. doi:10.1002/adhm.201300189

7. Konishi K, Iwasaki M, Sugiuchi M, Shichibu Y. Ligand-Based Toolboxes for Tuning of the Optical Properties of Subnanometer Gold Clusters. *Journal of Physical Chemistry Letters*. 2016;7(21):4267-4274. doi:10.1021/acs.jpclett.6b01999

8. Wu Z, Jin R. On the ligand's role in the fluorescence of gold nanoclusters. *Nano Lett*. 2010;10(7):2568-2573. doi:10.1021/nl101225f

9. Yuan X, Goswami N, Chen W, Yao Q, Xie J. Insights into the effect of surface ligands on the optical properties of thiolated Au25nanoclusters. *Chemical Communications*. 2016;52(30). doi:10.1039/c6cc00857g

10. Shibu ES, Muhammed MAH, Tsukuda T, Pradeep T. Ligand exchange of Au25SG18 leading to functionalized gold clusters: Spectroscopy, kinetics, and luminescence. *Journal of Physical Chemistry C*. 2008;112(32):12168-12176. doi:10.1021/jp800508d

11. Ning X, Peng C, Li ES, et al. Physiological stability and renal clearance of ultrasmall zwitterionic gold nanoparticles: Ligand length matters. *APL Mater*. 2017;5(5). doi:10.1063/1.4978381

12. Zhang XD, Wu D, Shen X, Liu PX, Fan FY, Fan SJ. In vivo renal clearance, biodistribution, toxicity of gold nanoclusters. *Biomaterials*. 2012;33(18):4628-4638. doi:10.1016/j.biomaterials.2012.03.020

13. Zanchet D, M. Micheel C, J. Parak W, Gerion D, Paul Alivisatos A. Electrophoretic Isolation of Discrete Au Nanocrystal/DNA Conjugates. *Nano Lett*. 2000;1(1):32-35. doi:10.1021/nl005508e

14. Claridge SA, Liang HW, Basu SR, Fréchet JMJ, Alivisatos AP. Isolation of Discrete Nanoparticle−DNA Conjugates for Plasmonic Applications. *Nano Lett*. 2008;8(4):1202-1206. doi:10.1021/nl0802032

15. Sperling RA, Pellegrino T, Li JK, Chang WH, Parak WJ. Electrophoretic separation of nanoparticles with a discrete number of functional groups. *Adv Funct Mater*. 2006;16(7):943-948. doi:10.1002/ADFM.200500589

16. Pellegrino T, Sperling RA, Alivisatos AP, Parak WJ. Gel Electrophoresis of Gold-DNA Nanoconjugates. *J Biomed Biotechnol*. 2007;26796. doi:10.1155/2007/26796

17. Martin M. F. Choi †, Alicia D. Douglas and, Murray* RW. Ion-Pair Chromatographic Separation of Water-Soluble Gold Monolayer-Protected Clusters. *Anal Chem*. 2006;78(8):2779-2785. doi:10.1021/AC052167M

18. Niihori Y, Kikuchi Y, Shima D, et al. Separation of Glutathionate-Protected Gold Clusters by Reversed-Phase Ion-Pair High-Performance Liquid Chromatography. *Ind Eng Chem Res*. 2017;56(4):1029-1035. doi:10.1021/acs.iecr.6b03814

19. Donegan M, Nguyen JM, Gilar M. Effect of ion-pairing reagent hydrophobicity on liquid chromatography and mass spectrometry analysis of oligonucleotides. *J Chromatogr A*. 2022;1666:462860. doi:10.1016/J.CHROMA.2022.462860

20. Enmark M, Harun S, Samuelsson J, et al. Selectivity limits of and opportunities for ion pair chromatographic separation of oligonucleotides. *J Chromatogr A*. 2021;1651:462269. doi:10.1016/J.CHROMA.2021.462269

21. Close ED, Nwokeoji AO, Milton D, et al. Nucleic acid separations using superficially porous silica particles. *J Chromatogr A*. 2016;1440:135. doi:10.1016/J.CHROMA.2016.02.057

22. Macnair JE, Lewis KC, Jorgenson JW, et al. Effect of Pressure, Particle Size, and Time on Optimizing Performance in Liquid Chromatography. *Anal Chem*. 2009;81(13):5342-5353. doi:10.1021/AC9001244

23. Gong L. Analysis of oligonucleotides by ion-pairing hydrophilic interaction liquid chromatography/electrospray ionization mass spectrometry. *Rapid Communications in Mass Spectrometry*. 2017;31(24):2125-2134. doi:10.1002/rcm.8004

24. Gilar M, Fountain KJ, Budman Y, et al. Ion-pair reversed-phase high-performance liquid chromatography analysis of oligonucleotides:: Retention prediction. *J Chromatogr A*. 2002;958(1-2):167-182. doi:10.1016/S0021-9673(02)00306-0

25. Fountain KJ, Gilar M, Gebler JC. Analysis of native and chemically modified oligonucleotides by tandem ion-pair reversed-phase high-performance liquid chromatography/electrospray ionization mass spectrometry. *Rapid Communications in Mass Spectrometry*. 2003;17(7):646-653. doi:10.1002/rcm.959

26. Huber CG, Krajete A. Analysis of nucleic acids by capillary ion-pair reversed-phase HPLC coupled to negative-ion electrospray ionization mass spectrometry. *Anal Chem*. 1999;71(17):3730-3739. doi:10.1021/ac990378j

27. Miyata S, Miyaji H, Kawasaki H, et al. Antimicrobial photodynamic activity and cytocompatibility of Au25(Capt)18 clusters photoexcited by blue LED light irradiation. *Int J Nanomedicine*. 2017;12:2703-2716. doi:10.2147/IJN.S131602

28. McLean A, Wang R, Huo Y, et al. Synthesis and Optical Properties of Two-Photon-Absorbing Au25(Captopril)18-Embedded Polyacrylamide Nanoparticles for Cancer Therapy. *ACS Appl Nano Mater*. 2020;3(2):1420-1430. doi:10.1021/acsanm.9b02272

29. Kumar S, Jin R. Water-Soluble Au 25 (Capt) 18 Nanoclusters: Synthesis, Thermal Stability, and Optical Properties. Accessed August 8, 2017. http://www.rsc.org/suppdata/nr/c2/c2nr30833a/c2nr30833a.pdf

30. Kumar S, Jin R. Water-soluble Au25(Capt)18 nanoclusters: synthesis, thermal stability, and optical properties. *Nanoscale*. 2012;4(14):4222-4227. doi:10.1039/c2nr30833a

31. Fornstedt T, Forssén P, Westerlund D. Basic HPLC Theory and Definitions: Retention, Thermodynamics, Selectivity, Zone Spreading, Kinetics, and Resolution.

32. Snodin BEK, Schreck JS, Romano F, Louis AA, Doye JPK. *Coarse-Grained Modelling of the Structural Properties of DNA Origami*. Accessed January 3, 2019. https://arxiv.org/pdf/1809.08430.pdf

33. Poppleton E, Romero R, Mallya A, Rovigatti L, Šulc P. OxDNA.org: a public webserver for coarse-grained simulations of DNA and RNA nanostructures. *Nucleic Acids Res*. 2021;49(W1):W491-W498. doi:10.1093/NAR/GKAB324

34. Šulc P, Romano F, Ouldridge TE, Rovigatti L, Doye JPK, Louis AA. Sequence-dependent thermodynamics of a coarse-grained DNA model. *J Chem Phys*. 2012;137(13):135101. doi:10.1063/1.4754132

35. Ouldridge TE, Louis AA, Doye JPK. DNA nanotweezers studied with a coarse-grained model of DNA. *Phys Rev Lett*. 2010;104(17):178101. doi:10.1103/PHYSREVLETT.104.178101/FIGURES/5/MEDIUM

36. Persson BNJ, Lang ND. Electron-hole-pair quenching of excited states near a metal. *Phys Rev B*. 1982;26(10):5409-5415. doi:10.1103/PhysRevB.26.5409

37. T. L. Jennings, M. P. Singh and, Strouse* GF, Jennings TL, Singh MP, Strouse GF. Fluorescent lifetime quenching near d = 1.5 nm gold nanoparticles: Probing NSET validity. *J Am Chem Soc*. 2006;128(16):5462-5467. doi:10.1021/ja0583665

38. Breshike CJ, Riskowski RA, Strouse GF. Leaving Fö rster Resonance Energy Transfer Behind: Nanometal Surface Energy Transfer Predicts the Size-Enhanced Energy Coupling between a Metal Nanoparticle and an Emitting Dipole. *J Phys Chem C*. 2013;117. doi:10.1021/jp407259r

39. Lakowicz JR. *Principles of Fluorescence Spectroscopy*. Springer; 2006. doi:10.1007/978-0-387-46312-4

40. Gennis RB, Cantor CR. Use of Nonspecific Dye Labeling for Singlet Energy-Transfer Measurements in Complex Systems. A Simple Model. *Biochemistry*. 1972;11(13). doi:10.1021/bi00763a020

41. Apffel A, Chakel JA, Fischer S, Lichtenwalter K, Hancock WS. Analysis of Oligonucleotides by HPLC-Electrospray Ionization Mass Spectroscopy. *Anal Chem*. 1997;69(7):1320-1325. doi:10.1021/ac960916h

42. Huber CG, Oberacher H. Analysis of nucleic acids by on-line liquid chromatography–Mass spectrometry. *Mass Spectrom Rev*. 2001;20(5):310-343. doi:10.1002/MAS.10011

43. Zhu M, Aikens CM, Hollander FJ, Schatz GC. Correlating the Crystal Structure of A Thiol-Protected Au 25 Cluster and Optical Properties. *J Am Chem Soc*. 2008;130:5883-5885. doi:10.1021/ja801173r

44. Liu R, Ruan Y, Liu Z, Gong L. The role of fluoroalcohols as counter anions for ion-pairing reversed-phase liquid chromatography/high-resolution electrospray ionization mass spectrometry analysis of oligonucleotides. *Rapid Communications in Mass Spectrometry*. 2019;33(7):697-709. doi:10.1002/RCM.8386

45. Gong L, McCullagh JSO. Comparing ion-pairing reagents and sample dissolution solvents for ion-pairing reversed-phase liquid chromatography/electrospray ionization mass spectrometry analysis of oligonucleotides. *Rapid Communications in Mass Spectrometry*. 2014;28(4):339-350. doi:10.1002/RCM.6773

46. Basiri B, van Hattum H, van Dongen WD, Murph MM, Bartlett MG. The role of fluorinated alcohols as mobile phase modifiers for LC-MS analysis of

oligonucleotides HHS Public Access. *J Am Soc Mass Spectrom*. 2017;28(1):190-199. doi:10.1007/s13361-016-1500-3

47. G. Huber C, Krajete A. Analysis of Nucleic Acids by Capillary Ion-Pair Reversed-Phase HPLC Coupled to Negative-Ion Electrospray Ionization Mass Spectrometry. *Anal Chem*. 1999;71(17):3730-3739. doi:10.1021/ac990378j

48. Kiss I, Bacskay I, Kilár F, Felinger A. Comparison of the mass transfer in totally porous and superficially porous stationary phases in liquid chromatography. *Anal Bioanal Chem*. 2010;397:1307-1314. doi:10.1007/s00216-010-3627-6

49. Yun CS, Javier A, Jennings T, et al. Nanometal surface energy transfer in optical rulers, breaking the FRET barrier. *J Am Chem Soc*. 2005;127(9):3115-3119. doi:10.1021/JA043940I

50. Jennings TL, Singh MP, Strouse GF. Fluorescent lifetime quenching near d = 1.5 nm gold nanoparticles: probing NSET validity. *J Am Chem Soc*. 2006;128(16):5462-5467. doi:10.1021/JA0583665

51. Ruppin R. Decay of an excited molecule near a small metal sphere. *J Chem Phys*. 1998;76(4):1681. doi:10.1063/1.443196

52. Bae W, Yoon TY, Jeong C. Direct evaluation of self-quenching behavior of fluorophores at high concentrations using an evanescent field. *PLoS One*. 2021;16(2 February 2021). doi:10.1371/journal.pone.0247326

53. Zhuang X, Ha T, Kim HD, Centner T, Labeit S, Chu S. *Fluorescence Quenching: A Tool for Single-Molecule Protein-Folding Study*. www.pnas.org

54. Munkholm C, Parkinson DR, Walt DR. *Intramolecular Fluorescence Self-Quenching of Fluoresceinamine*. Vol 112. CRC Press; 1990. https://pubs.acs.org/sharingguidelines

55. Penzkofer A, Lu ' Y. *FLUORESCENCE QUENCHING OF RHODAMINE 6C IN METHANOL AT HIGH CONCENTRATION*. Vol 103.; 1986.

56. Harms GS, Orr G, Montal M, Thrall BD, Colson SD, Lu HP. *Probing Conformational Changes of Gramicidin Ion Channels by Single-Molecule Patch-Clamp Fluorescence Microscopy*. Vol 85.; 2003.

57. Quinn SD, Dalgarno PA, Cameron RT, et al. Real-time probing of β-amyloid self-assembly and inhibition using fluorescence self-quenching between neighbouring dyes. *Mol Biosyst*. 2014;10(1):34-44. doi:10.1039/c3mb70272c

58. Conroy EM, Li JJ, Kim H, Algar WR. Self-Quenching, Dimerization, and Homo-FRET in Hetero-FRET Assemblies with Quantum Dot Donors and Multiple Dye Acceptors. *Journal of Physical Chemistry C*. 2016;120(31):17817-17828. doi:10.1021/acs.jpcc.6b05886

59. Biaggne A, Kim YC, Melinger JS, Knowlton WB, Yurke B, Li L. Molecular dynamics simulations of cyanine dimers attached to DNA Holliday junctions. *RSC Adv*. 2022;12(43):28063-28078. doi:10.1039/d2ra05045e

60. Berlier JE, Rothe A, Buller G, et al. *Quantitative Comparison of Long-Wavelength Alexa Fluor Dyes to Cy Dyes: Fluorescence of the Dyes and Their Bioconjugates*. Vol 51.; 2003. http://www.jhc.org

3.6. Appendix

Appendix 3.1. Resolution between Peak 2, fAuNC-(ssDNA), and Peak 3, fAuNC-$(ssDNA)_2$, was calculated using equation 3.2. For details, see the Experimental section.

Gradient Slope (% ACN/min)	**Retention Time (min)**				**Resolution**
	Peak 1: AuNC	Peak 2: fAuNC-(ssDNA)	Peak 3: fAuNC-$(ssDNA)_2$	Peak 4: ssDNA	Peak 2/ Peak 3
0.25	15.33	22.20	25.93	35.49	0.911
0.5	13.88	17.82	18.44	26.11	0.740
1.0	10.44	12.00	12.44	16.12	0.683
1.5	9.13	10.05	10.31	13.02	0.364
2.0	8.61	9.21	9.38	11.57	0.278

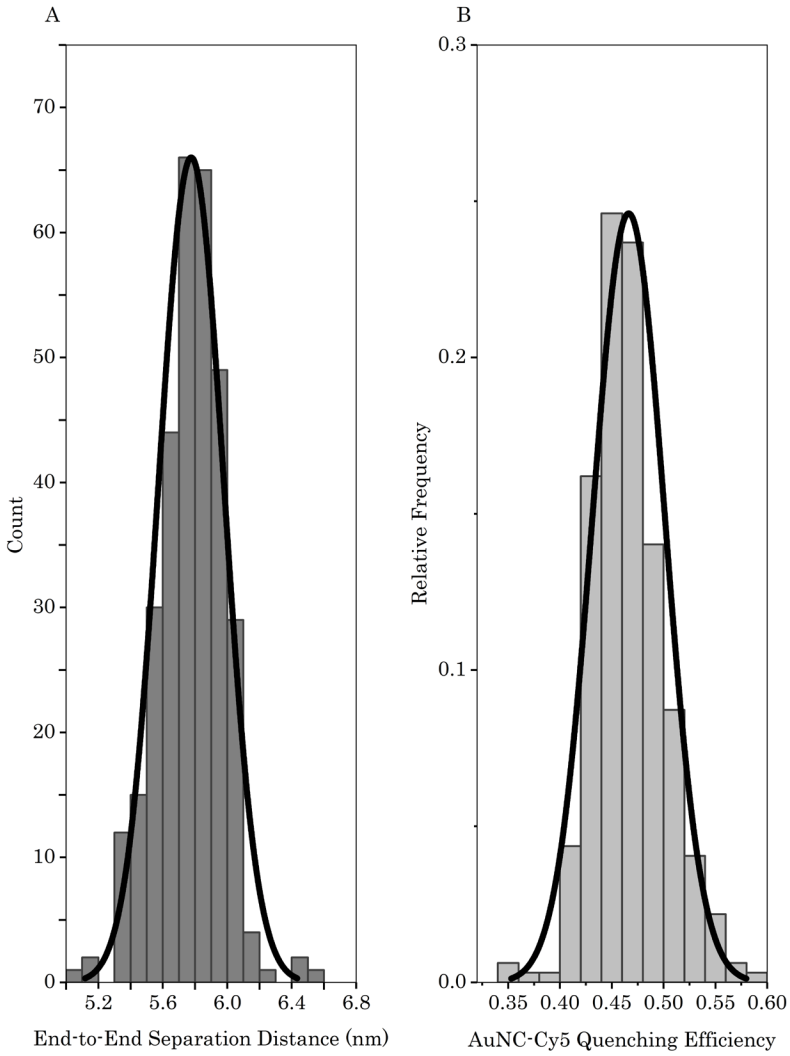

Appendix 3.2. (A) Histogram of the end-to-end separation distance of 18- mer double-stranded sequence in 0.25 M NaCl showing a separation distance of 5.77±0.20 nm. (B) Theoretical quenching for the AuNC-Cy5 conjugates shows a quenching efficiency of 0.46±0

Chapter 4

Self-assembly of Gold Nanoclusters on DNA Origami

4.1. Introduction

The coupling of AuNCs with other nanomaterials enables properties unavailable with isolated AuNCs. Such coupling interactions are sensitive to geometric and spatial orientation between AuNC and materials such as dyes, nanoparticles and other NCs. The characterization of such couplings requires precise programmed assemblies of multiple nanomaterials on a single template. Synthesizing such materials remains challenging and is impeding progress in understanding and controlling these interactions. Despite the advancement of AuNC self-assembly methods, currently none meet these needs.

Current methods of AuNC self-assembly have been limited to techniques such as crosslinking and surface synthesis. Yahia-Ammar *et al.* assembled AuNCs nanogels by mixing the negatively charged AuNCs with a cationic polymer. This crosslinking technique can assemble monodisperse AuNC assemblies but cannot control the placement of AuNCs and other nanomaterials. Dyads of AuNCs and organic dyes have been made by functionalizing both materials with ssDNA and using base-pairing to assemble them. This method does allow nanometer scale separations between AuNCs and organic dyes but with some significant limitations. First, these assemblies are limited to dyads and thus unable to create varied geometrical arrangements. Secondly, the distance separation between AuNCs and organic dyes is limited to dsDNA persistence lengths. Li *et al.* assembled patterns of AuNCs using a DNA origami tile surface seeded with thiol groups that served as AuNC nucleation sites in a $HAuCl_4 \cdot H_2O$ solution. However, this surface synthesis showed arbitrary patterning and inconsistent distance separations. Moreover, due to the difficulty in characterizing the AuNCs formed on that surface, the size and composition of the AuNCs were unknown.

A templated-directed assembly such as DNA origami would be able to achieve precise separations between multiple nanomaterials. Purified AuNC-DNA with discrete numbers of LDNA are ideal for such DNA-directed assemblies. While such assemblies have not yet been achieved for couplings involving AuNCs, they have been used with materials such as AuNPs [1–4], quantum dots [5], fluorescent dyes [6].

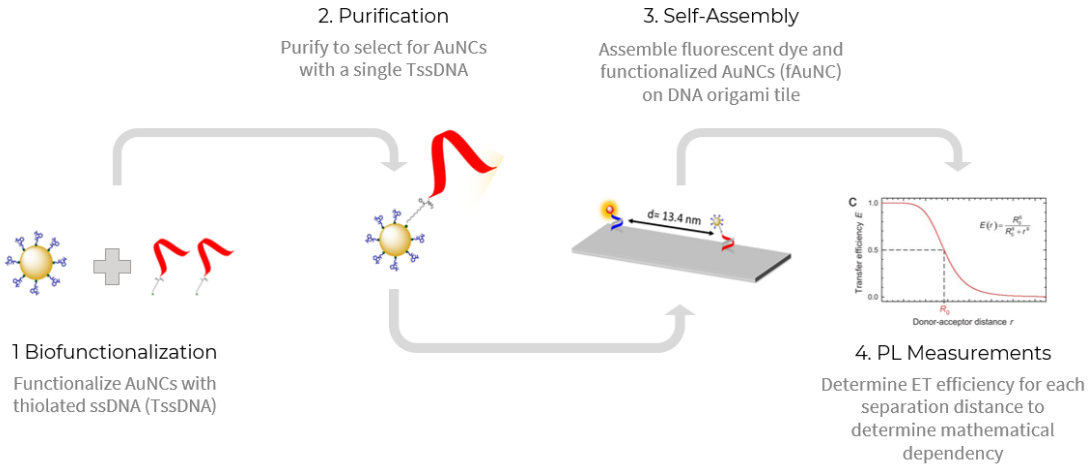

Figure 4.1. Schematic illustration of the assembly of AuNC-DNA conjugates on a DNA origami tile. Starting with $Au_{25}(Captopril)_{18}$ solution, a ligand exchange is performed to replace captopril ligands with thiolated LDNA resulting in $Au25(Captopril)_{18-n}(DNA)_n$. A fraction containing $Au_{25}(Captopril)_{17}(DNA)$ is collected and concentrated following IP-RP HPLC purification. The AuNC-DNA conjugates are then annealed to a DNA origami tile functionalized with a single Cy5 dye. To confirm that the AuNC-DNAs are assembled at discreet distances from the dye, PL measurement were taken of the assemblies.

Herein we show a new strategy to position oligonucleotide functionalized AuNCs (fAuNCs) at specific separations from a Cy5 fluorophore on a DNA origami tile. Using $Au_{25}(Captopril)_{17}(DNA)$ conjugates purified using the IP-RP HPLC technique developed in Chapter 3 were annealed to the DNA origami tile. After annealing these AuNC-DNA to capture strands on the DNA origami tile, precise assemblies on the DNA origami tile surface were confirmed using AFM. Coupled interactions between the AuNC and fluorophore were measured using static and lifetime PL measurements. Steady-state fluorescence spectroscopy measurements demonstrated a decrease in relative fluorescence proportional to the number and position of AuNC-DNA relative to Cy5 over time.

4.2. Methods and materials

4.2.1. DNA preparation

The thiolated ssDNA (TssDNA) sequence was purchased from Integrated DNA Technologies (Coralville, IA, US). The sample arrived lyophilized in disulfide form and was then reconstituted to 200 µm with ultrapure water from the Barnstead Nanopure system (Thermo Fisher Scientific, Houston, TX, US). To reduce the disulfide form to the thiol form

needed for the AuNC ligand exchange, the TssDNA was mixed with Tris (2 carboxyethyl) phosphine hydrochloride (TCEP) (Thermo Fisher Scientific) in 200 µL PCR tube with a 1000:1 TCEP to DNA ratio. The PCR tube was backfilled with nitrogen gas and vortexed for 30 minutes. The reduced TssDNA was purified using a 3 kDa molecular cutoff filter (Sigma Millipore, St. Louis, MO, US). The TCEP/TssDNA solution was added to the filter and, filled to 450 µL, spun for 30 minutes at 14,000×g. These steps were repeated three times. Next, 250 µL was added and spun for 5 minutes for the final solvent exchange at 14,000×g. After the final spin, the filter was inverted and centrifuged at 10,000×g for 5 minutes. Multiple solvent exchange steps are necessary to remove any remaining TCEP; otherwise, it will degrade the AuNC in the ligand exchange step. The final TssDNA concentration was determined using a NanoDrop™ ND-1000 spectrophotometer (Thermo Fisher Scientific).

4.2.2. Gold nanocluster synthesis

Gold nanoclusters were obtained through a collaboration with the Jin research group at Carnegie-Mellon. The preparation and characterization have been reported in previous publication[7]. Briefly, $HAuCl_4 \cdot 3H_2O$ (78.7 mg) and TOABr (126.8 mg) were dissolved in 10 mL of methanol and stirred vigorously. After 20 minutes 5 mL of methanol containing 217.2 mg of captopril was injected into the solution. After 30 minutes 2 mmol of $NaBH_4$ was added and the solution was mixed for another 8 hours. The mixture was then centrifuged and the AuNCs were precipitated with a methanol extraction.

4.2.3. Bioconjugation of oligonucleotides to gold nanoclusters

Ultrapure water was added to PAGE purified and desiccated AuNCs. The AuNC solution concentration was determined using Nanodrop and $\varepsilon_{310\ nm}=3.6\times10^4\ M^{-1}\ cm^{-1}$. A 50 µL ligand exchange solution with 18 µM TssDNA, 180 µM AuNC, and 0.1 M NaCl was mixed in a 200 µL PCR tube. The PCR tube was then backfilled with nitrogen gas and vortexed overnight.

4.2.4. Bio-conjugated gold nanocluster purification

Functionalized gold nanoclusters (fAuNCs) were purified using an IP-RP HPLC method on an Agilent 1200 series with a manual injector, heated column compartment, and variable wavelength detector set to monitor 260 nm. All separations were done using AdvanceBio Oligonucleotides C18 4.6x150 mm column with 2.7 um particle size.

Mobile phase A was HPLC grade methanol (Thermo Fisher Scientific), and mobile phase B was a 75 mM triethyl ammonium acetate (TEAA). Mobile phase B was prepared by mixing 2.61 mL HPLC grade TEA (Thermo Fisher

Scientific) and 1.05 mL HPLC grade glacial acetic acid (Thermo Fisher Scientific) to 100 µL of ultrapure H2O and then filled to 250 mL with ultrapure water. pH was adjusted to 7.00 +/- 0.05. 25 µL of the fAuNC ligand exchange solution was injected at 60 C with a 0.5 mL/minute flow rate. The mobile phase gradient was 20% mobile phase B with a 2-minute hold, then increased to 50% B in 38 minutes.

A fraction was collected from 25-27 minutes, and a solvent exchange was performed using an Amicon 3 kDa molecular cutoff filter. The collected fraction was added to the molecular weight cutoff (MWCO) filter, then spun at 14,000×g for 25 minutes, then ultrapure water was added to a final volume of 450 µL. These steps were repeated twice before the MWCO filter was inverted and spun at 10,000 × g for 5 minutes. The absorption spectra for the concentrated fractions were collected using NanoDrop™.

4.2.5. DNA Origami Formation

The rectangular DNA origami tile structure was adapted from publication[8] using caDNAno software[9]. The complete list of DNA staple sequences for tile structures is given in Appendix Table 1. Labeling the DNA origami structure with Cy5 was done by modifying the 3' end of the 8[64] staple. Staples 10[64] and 8[79] were modified by adding the AC complementary sequence to the 3' end. The modified staples and capture sequences are summarized in Table 1.

The synthetic oligonucleotide staple sequences and Cy5-modified staples were purchased from Integrated DNA technologies. Single-stranded M13mp18 scaffold DNA was purchased from New England Biolabs (Ipswich, MA, US). Tile designs 1, 2, and 3 were annealed by replacing the staples at 10[64] and /or 8[79]. The scaffold DNA was mixed with the staple oligonucleotides in a 1:5 molar ratio. Different tile designs were annealed by replacing staples 10[64] and/or 8[79]. The final concentrations of folding solutions were 10 nM scaffold strand and 50 nM of each staple strand, 12 mM $MgCl_2$, and 1X TAE. The mixture was then thermally annealed according to a previously published protocol[10]. The folded tiles were purified from excess staple sequences with a previously published micro-centrifugal molecular cutoff filter protocol[11].

4.2.6. Course-grained modeling

Course-grain simulations were performed in oxDNA to estimate the fAuNC surface to fluorophore separation distances[12,13]. All simulations were run with 0.5 M salt concentrations.

4.2.7. Atomic force microscopy

All atomic force microscopy (AFM) images were collected under the imaging buffer at room temperature. The AFM probes (Model SNL-10, Bruker Nano Inc., Santa Barbara, CA, US) with tapping-mode imaging on a NTEGRA AFM (NT-MDT America, Tempe, AZ, US). Images were processed using Gwyddion SPM Image visualization software.

20 mm mica discs (Ted Pella Inc., Redding, CA, USA) were cleaved using packaging tape. The mica surface was prepared by incubating with 5 mM $NiAc_2$, 0.1×TAE, for 2 min. Next, the solution was removed and replaced with the annealed tile solution. The tiles were incubated on the mica for 1 minute before adding 12.5 mM $MgAc_2$, 0.1×TAE. This was incubated for 1 min before being replaced with the imaging buffer (5 mM $NaAc_2$, 0.1×TAE).

4.2.8. Steady-state fluorescence measurements

Steady-state fluorescence measurements were taken with a HORIBA Jobin-Yvon Fluorolog (Horiba, Kyoto, Japan) with a Xenon lamp excitation source and a HORIBA Microsense cuvette. Excitation and emission band passes were set to 5 nm, and the integration time was 45 seconds. 8 µL of fAuNC annealed or control tile solutions were excited at 590 nm. The experimental efficiency was calculated using Equation 3.4:

4.2.9. Nanometal Surface Energy Transfer (SET)

The critical distance (d_0) was calculated using *Equation 1.5*, where Φ_{dye} is the fluorescence quantum yield of the donor in the absence of the acceptor, and c is the speed of light in a vacuum. The energy transfer efficiency was calculated using Equation 1.7, where $k_{D\rightarrow A_i}$ is the ET rate between the donor and a single acceptor, k_{D_0} is the decay rate of the donor in the absence of the AuNC. "n" depends on which ET mechanism is employed; n=4 for SET and n=6 for FRET.

4.3. Results and discussion

Figure 4.1. is a schematic demonstrating the goals of the Chapter 4 experiments. In order to achieve precise assemblies of AuNCs in proximity to a fluorophore, we first functionalized the AuNCs with ssDNA and purified them to remove excess DNA and AuNCs. We designed three different DNA origami tiles that would each have a single fluorophore and either one or two AuNCs. These assemblies were characterized with AFM and characterization of ET with fluorescence spectroscopy.

4.3.1. Bioconjugation of gold nanoclusters with oligonucleotides

The first step toward nanometer precision AuNC self-assembly on DNA origami is synthesizing and purifying AuNC-DNA conjugates. If AuNCs are annealed to the DNA origami in the presence of free DNA ligands, capture sequences could bind to either free ligands or AuNCs. This would result in a DNA origami solution that resulted in less quenching than predicted due to the absence of AuNCs at some of the capture sites. As the previous chapter shows, mono-functionalized AuNCs have more predictable results and cannot bind to multiple origami simultaneously.

The Jin group from Carnegie Mellon synthesized and characterized $Au_{25}(Captopril)_{18}$ nanoclusters[14]. These nanoclusters are water-soluble, stable up to 80 °C, and stable under salt and pH changes[7].

Extending selected DNA origami staples and using a complimentary thiolated oligonucleotide to bioconjugate AuNCs, those AuNCs should specifically bind to the DNA origami tile through hybridization between thiol-modified DNA ligands and the set staples. For our experiments, we used a 16-mer oligonucleotide modified with a six-carbon linker and -SH group at the 5' end that will be referred to as NCD.

To ensure the accuracy of downstream applications, we had to ensure fAuNCs and not excess NCDs occupied these AuNC capture sequences. Therefore, one of our first experiments incorporated the reduced NCD into the folding process of the DNA origami tiles. The assumption was that excess NCDs would be easily removed during tile purification, and the exposed thiol could bioconjugate with the AuNCs. However, we found that exposing tiles to the AuNC concentrations necessary to ensure bioconjugation resulted in substantial degradation of the tiles, rendering them unusable for further applications. From this, we knew it was not only essential to remove excess NCDs but also to remove excess AuNCs before beginning the self-assembly process.

We want to isolate the mono-conjugates to ensure one tile for every fAuNC. Therefore, we used the ion-paired reversed phased (IP-RP) HPLC method developed in Chapter 3 to isolate the mono-conjugated fAuNCs.

4.3.2. Formation of DNA origami tiles

To anneal purified fAuNCs on the folded and purified DNA origami tiles, 20 nM of fAuNCs, 2 nM DNA Origami tiles, and 8 mM $MgCl_2$ were incubated at 25 °C for 180 minutes. The DNA origami rectangle (100 ×70 nm) is folded from one m13mp18-scaffold strand and 187 staple strands.[8,10] Each of the origami tiles also contains one Cy5-modified staple. The folding process directly inserts the fluorophore-modified staple strand into the DNA origami.

To adapt published DNA origami tiles for AuNC self-assembly, we appended "capture" sequences to the 3' end of two staple sequences. We constructed three Cy5 functionalized DNA origami designs, the sole difference being the position and/or number of AuNC capture staples. These designs are represented in Figure 4.2.a., where the blue stars indicate the positions of the Cy5 dye, and each yellow dot represents the position of the AuNC capture sequences. After the assembly of fAuNCs onto tiles, the assemblies were characterized on mica using atomic force microscopy (AFM). Figure 4.2.b. shows 1 AuNC on D1 and D2. Need to describe what is observed under AFM and interpret the results.

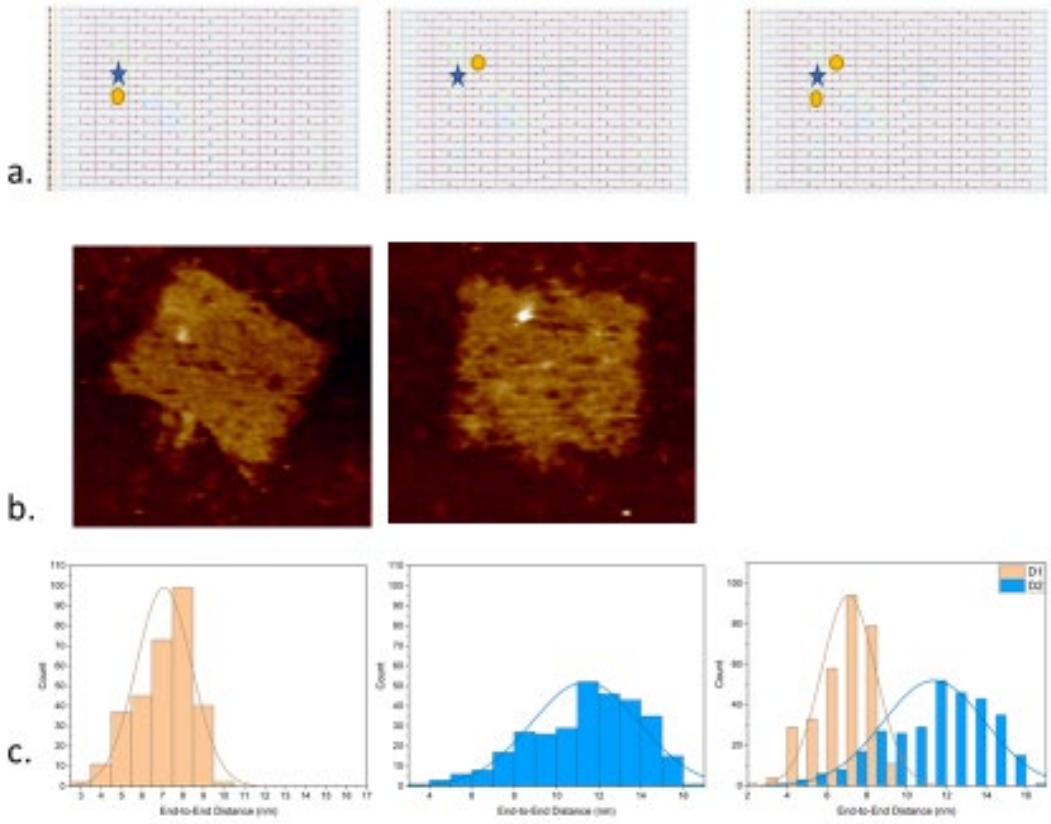

Figure 4.2. (A) Graphic representations of DNA origami tile designs. The gold circles represent the placement of the fAuNCs, while the blue stars represent the placement of the Cy5 dye (B) AFM images of tiles D1 and D2 (C) Histograms of the end-to-end separation distances between the fAuNC surface and the Cy5 dye.

Although DNA origami is substantially more rigid than a dsDNA template used to organize AuNCs, fluctuations in the origami may alter the separations and hence the energy transfer efficiencies. Therefore, mean separation distances were calculated using coarse-grained oxDNA simulations.

oxDNA has been used in the past for the study of a variety of DNA models.[13,15] The model describes double-stranded DNA as two intertwined strings of rigid nucleotides, with pairwise interactions modeling the backbone covalent bonds, the hydrogen bonding, the stacking, cross-stacking, and excluded-volume interactions. oxDNA has been used in the past for the study of a variety of DNA models.[13,15] Results from the simulated separation distances between Cy5 and AuNCs on tiles D1 and D2 are represented as histograms in Figure 4.2.c. Design D1 represents a separation distance of 6.54 ± 1.36 nm between the dye and AuNC surface. D2 is 10.83 ± 2.56 nm separation distance. And D12 contains the capture sequences of both D1 and D2 to assemble two AuNCs on the tile.

The distances modeled by oxDNA were significantly larger than was estimated from the original caDNAno designs. The original designs in caDNAno predicted that the fluorophore, D1 capture sequence, and D2 capture sequence would all be on the same plane of the tile. Instead, we found that D1 and D2 were on opposite sides of the tile; thus, AFM images showing D1 and D2 present on the same tile were unachievable. The oxDNA simulation conditions reflected our experimental conditions for the photoluminescent (PL) measurements. The low salt conditions for these measurements caused more repulsion between the tile's anionic helices and contributed to the larger-than-expected distances. At 20 °C, the capture sequences have an extensive range of motion leading to significant standard deviations in the simulated distances.

4.3.3. Self-assembly of AuNCs on DNA origami

We carried out steady-state fluorescent measurements for D1, D2, and D12 tiles to demonstrate that our assemblies could be applied to ET biosensor designs. AuNCs have been shown to quench fluorescent dyes in a distance-dependent manner as characterized by (SET)[16–19]. In SET, energy from a photoexcited chromophore is dampened in the presence of a nanometal surface with a $1/d^4$ distance-dependence[20]. To determine the theoretical quenching efficiencies between Cy5 and AuNC d_0 were calculated using Equation 1.8. The ω_{dye} for Cy5 is 2.81×10^{15} s^{-1}, and the Φ_{dye} for Cy5 attached to the end of an oligonucleotide in a buffered solution is 0.20[21–23]. The d_0 for Cy5 in our system was 6.22 nm.

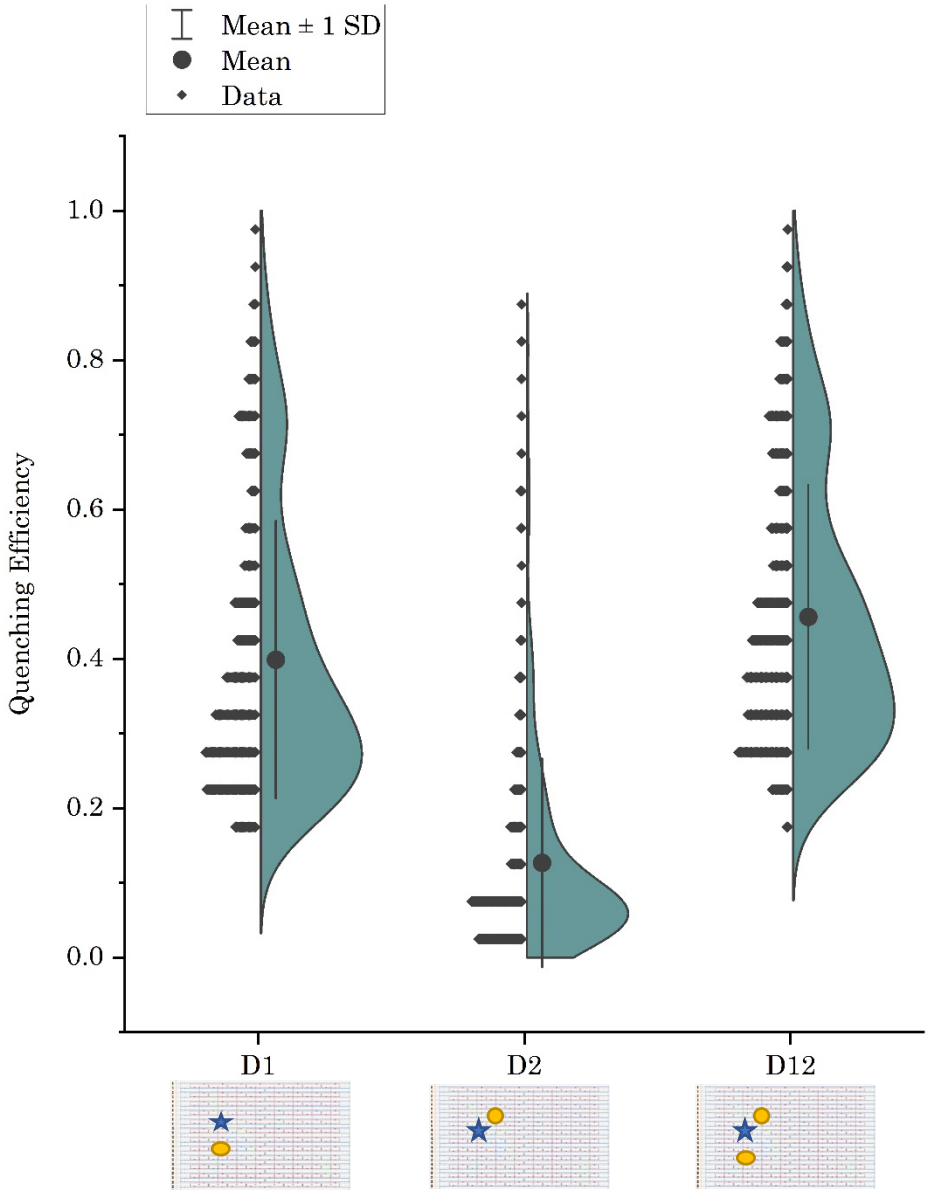

Figure 4.3. Distribution of the theoretical quenching efficiencies for the D1, D2, and D12 tile assemblies.

Using Equation 1.8 and the distances predicted by oxDNA for the D1, D2, and D12 tiles, our predicted theoretical values are 0.40±0.19, 0.13±0.14, and 0.46±0.18, respectively. The distributions of quenching efficiency from these calculations are illustrated in Figure 4.3.

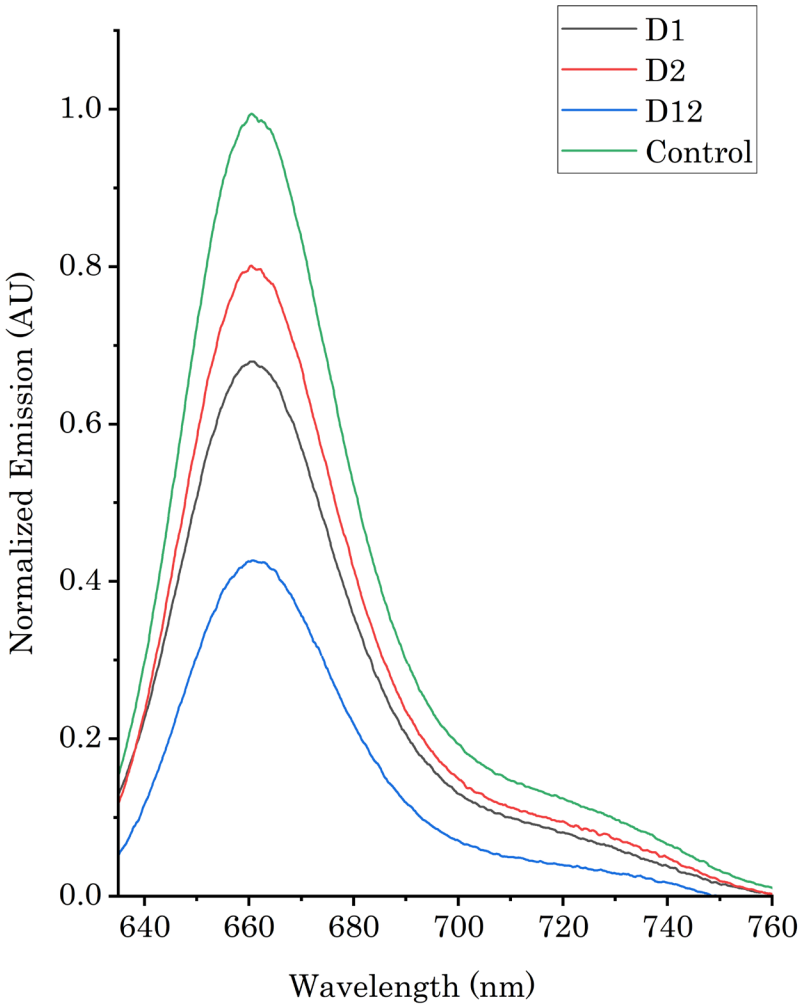

Figure 4.4. Normalized PL quenching for each tile assembly.

Experimental quenching efficiency was determined using *Equation 3.4*, where the fluorescent intensity of the control tile is I and the tiles with AuNC(s) is I_Q. The experimental quenching efficiency observed for D1, D2, and D12 was 0.43 ± 0.04, 0.21 ± 0.04, and 0.60 ± 0.06, respectively. These results show that the quenching efficiency was proportional to the quantity and proximity of AuNCs to a fluorescent dye but show some significant deviations from the theoretical values. There are a few potential reasons for the deviation. The first is that theoretical efficiencies depend on the modeled separation distances, and the second is the possible surplus effect for ET assemblies with multiple acceptors, as detailed below.

Table 4.1: Summary of Theoretical and Experimental Efficiencies

Tile Assembly	D1	D2	D12
Separation distance (d)	6.54±1.36 nm	10.83±2.56 nm	6.54±1.36 nm and 10.83±2.56 nm
Experimental E	0.43±0.04	0.21±0.04	0.60±0.06
Theoretical E	0.40±0.19	0.13±0.14	0.46±0.18

The separation distances generated by oxDNA had a relative SD of 0.21 for D1 and 0.24 for D2, indicating that the capturing sequences extending from the tile have a dynamic range of motion. When larger AuNPs are assembled on DNA origami, there are usually multiple capture strands to reduce this range of motion. With an AuNC that is approximately 1 nm in size, it is necessary to rely on a single capture sequence. Reducing the RSD error associated with this range of motion would be possible by reducing the capture sequence length.

Salt concentration significantly impacts the stability and movement of DNA origami[24]. Due to the simplicity required of course-grained modeling, the simulations are limited to monovalent ions. Magnesium-DNA interactions are not uniform and site-specific[15]. Our running conditions for fluorescent measurements were 6 mM $MgCl_2$ and 500 mM NaCl in a 1X PBS buffer, so there is no exact salt simulation for our tiles. When we simulated different salt concentrations, we found that it had little effect on the dynamic range of the capture sequences. However, when the simulation temperature was run at 4 °C, the relative SD dropped to less than 5% for both distances. Future experiments dependent on a single capture sequence should be run at 4 °C.

The second consideration is the discrepancy between the theoretical and experimental efficiencies for tiles with multiple AuNC acceptors. The energy transfer rate constant (k_{ET}, Equations 1.1 and 1.8) describes the probability of donor de-excitation in a single dye-AuNC pair. The efficiency model described by Equation 1.8 assumes that this rate will behave independently between the donor and each acceptor in a multiplexed assembly. Typical ET sensors are designed to detect single events, but there have been some investigations into FRET multiplexes with multiple acceptors. In these studies, they observed that these multiplexes consistently demonstrated ET efficiencies greater than predicted by Equation 1.8 and have been described as the surplus effect[25–27]. This surplus effect increases with the number of acceptors in the multiplex.

FRET has first theorized 75 years ago and has been much more widely used and studied than the newer SET theory. A few SET assemblies with multiple acceptors have relied on a combination of FRET and SET, thus not offering a clear window into if a surplus effect is occurring. There has been one study that constructed assemblies of multiple AuNCs attached to fluorophores via PEGylated ligands. They found that the experimental efficiencies did not agree with the SET model. Rather than contribute this to a surplus effect, they proposed that the damping mechanism was volume rather than surface dominant[28].

In Chapter 3, we observed that the quenching in the bi-conjugate was greater than theorized. The bi-conjugate design of that experiment could not rule out spFRET nor dimerization as the cause for the observed decrease in relative fluorescence. Using the DNA origami tile for this chapter's assemblies eliminates the possibility of collisional quenching, spFRET, and Cy5 dimerization, yet there is still a 0.14 efficiency discrepancy between experimental and theoretical. Our steady-state fluorescent measurements and the wide variability in our separation distances do not provide enough information to elucidate what additional de-excitation pathway could occur within the multiplex. However, our assemblies at 4 °C combined with a more quantitative technique, such as alternating-laser excitation[25], could shed light on this mechanism.

4.4. Conclusion and outlook

This chapter demonstrated the first successful AuNC self-assembly with precisely controlled positions on a DNA origami template. The separation distances were estimated using course-grained simulation and showed relatively close experimental agreement with the theoretical quenching predicted by NSET. In addition, we have noted small adjustments to our method that could improve the precision, especially regarding distance-dependent modalities. These results demonstrate that by functionalizing the AuNCs with the oligonucleotides, we can program the self-assembly of the AuNCs with nanometer precision.

AuNCs are promising materials for *in vivo* applications due to their stability, non-toxicity, and bio-conjugatable surfaces. A fundamental understanding of how nanoclusters coupled to other nanomaterials would expand their use in diagnostics, biosensing, and imaging applications. This ability to program the assembly of AuNCs on DNA origami templates opens a range of applications for the study and application of AuNCs. The results of these triads suggest that with this new ability to organize AuNCs and other emitters with nanometer precision and prescribed geometry, we now have a

powerful platform to study how these AuNCs couple to each other and fluorophores.

4.5. References

1. Ding B, Deng Z, Yan H, Cabrini S, Zuckermann RN, Bokor J. Gold Nanoparticle Self-Similar Chain Structure Organized by DNA Origami. *J Am Chem Soc*. 2010;132(10):3248-3249. doi:10.1021/ja9101198

2. Hung AM, Micheel CM, Bozano LD, Osterbur LW, Wallraff GM, Cha JN. Large-area spatially ordered arrays of gold nanoparticles directed by lithographically confined DNA origami. Published online 2010. doi:10.1038/NNANO.2009.450

3. Pal S, Deng Z, Ding B, Yan H, Liu Y. DNA-Origami-Directed Self-Assembly of Discrete Silver-Nanoparticle Architectures. *Angewandte Chemie*. 2010;122(15):2760-2764. doi:10.1002/ANGE.201000330

4. Pilo-Pais M, Goldberg S, Samano E, Labean TH, Finkelstein G. Connecting the nanodots: Programmable nanofabrication of fused metal shapes on DNA templates. *Nano Lett*. 2011;11(8). doi:10.1021/nl202066c

5. Bui H, Onodera C, Kidwell C, et al. Programmable periodicity of quantum dot arrays with DNA origami nanotubes. *Nano Lett*. 2010;10(9). doi:10.1021/nl101079u

6. Steinhauer C, Jungmann R, Sobey TL, Simmel FC, Tinnefeld P. DNA Origami as a Nanoscopic Ruler for Super-Resolution Microscopy. *Angewandte Chemie International Edition*. 2009;48(47):8870-8873. doi:10.1002/anie.200903308

7. Kumar S, Jin R. Water-Soluble Au 25 (Capt) 18 Nanoclusters: Synthesis, Thermal Stability, and Optical Properties. Accessed August 8, 2017. http://www.rsc.org/suppdata/nr/c2/c2nr30833a/c2nr30833a.pdf

8. Rothemund PWKK. *Folding DNA to Create Nanoscale Shapes and Patterns*. Vol 440. Nature Publishing Group; 2006:297-302. doi:10.1038/nature04586

9. Douglas SM, Marblestone AH, Teerapittayanon S, Vazquez A, Church GM, Shih WM. Rapid prototyping of 3D DNA-origami shapes with caDNAno. *Nucleic Acids Res*. 2009;37(15):5001-5006. doi:10.1093/NAR/GKP436

10. Cao HH, Gary R. Abel Jr, Gu Q, et al. Seeding the Self-Assembly of DNA Origamis at Surfaces. *ACS Nano*. 2020;14(5):5203-5212. doi:10.1021/ACSNANO.9B09348

11. Wagenbauer KF, Engelhardt FAS, Stahl E, et al. How We Make DNA Origami. *ChemBioChem*. 2017;18(19):1873-1885. doi:10.1002/cbic.201700377

12. Snodin BEK, Schreck JS, Romano F, Louis AA, Doye JPK. *Coarse-Grained Modelling of the Structural Properties of DNA Origami*. Accessed January 3, 2019. https://arxiv.org/pdf/1809.08430.pdf

13. K Doye JP, Fowler H, Prešern D, et al. The oxDNA coarse-grained model as a tool to simulate DNA origami.

14. Kumar S, Jin R. Water-soluble Au25(Capt)18 nanoclusters: synthesis, thermal stability, and optical properties. *Nanoscale*. 2012;4(14):4222-4227. doi:10.1039/c2nr30833a

15. Poppleton E, Romero R, Mallya A, Rovigatti L, Šulc P. OxDNA.org: a public webserver for coarse-grained simulations of DNA and RNA nanostructures. *Nucleic Acids Res*. 2021;49(W1):W491-W498. doi:10.1093/NAR/GKAB324

16. Yun CS, Javier A, Jennings T, et al. Nanometal surface energy transfer in optical rulers, breaking the FRET barrier. *J Am Chem Soc*. 2005;127(9):3115-3119. doi:10.1021/JA043940I

17. Jennings TL, Singh MP, Strouse GF. Fluorescent lifetime quenching near d = 1.5 nm gold nanoparticles: probing NSET validity. *J Am Chem Soc*. 2006;128(16):5462-5467. doi:10.1021/JA0583665

18. Ruppin R. Decay of an excited molecule near a small metal sphere. *J Chem Phys*. 1998;76(4):1681. doi:10.1063/1.443196

19. T. L. Jennings, M. P. Singh and, Strouse* GF, Jennings TL, Singh MP, Strouse GF. Fluorescent lifetime quenching near d = 1.5 nm gold nanoparticles: Probing NSET validity. *J Am Chem Soc*. 2006;128(16):5462-5467. doi:10.1021/ja0583665

20. Persson BNJ, Lang ND. Electron-hole-pair quenching of excited states near a metal. *Phys Rev B*. 1982;26(10):5409-5415. doi:10.1103/PhysRevB.26.5409

21. Meares A, Susumu K, Mathur D, et al. Synthesis of Substituted Cy5 Phosphoramidite Derivatives and Their Incorporation into Oligonucleotides Using Automated DNA Synthesis. *ACS Omega*. 2022;7(13):11002-11016. doi:10.1021/acsomega.1c06921

22. Hensbergen AW, M. van Willigen D, M. Welling M, et al. Click Chemistry in the Design and Production of Hybrid Tracers. *ACS Omega*. 2019;4(7):12438-12448. doi:10.1021/acsomega.9b01484

23. Malicka J, Gryczynski I, Fang J, Lakowicz JR. Fluorescence spectral properties of cyanine dye-labeled DNA oligomers on surfaces coated with silver particles. *Anal Biochem*. 2003;317(2):136. doi:10.1016/S0003-2697(03)00005-8

24. Bosco A, Camunas-Soler J, Ritort F. Elastic properties and secondary structure formation of single-stranded DNA at monovalent and divalent salt conditions. *Nucleic Acids Res*. 2014;42(3):2064. doi:10.1093/NAR/GKT1089

25. Koushik S V., Blank PS, Vogel SS. Anomalous Surplus Energy Transfer Observed with Multiple FRET Acceptors. Brezina V, ed. *PLoS One*. 2009;4(11):e8031. doi:10.1371/journal.pone.0008031

26. Bunt G, Wouters FS. FRET from single to multiplexed signaling events. doi:10.1007/s12551-017-0252-z

27. Uphoff S, Holden SJ, Le Reste L, et al. Monitoring multiple distances within a single molecule using switchable FRET. *Nature Methods 2010 7:10*. 2010;7(10):831-836. doi:10.1038/nmeth.1502

28. Oh E, Huston AL, Shabaev A, et al. Energy Transfer Sensitization of Luminescent Gold Nanoclusters: More than Just the Classical Förster Mechanism. *Sci Rep*. 2016;6:35538. doi:10.1038/srep35538